Åbo Akademi University

Didem Şen Karaman

Physicochemical Characteristics of Silicananoparticles Tailored for Nanomedicine

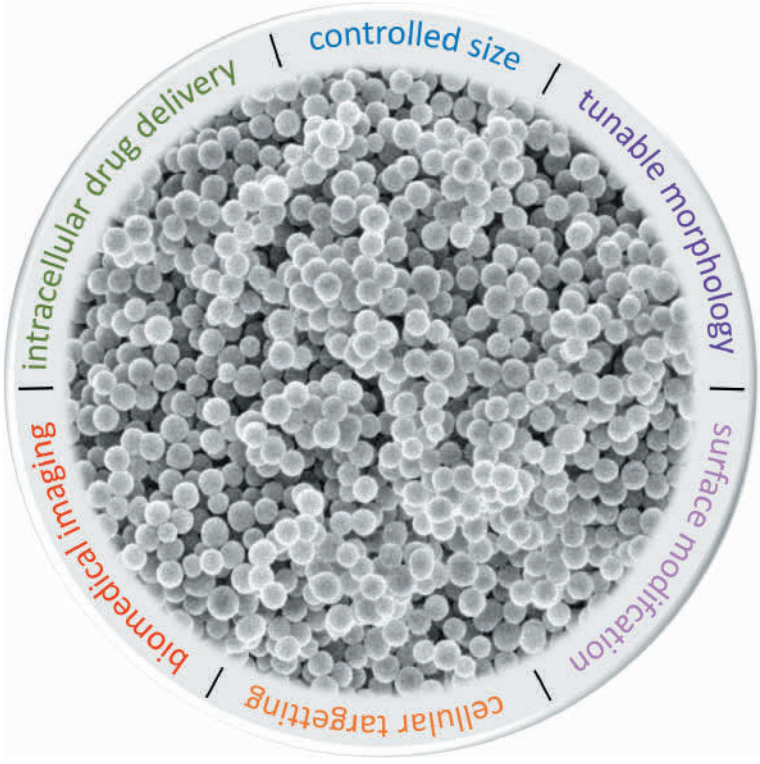

PHYSICOCHEMICAL CHARACTERISTICS OF SILICANANOPARTICLES TAILORED FOR NANOMEDICINE

DIDEM ŞEN KARAMAN

Laboratory of Physical Chemistry
Faculty of Science and Engineering
Åbo Akademi University
Åbo, Finland 2016

Supervised by

Professor Jessica M. Rosenholm
Pharmaceutical Sciences Laboratory
Faculty of Science and Engineering
Åbo Akademi University, Finland

Co-Supervised by

Assistant Professor Jixi Zhang
Department of Biomedical Engineering
Chongqing University, China

Pre-examined by

Docent Jarno Salonen
Laboratory of Industrial Physics
Department of Physics and Astronomy
University of Turku, Finland

and

Dr. Amirali Popat
School of Pharmacy
University of Queensland, Austria

Opponent

Docent Jarno Salonen
Laboratory of Industrial Physics
Department of Physics and Astronomy,
University of Turku, Finland

ISBN 978-952-12-3406-4 (print)
ISBN 978-952-12-3407-1 (PDF)
Painosalama Oy – Turku, Finland 2016

"If you see it's impossible,
it is the time to change your point of view"
…
Turgul Y., Hunting Season, 2010

ACKNOWLEDGEMENTS

This work was carried out at the Laboratory of Physical Chemistry at Åbo Akademi University, Turku, Finland. I would like to thank several persons who have been involved in the work leading to PhD thesis.

First of all, I would like to express my sincere gratitude to my supervisor Prof. Jessica Rosenholm for continuous support of my PhD studies. I have been always lightened with her guidance not only about scientific manners also for many other difficult cases. I couldn't not have imagined having a better supervisor for my PhD study.

Besides my supervisor I would like to thank my co-supervisor Assistant Prof. Jixi Zhang for very valuable discussions and comments when he was also a FyKe member and during writing of my PhD thesis.

I own special thanks to Prof. Jouko Peltonen for the overall support and also providing me valuable comments concerning the content and the form of the book. I am honored to have Dr. Jarno Salonen and Dr. Amirali Popat as reviewers for my thesis and thanks for valuable comments. My sincere thanks also go to Prof. Mika Linden who provided me opportunity to join FyKe family and start my PhD studies. I wish to thank all Fyke family (past and present) for creating a friendly working environment.

I would like to acknowledge my coauthors for their contributions to publications included in my thesis. Furthermore, I have been so lucky to have several colleagues that created a friendly, helping atmosphere and provided good discussions. In this respect, I would like to thank all BioNanoMaterials group members for being so wonderful lab mates and bringing fun to my daily lab works.

The Center for Functional Materials (FUNMAT) and "*Rare-earth metal doped silica nanoparticles as targeted probes for optical and MR-imaging*" Academy of Finland project #260599 are greatly acknowledged for financial support during my PhD study.

I send my appreciation and thoughts to my parents. Your belief in my skills and supports to my choices make me feel stronger in my life.

Most thankful I am to my beloved husband and our son. I feel so blessed to have you in my life. You are my rainbow in life.

Turku, May, 2016

Didem ŞEN KARAMAN

TABLE OF CONTENTS

ABSTRACT

Silica nanoparticles have broad applications as multifunctional nanoparticle systems in nanomedicine. Silica nanoparticles possess a great potential as drug delivery systems: their small size, unique surface properties and loading capacities make them attractive for drug delivery. Moreover, they can serve simultaneously as diagnostic tools. The attractive combination of drug delivery and simultaneous tracking of nanoparticles is known under the term “theranostics”. Hereby, diagnostic and therapeutic features can be united in the same particle with the controlled synthesis of silica nanoparticles. For successful use of nanoparticles in nanomedicine, their physicochemical characteristics need to be well-controlled to predict their behavior in biological matrices.

The size, shape, and surface characteristics of silica nanoparticles define their behavior at the nano-bio interface. In this study, silica nanoparticles were prepared with diverse size, shape, surface, and composition with the focus of endowing the nanoparticles with multifunctionality and facilitating their use in biomedical applications.

The dispersion stability of nanoparticles is an important aspect for both diagnosis and therapy applications. In this study, the dispersion stability of silica nanoparticles was evaluated after altering the surface physicochemical characteristics by a surface coating process. The process was mainly achieved by physical adsorption of copolymers composed of polyethylene glycol grafted polyethyleneimine (PEG-PEI) prepared with two different grafting ratios. Then, the emphasis was put on evaluating the colloidal stability and redispersibility of particles in the biologically relevant medium. Differences in redispersibility and dispersion stability of particles were observed by tuning of PEG-PEI composition on the particle surfaces. Furthermore, physiological responses (i.e. protein corona formation) to surface modified silica nanoparticles were investigated.

In therapeutic applications, when the nanoparticles are designed as drug carriers, internalization of particles by target cells is aimed in order to exert intracellular therapeutic effects. Enhancement in the cellular internalization of nanoparticles can be facilitated by altering the size, shape and surface properties of the particles. In this thesis, silica nanoparticles with spherical and rod-like shapes, porous, non-porous and hollow structures were prepared on the submicron scale for biomedical purposes. Among these approaches, the extent of nanoparticle internalization was altered by modifying the shape and surface modification by preparing similarly sized spherical and rod-like particles with various net surface charges. The obtained results revealed that the particle shape–induced uptake play a predominant role as compared to surface charge dependent uptake. We could show that particles with a

higher aspect ratio were internalized more than their spherical counterparts. The surface charge of the particles remained a secondary regulator to control the internalization of particles.

In therapeutic applications, targeted drug delivery is a promising approach which benefits from lower doses and avoiding side effects to healthy cells. By the targeted drug deliver strategy, drugs can be protected in a drug delivery system (DDS), e.q. particulate drug delivery system and cannot freely diffuse, and the uptake of the DDS *via* specific ligand-receptor interaction, where the targeted receptors are mainly expressed at lesion sites, can be provided. Therefore, specific uptake of the DDS mainly by the injured cells reduces the side effects. In this thesis, mesoporous silica nanoparticles were designed as drug carrier with active cellular targeting capability. Additionally, the particles were loaded with a potential anticancer compound. The effect of the free potential anticancer compound and the silica nanoparticle incorporated compound was tested *in vitro*. The apoptotic effect of the potential anticancer compound was significantly enhanced compared to free compound with the employed targeted mesoporous silica nanoparticle based DDS.

Tracking of silica nanoparticles in the biological environment via different imaging modalities during the delivery of drug is an important feature for multifunctional nanoparticles. This is usually achieved by the incorporation of an imaging probe into the silica network. The detectability of particles can be altered by the structural and morphology of silica nanoparticles, as well as the incorporation strategy of imaging probe into silica network. Furthermore, surface coating of the nanoparticles, leaching of the probe from the silica matrix, and the surrounding pH can affect the detectability significantly. In the present thesis, these phenomena were evaluated in order to clarify their influence on detectability of particles via fluorescent and magnetic resonance imaging methodologies.

The thesis addresses the critical steps in the synthesis of silica nanoparticles to be used in theranostic applications. Various methods were explored to obtain tailor-made silica nanoparticles. The work provides deep insight into how the physicochemical properties of silica nanoparticles influence their fate in biological environment and can serve as a guideline to design safe and efficient theranostic systems.

SAMMANFATTNING

Multifunktionella kiseldioxidnanopartiklar har en bred tillämpning inom nanomedicin. En attraktiv kombination är samtidig läkemedelstillförsel och spårning av nanopartiklarna, vilket är känt som ”teranostik”. Genom kontrollerad design av kiseldioxidnanopartiklarna kan terapi och diagnostik på detta sätt kombineras i samma partikel. För en lyckad användning av nanopartiklar inom nanomedicin måste deras fysikalisk-kemiska egenskaper vara välkontrollerade för att kunna förutspå deras beteende i biologiska system.

I denna studie tillverkades kiseldioxidnanopartiklar med varierande storlek, form, yta och sammansättning med fokus på att utrusta nanopartiklarna med multifunktionalitet och på så sätt främja deras användning inom biomedicinska tillämpningar. Kiseldioxidnanopartiklar med sfäriska och stav-liknande former, porösa, icke-porösa och ihåliga strukturer tillverkades. De erhållna resultaten visade att nanopartiklarnas form har större inverkan på upptaget i celler jämfört med effekten av deras ytladdning. Nanopartiklarnas dispersionsstabilitet är en annan viktig aspekt för både diagnostiska och terapeutiska tillämpningar. Genom att ändra kiseldioxidnanopartiklarnas fysikalisk-kemiska ytegenskaper med ytfunktionalisering, bedömdes dispersionstabiliteten av nanopartiklarna. Nanopartiklarnas ytsammansättning justerades och skillnader i dispergerbarhet och dispersionsstabilitet undersöktes i biologiskt medium.

Inom terapeutiska tillämpningar är målsökande läkemedelsfyllda nanopartiklar en lovande taktik som medför lägre läkemedelsdoser och minskar sidoeffekterna. I denna avhandling designades mesoporösa kiseldioxidnanopartiklar för användning som målsökande läkemedelsbärare. Dessa partiklar laddades med ett potentiellt anti-cancer läkemedel. En klart högre apoptotisk effekt kunde påvisas med de läkemedelsfyllda partiklarna jämfört med fri drog in vitro. En viktig egenskap för sådana multifunktionella nanopartiklar är också att kunna spåra dem under läkemedelsfrisättningen i biologisk miljö med olika bildåtergivningsmetoder. Detta kan uppnås genom att infoga en markör i kiseldioxidnätverket. Kiseldioxidnanopartiklarnas bildåtergivningsförmåga modifierades på olika sätt och inverkan på detekterbarheten analyserades med fluorescerande metoder och med magnetisk resonanstomografi.

Denna avhandling lyfter fram de kritiska parametrarna vid syntes av kiseldioxidnanopartiklar för teranostiska tillämpningar. Olika metoder undersöktes för att erhålla skräddarsydda nanopartiklar. Detta arbete bidrar med en djup insikt i hur nanopartiklarnas fysikalisk-kemiska egenskaper påverkar deras beteende i biologisk miljö, och arbetet kan därför fungera som riktlinje för att designa säkra och effektiva nanomediciner.

LIST OF ORIGINAL PUBLICATIONS

I. **Rational evaluation of the utilization of PEG-PEI copolymers for the facilitation of silica nanoparticulate systems in biomedical applications**

D. Şen Karaman, T. Gulin-Sarfraz, G. Hedström, A. Duchanoy , P. Eklund , J. M. Rosenholm, *Journal of Colloid And Interface Science*, 418, **2014**, 300-310.

II. **Shape engineering vs organic modification of inorganic nanoparticles as a tool for enhancing cellular internalization**

D. Şen Karaman, D. Desai, R. Senthilkumar , E.M. Johansson, N. Råtts, M. Odén, J.E. Eriksson, C. Sahlgren, D. M. Toivola, J.M. Rosenholm**,** *Nanoscale Research Letters*, 7, **2012**, 1-14.

III. **Targeted delivery of new anticancer compound anisomelic acid using chitosan-coated porous silica nanorods for an enhanced apoptotic effect in cervical cancer cells**

R. Senthilkumar, **D. Şen Karaman**, P. Paul, E.M. Björk, M. Odén, J. E. Eriksson, J.M. Rosenholm, *Biomaterials Sciences*, 1, **2015**, 103-111.

IV. **Design considerations for mesoporous silica nanoparticulate systems in facilitating biomedical applications**

D. Desai, **D. Şen Karaman**, N. Prabhakar, S. Tadayon, A. Duchanoy, D. M. Toivola, S. Rajput, T. Näreoja, J.M. Rosenholm, *Mesoporous Biomaterials*, 1, **2014**, 16-43.

V. **One-Pot Synthesis of Pore-Expanded Hollow Mesoporous Silica Nanoparticles**

D. Şen Karaman, T. Gulin-Sarfraz, J. Zhang, J.M. Rosenholm, *Materials Letters*, 143, **2015**, 140-143.

VI. **Modulation of the structural properties of mesoporous silica nanoparticles to enhance the T1-weighted MR imaging capability**

D. Şen Karaman, D. Desai, J. Zhang, S. Tadayon, G. Unal, J. Teuho, J. Sarfraz, J.-H. Smått, H. Gu, T. Näreoja, J. M. Rosenholm, *Journal of Materials Chemistry B*, 4, **2016**, 1720-1732.

CONTRIBUTIONS OF THE AUTHOR

In PAPER I, the author was responsible for the sample preparation, characterization of particles, analysis of the results and writing the first draft. NMR analysis was performed together with P. Eklund and i*n vitro* experiments were performed by T. Gulin-Sarfraz.

In PAPER II the author was responsible for some of the sample preparation (S-MSP1, NR-MSP-$PEI_{ads.}$), characterization of the samples, and analysis of characterization data and contributed writing of the first draft. Rod-like mesoporous silica nanoparticles (bare) were prepared by E. M. Johansson, *In vitro* experiments and analysis of these data were performed by D. Desai and R. Senthilkumar.

In PAPER III, the author was responsible for surface modification, and characterizations of samples and the analysis of characterization data and writing some parts of first draft. Rod-like mesoporous silica nanoparticles (bare) were prepared by E. M. Björk and *in vitro* experiments and analysis of data were performed by R. Senthilkumar.

In PAPER IV, the author was responsible for some of the sample preparations (F-MSN1, T-MSN1) and surface modifications ($PEI_{ads.}$F-MSN1, $PEI_{ads.}$T-MSN1) and their characterizations. The analysis of the characterization data was performed by the author. Author has contributed the writing the first draft. D. Desai performed the rest of the samples preparations and their characterizations. I*n vitro* experiments and analysis of these data were performed by D. Desai and N. Prabhakar.

In PAPER V, the author was responsible for the preparation of the samples, their characterizations and analysis of characterization and writing the first draft. SEM images were taken by L. Silvander, TEM imaging was performed by J. Zhang and N_2 sorption analysis was carried out by T. Gulin-Sarfraz.

In PAPER VI, the author is responsible for the sample preparation and analysis of their characterization data, writing the first draft of the manuscript. Relaxivity measurements were performed by J. Zhang. ICP-MS analysis was carried out by S. Lindholm. X-ray diffraction analysis was carried out by J.-H. Smått. XPS measurements were carried out by J. Sarfraz. SEM images were taken by L. Silvander. *In vitro* and *in ovo* experiments were performed by J. Teuho, D. Desai, and S. Tadayon. Analysis of image data was performed by S. Tadayon.

LIST OF SUPPORTING PUBLICATIONS

i. **Polyethyleneimine-functionalized large pore ordered silica materials for poorly water-soluble drug delivery**

Martin, R. A. Garcia, **D. Şen Karaman**, J.M. Rosenholm, *Journal of Materials Science*, 49**, 2014**, 1437-1447.

ii. **Core-shell designs of photoluminescent nanodiamonds with porous silica coatings for bioimaging and drug delivery II: Application**

N. Prabhakar, T. Näreoja, E. Von Haartman, **D. Şen Karaman**, H. Jiang, S. Koho, T. Dolenko , P. Hänninen, I.D. Vlasov, G.V. Ralchenko, S. Hosomi, I. Vlasov, C. Sahlgren, J.M. Rosenholm, *Nanoscale*, 5, **2013**, 3713-3722.

iii. **Comparative safety evaluation of silica-based particles**

H. Kettiger, **D. Şen Karaman**, L. Schiesser, J.M. Rosenholm, J. Huwyler, *Toxicology in Vitro*, 30, **2015**, 355-363.

iv. **Targeted modulation of cell differentiation in distinct regions of the gastrointestinal tract via oral administration of differently functionalized mesoporous silica nanoparticles with PEI-PEG**

D. Desai, N. Prabhakar, V. Mamaeva, **D. Şen Karaman**, I.A.K. Lähdeniemi, C. Sahlgren, J.M. Rosenholm, D.M. Toivola, *International Journal of Nanomedicine*, 11, **2016**, 299-313.

v. **FRET-reporter nanoparticles to monitor redox-induced intracellular delivery of active compounds**

T. Gulin-Sarfraz, J. Sarfraz, **D. Şen Karaman**, J. Zhang, C. Oetken-Lindholm, A. Duchanoy, J.M. Rosenholm, D. Abankwa, *RSC Advances*, 4, **2014**, 16429-16437.

vi. **Functionalization of graphene oxide nanostructures improves photoluminescence and facilitates their use as optical probes in preclinical imagining**

N. Prabhakar, T. Näreoja, E. von Haartman, **D. Şen Karaman**, S.A. Burikov, T.A. Dolenko, T Deguchi, V. Mamaeva, P.E. Hänninen, I.I. Vlasov, O.A. Shenderova, J.M. Rosenholm, *Nanoscale*, 7, **2015**, 10410-10420.

1 INTRODUCTION

Nanotechnology is an emerging discipline, in which the multidisciplinary knowledge from physics, chemistry, biology, medicine, engineering, and informatics are combined. Nanotechnology includes both science and engineering to design, synthesize, characterize, and apply materials and devices whose smallest functional organization at least in one dimension is on the nanometer scale.

Today, the application of nanotechnology in medicine is referred to as nanomedicine, which is gaining importance and becoming promising especially with the advances in the development of novel materials. The novel nanomaterials, whose physiochemical properties differ from those of their larger counterparts due to their higher surface-to-volume ratio, have become excellent candidates for biomedical applications. Their small size and larger surface areas make them readily interact with biomolecules in biological environments. By gaining access to various sites of the body, nanoparticles provide the potential to detect and treat the disease. The aim of 'nanomedicine' might be broadly defined as the comprehensive monitoring, control, construction, repair, defense and improvement of all biological systems, using engineered nanostructures ultimately to achieve medical benefit.[1]

Among all nanomaterials, colloidal silica particles have been extensively used in diverse biomedical applications, as (1) contrast agents/optical labels that enable traceable imaging of targets, (2) carriers to transport drug payload for therapeutic intervention and (3) carriers of biomolecular ligands for targeted delivery. Within the mentioned platform, it is also desired to develop multifunctional silica nanoparticles which possess find-, fight, and follow- capabilities (3F functionality) that make the nanoparticles feasible to be used as imaging probes for lesion location (find), delivering the therapeutic agents to lesion sites (fight) and also monitoring the development of therapy (follow).[2] All these tasks might be accomplished through careful and rational tuning of the physicochemical properties of silica nanoparticles. For any nanomedical application, the size and shape of silica particles in addition to surface characteristics of the particles are considered as critical and allow them to be eagerly adapted for specific or multifunctional applications.

The wide design flexibility and extensive applicability of silica nanoparticles have led to them receive increasing attention in the field of nanomedicine. In this thesis, tuning the physicochemical characteristics of silica nanoparticles have been intensively studied in order to draw attention to the issues required to be considered in the design of silica nanoparticles for biomedical applications.

2 REVIEW OF THE LITERATURE

2.1 Methods for Fabrication of Nanoparticles

Manufacturing of nanoparticles is the vital field in of nanotechnology. Two approaches for the fabrication of nanoparticles have been envisaged: the top-down method and bottom-up methods. In the first approach, "top-down", a bulk material is restructured to give smaller features, for examples by lithographic techniques, film deposition, and growth, laser-beam processing and mechanical techniques (e.g. machining, grinding). Top-down methods offer a wide range of structures of high yield but are generally neither cost nor time-effective and for some methods, resolution below the 100 nm range is not easily achievable.[3]

In the bottom-up approach, nanocomponents are built up from atomic or molecular species by employing either chemical or physical deposition processes which allow the precursors to grow in size.[3] Currently bottom-up approaches provide an increasingly important complement to top-down techniques. The bottom-up approaches are inspired by biological systems, where nature has harnessed chemical forces to create essentially all the structures needed by life. Therefore, the main goal in the manufacturing of nanoparticles by bottom-up approach is set as to replicate nature's ability to create more elaborate structures which are formed by self assemble of precursors.[4]

In bottom-up approaches, the utilized processes are based on transformations in solution e.g. sol-gel processing, chemical vapor deposition (CVD), plasma or flame spraying synthesis, and laser pyrolysis, atomic or molecular condensation. These chemical processes rely on the availability of appropriate molecules as precursors, and also, the use of templating substrates like chemically or topologically patterned surfaces, inorganic mesoporous structures, and organic supramolecular complexes.

Among the existing bottom-up approaches sol-gel processing differs from other chemical processes due to its high chemical homogeneity, low processing temperatures, and the possibility of controlling the size and morphology of particles. This makes the sol-gel process cost-effective and versatile and also popular.[5]

2.1.1 General Remarks of Sol-Gel Method

Sol-gel approach is described as the formation of oxide network through polycondensation reactions of a molecular precursor in a liquid. The sol-gel-derived materials take part in various applications including microelectronics, solar cells, intelligent coatings, batteries, and catalysis, as well as in clinical and analytical chemistry. The sol-gel materials are prepared via the generation of colloidal suspensions, the "sol", subsequently converted to viscous "gel" and solid materials under proper conditions. Both organic (metal alkoxides) and inorganic (salts or particulate) precursors can be used to build up nanoparticles in sol-gel approach.

In the literature, among the used precursors tetrafunctional silicon alkoxide (e.g. tetraethyl orthosilicate) is the most frequently used and well-studied, due to the slower hydrolysis and condensation kinetics than in transition metal systems.[6]

In the sol-gel system, silicate gels are prepared via hydrolyzing monomeric silicon alkoxide precursors with the additional acid or base catalysts. The production of silica (silicon dioxide) starts with the hydrolysis of silicon alkoxides and continues with the condensation reactions. During the hydrolysis reaction (Eq. 1) alkoxide groups (OR) of the precursor are replaced with hydroxyl groups (OH) and siloxane (Si-O-Si) bonds are formed in the condensation reactions (Eq. 2, Eq. 3) plus by-products alcohol (ROH) or water. In the hydrolysis and condensation reactions of silicon alkoxides, alcohol is added as co-solvent in order to homogenize immiscible water and alkoxysilanes mixture.

$$\equiv Si - OR + H_2O \underset{esterification}{\overset{hydrolysis}{\rightleftharpoons}} \equiv Si - OH + ROH$$

Eq. 1

$$\equiv Si - OR + OH - Si \underset{alcoholysis}{\overset{alcohol\ condensation}{\rightleftharpoons}} \equiv Si - O - Si \equiv + ROH$$

Eq. 2

$$\equiv Si - OH + OH - Si \underset{hydrolysis}{\overset{water\ condensation}{\rightleftharpoons}} \equiv Si - O - Si \equiv + H_2O$$

Eq. 3

The kinetics of the above-given reactions are determined by various parameters, including the type of the precursor, pH of the sol, temperature, co-solvent the value of H_2O/Si and the solubility of silica. Diversification in these parameters can also affect the structure and properties of obtained polysilicate products.

The most commonly used tetraalkoxysilanes are tetraethoxysilane (TEOS) and tetramethoxysilane (TMOS). It is known that hydrolysis of the silicon alkoxide precursors is very sensitive to steric hindrance. The chain elongation and branching in the alkoxide ligands cause a decrease in the reaction rate and result in less-condensed gels.[7] In addition, replacement of alkoxy groups by other ligands such as acetylacetone/acetate, either hydrolysis of silicon tetraacetate or the hydrolysis of tetraalkoxysilanes in the presence of acetic acid results in very fast gelation.[7]

pH of sols affects both the hydrolysis and condensation reactions in the sol-gel approach. In general, employing catalysts makes the hydrolysis reactions rapid and complete. In the sol-gel approaches, mineral acids and ammonia are the most commonly used catalysts. The rate and the extent of hydrolysis and condensation reactions are influenced by the strength and concentration of the acid or base catalysts, [6] while temperature and solvent are of secondary importance.[8] Hydrolysis and condensation reactions usually take place simultaneously. The continuous condensation reactions build larger silicon-containing molecules by the process of polymerization as presented in Figure 1. The rate of the polymerization process is influenced by pH of the sol and Iler investigated the effect of pH in three approximate values; < pH2, pH 2-7 and > pH 7.[9] pH 2 appears as boundary since the point of zero charge (PZC), where the surface charge density is zero and the isoelectric point (IEP) where the electrical mobility of silica particles is zero, are both in the range of pH 1-3. At pH 7 or above pH 7 the particle growth occurs, and no aggregation and gel formation are observed since the solubility and dissolution rates are maximized due to the ionization of silica particles. Above pH 7, Ostwald ripening mechanism takes place in order to fulfill the growing of particles. Ostwald ripening is known as the dissolving of three-dimensional particles (nuclei) and deposition of them on the larger ones. At the ordinary temperature and pH above 7, the particle growth continues up to 10 nm with high dissolution and deposition rate after that it slows down. At high temperatures, the growth of particles continues to larger sizes. Above pH 7 silica particles start to repel each other due to being negatively charged and continue to grow without aggregation.

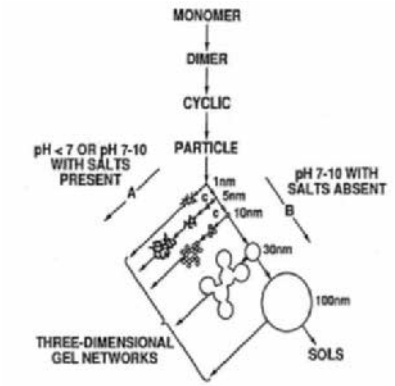

Figure 1. Polymerization behavior of aqueous silica.[9]

The molar ratio of H_2O/Si also has an impact on the morphology of the particles.[10] Poxviel *et al.*[11] investigated the hydrolysis of TEOS at different H_2O/Si

ratios. According to their report, increasing the ratio of H_2O/Si promotes the hydrolysis reaction. Under stoichiometric addition of water for the value of $H_2O/Si \leq 4$, the alcohol-producing condensation mechanism is favored, whereas it changes to water-producing condensation reaction for the increased ratio ($H_2O/Si \geq 4$). In the base catalyzed sol-gel synthesis high H_2O/Si (≥20) values aid to form well condensed particulate sols that can be dried as powders, whereas in the acid-catalyzed synthesis high ratio of 10 results thin films and for the preparation of silica fibers obtained from viscous sols is carried out by the low H_2O/Si values (~1).

2.1.2 Synthesis of Non-Porous and Porous Silica Particles

Stöber process is one of the mostly used chemical approaches employed to prepare non-porous silica materials. The process was discovered in 1968 by Werner Stöber *et al.*[12] which built on earlier work of by G. Kolbe in 1956[13]. In the study of Kolbe, synthesis of monodispersed silica particles based on the hydrolysis and subsequent condensation of silicon alkoxides in ethanol was investigated. Later on, Stöber *et al.* worked on the experimental conditions of this reaction systematically and investigated the controlled growth of spherical silica particles which is now the well-known Stöber process.[12] Subsequently, numerous synthesis routes and different precursors have been used for the preparation of non-porous silica particles with various sizes and shapes.

The preparation of mesoporous silica materials was reported for the first time by Yanagisawa *et al.* in 1990. [14,15] In their reported study, porous silica with controlled mesopores was obtained by the reaction of a layered silicate (kanemite) with aqueous solutions of alkyltrimethylammonium surfactants. Their findings revealed that the formation of ordered mesopores is mainly controlled by the surfactant assemblies which were controllable in the range of 2–4 nm depending on the alkyl chain length of the employed surfactants. In addition, mesoporous molecular sieves were prepared in 1992, when Mobil Oil scientists reported the synthesis of silica/alumina ordered mesoporous molecular sieves (designated as M41S).[16] The preparation of those mesophase silicates was based on self-assembly principles in a concentrated surfactant (C_nTMA) aqueous solution. Three mesophase silicates (MSM-41, -48 and -50) were prepared by the reaction of monomeric silicate and C_nTMA surfactants.[17,18,19]

MCM-41 is the initial member, and the most widely studied material of M41S family, and is based on a hexagonally packed rod-shaped micelle structures.[20] Another member of the family is MCM-48, which has a cubic structure and has been purposed as a three-dimensional and unconnected network of rod micelles. In the study of Vartuli *et al.*[21], they investigated a set of synthesis conditions in which tetrahylorthosilicate and cetyltrimethylammonium hydroxide solution were employed as structure directing agent (SDA). According to their report, MCM-41

was obtained at surfactant/silica molecular ratios less than 1, and as presented in the upper part *of* Figure 2, MCM-48 was synthesized when the ratios was between 1 to 1.1. Lamellar structured materials (MCM-50) can also be prepared by using the same liquid crystal templating system. The structure formation of MCM-50 was also investigated with a variety of synthesis conditions for different metal oxides. The siliceous lamellar structured material was obtained when the carbon number of the alkyl chain lengths exceeded six, and in another study, the siliceous lamellar structures formation was observed at higher surfactant/silica molecular ratios than those used for the hexagonal (MCM-41) and cubic (MCM-48) materials.[22]

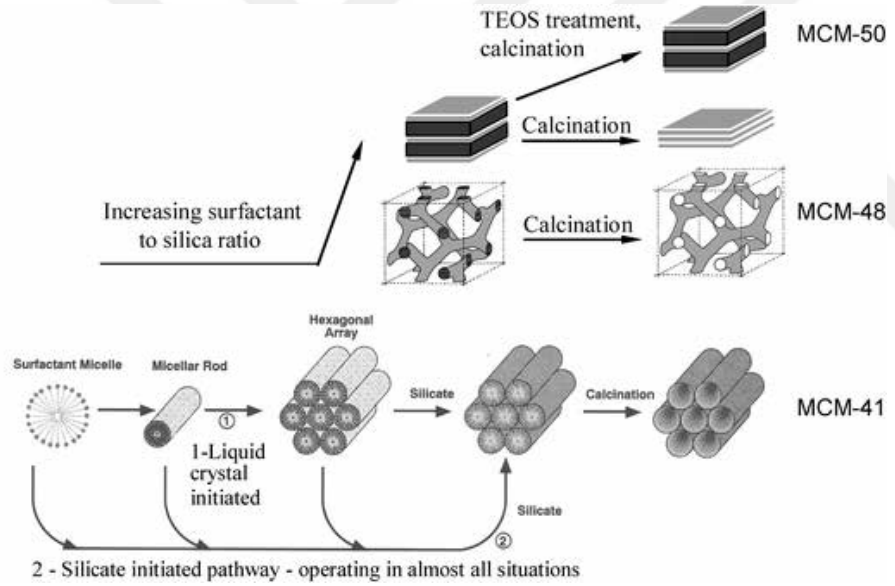

Figure 2. The initially proposed LCT mechanism of formation pathways and its further additions.[23]

The formation of templates in the synthesis of M41S family of materials was explained by the liquid crystal templating (LCT) mechanism, in which supramolecular assemblies of alkyltrimethylammonium surfactant serve as one component of the template. As presented in the below part of Figure 2, two possible mechanisms were stated for the formation of mesoporous silicates.[18] In pathway one, the literal meaning of LCT was accepted. It is initiated with the pre-existence of surfactant micelles (e.g. rod-like micelles) or liquid crystal phases in the surfactant precursor solution. Formation of silica framework consequently occurs with the migration and polymerization of silicate ions into the aqueous region. The second

pathway hypothesizes cooperative self-assembly of the liquid-crystal-like structures by the interaction between dissolved silica and surfactant species. In the literature, the first pathway has been argued that it cannot be operative in the majority of cases. In literature studies, series of experiments were carried out by altering the molar ratio of surfactant/ Si while the other synthesis variables were kept same. As a result of these serial experiments MCM-41, MCM-48, MCM-50 materials were obtained which can be also accepted as evidence of surfactant originating concepts such as straight liquid crystal and critical micelle concentration analogy cannot be accepted. The studied conditions showed that liquid crystalline phase formation prior to the formation of the silicon phase is not possible.[17,21] In the literature, both LCT initiated and silicate initiated pathways are accepted as valid so neither silicate nor surfactant alone would form a liquid crystalline phase, the phase occur under the conditions of their interactions together. The silicate ions have a vital role in the self-assembly process.[23]

In the literature, the formation of surfactant-silicate mesostructures was identified by three continuous processes which are multidentate binding of silicate ions to cationic surfactant, polymerization of silicate at the interface of the silicate-surfactant region and matching of charge density across the interface.[24] The explained formation mechanism also clarifies the details of phase transitions from lamellar and hexagonal mesophases. The binding of silicate ions to the surfactant leads to the formation of lamellar surfactant configuration by the acting of silicate ions as multidentate ligands with their high charge density. With the polymerization of silicate the transformation from lamellar to hexagonal phase occurs which is caused by the decrease in the charge density of silica and surfactant and the increase in average head-groups of surfactant assembly. The interactions between the silica species and surfactants can be utilized in different ways. As presented in Figure 3, four possible electrostatic interaction routes and also hydrogen bonding interactions exist.

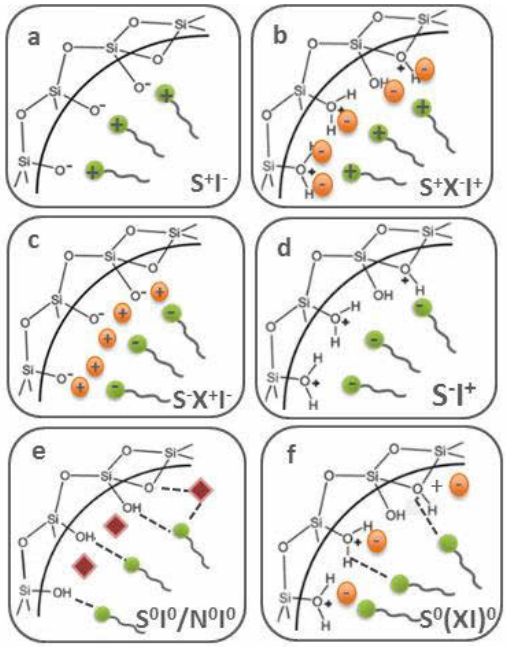

Figure 3. Mechanistic pathways of interactions between inorganic species and head groups of the surfactant (Adapted from reference [25]).

The synthetic pathway S^+I^- (Figure 3a) which is valid for the M41S family takes place under basic conditions where inorganic species silica is in anion form (I^-) and cationic surfactants (S^+) are used. When the preparation takes place under very acidic pH(pH~2) whereby the silica species are positively charged, in order to produce an interaction with cationic surfactant a mediator ion usually a halide (X) is used and the pathway named as $S^+X^-I^+$; as shown in Figure 3b. Conversely, when negatively charged surfactants (e.g., long-chain alkyl phosphates) are used as SDA, it is possible to work in basic media, where again a mediator ion is required to fulfill the interaction between negatively charged silica species and anionic surfactant and the synthesis pathway is named as $S^-X^+I^-$; pathway (Figure 3c). When the same synthesis is carried under acidic conditions there is no need for a mediator ion as presented in Figure 3d. All these four interactions composed of electrostatic nature of the species. In the last two pathways as presented in Figure 3e, the interactions between the silica species and non-ionic SDA is mediated by the hydrogen-bonding, where neural surfactants (S^0) or block copolymers (N^0) are employed as SDA. The pathways are named as S^0I^0 in which uncharged silica species and non-ionic SDA interact via hydrogen bonding. The other pathway is named as S^0 $(XI)^0$ in which the silicate species present ion pairs and the interaction formed is hydrogen bonding.

After the silica network and sufficient condensation degree have been obtained during the synthesis of the porous material, the templating molecules can be removed to open the porous structure since they are no longer needed to act as template molecules after the sufficient condensation degree is reached. Thermal decomposition (i.e. calcination) is one of the most frequently used techniques to remove the template from the readily structured material. Other employed methods are solvent extraction, oxygen plasma-extraction, ozone-extraction, [26] supercritical fluid extraction, [27] and microwave digestion.[28]

High-temperature treatment is known as calcination, and in this method, the synthesized materials are heated up to burn away the organic portions. In this method, the heating of the materials might result in other reactions such as removal of hydroxyl groups, shrinkage of pores. Especially in the cases of further modifications are needed other methods than calcination should be used to remove the template such as solvent extraction. In the solvent extraction method, either alcohol or ion exchange solutions are used. When the synthesis is carried out under very acidic conditions with the existence of both cationic surfactant and inorganic species and anionic counter ion, the templates are engaged via weak interactions with the inorganic network. In these cases, the template can be removed via water or ethanol solvents. The ion exchange method is usually performed when the synthesis was carried out via the route S^+I^- (Figure 3a) due to the strong interaction between the cationic surfactant head group and negatively charged inorganic species. The removal of template might be carried out via ion exchanging by refluxing in acidic ethanol solution or in a cationic alcohol solution. In the study of Hitz *et al.*[29], different extraction media and their efficacy in template removal were compared for the MCM-41 materials. Only solvents, acid or cationic proton donors in ethanol and neutral salts in ethanol were tested in their study. Their findings revealed that more polar alcohol solvent provides better template removal compared to less polar one such as ethanol was more efficient to remove template compare to 2-propanol as an extraction medium. Small cations and strong acids can also be used to extract the template. For instance, the acidic ethanol solution (EtOH/HOAc) with a low acid dissociation constant was reported as being less effective compared to the strong acid solution of ethanol ($EtOH/H_2SO_4$). In addition, the ethanolic solution of KNO_3 was not as efficient as $NaNO_3$. The amount of removed template by ethanol extraction is determined by the mobility of the cations in the close-packed micellar aggregates and by size of the cations too. In the literature, facile and efficient template removal was reported by Lang *et al.*[30] In their study, the solvent extraction of MCM-41 material, in which cetyltrimethylammonium bromide was employed as template, was carried out with the ethanolic solution of NH_4NO_3.The high performance of NH_4^+ was attributed to its chemical and geometrical similarity with

the head groups of surfactant molecules. The investigation was continued by characterization of solvent extracted MCM-41 material and no abundance of NH_4^+ was found in the material. Only the silanol groups were obtained on the surface of the MCM-41 material which was provided by the weak interaction between $NH4^+$ ions and SiO^- groups and leads directly to silanol groups. The solvent extraction method is advantageous for the design of functional materials which allows further modifications on the surface of materials.

In this study, mesoporous silica nanoparticles of type MCM-41 were prepared, in which the interactions of silica species and cationic surfactant (cetyltrimethylammonium bromide) exists as explained in Figure 3a. The removal of template was carried out by either the facile extraction method of Lang *et al.*[30] or calcination method depending on the further usage of the particles.

2.1.3 Morphology Engineering of Silica Nanoparticles

Recent advances in preparations of mesoporous silica nanoparticles (MSN) are focusing on altering the morphology. At the moment, bottom-up approach has been widely accepted as promising to prepare MSNs with diverse shapes such as spheres, rods, ellipsoids, platelets. In addition, hollow spheres that own hollow void space and mesoporous silica shell around become attractive for nanomedicine applications.

The sol-gel process provides flexible synthesis conditions for the synthesis of silica nanoparticles that ease the size, distribution and morphology control of particles through systematic monitoring of the reaction parameters. Compositional modification of nanoparticles and introduction of functional groups into the nanoparticle matrix are also possible by the sol-gel approach to providing diverse surface characteristics.

In the sol-gel approach, controlling the reaction kinetics by adding various dopants as precursors, changing pH or temperature dramatically during synthesis or starting with unique templates, such as cationic, non-ionic surfactants, polymers and electrolytes help to control the size and the shape of silica nanoparticles. The method developed by Stöber *et al.*[12] is capable of controlling silica nanoparticle synthesis by using tetraethoxysilane as silica precursor, water, ethanol and ammonia with the synthesis conditions at room temperature and high pH (~10).

The size and the distribution of size could be controlled by adjusting the composition of reactants, temperature, and pH. In the literature, there have been several studies which present the effects of TEOS concentration on final particle size. Increasing the TEOS concentration together with the concentration of water and ammonia up to 7 and 2 M respectively, results with increment in the size of the silica nanoparticles, after which the effect was reversed.[31] When the concentration of water gets higher the rate constant of hydrolysis increases and results in faster

kinetics, which leads to the production of smaller particles[32]. In the study of Rao *et al.*, [33] the effect of r= [H_2O] / [TEOS] on the size of particles at different temperatures was investigated. The observations revealed that the increased temperature at high r values results in larger particles whereas increased temperature at low r values results in smaller particle sizes.

Various morphologies can be obtained for mesoporous silica nanoparticles by altering the parameters of the fabrication process. The parameters which tune the shape of mesoporous silica nanoparticles from spherical to the rod-shaped have systematically been investigated by the researchers. The common observation in the existing studies is the aspect ratio rod-like mesoporous silica nanoparticles can be obtained through the deposition of self-assembled silicate micelles by altering the type of catalyst, stirring rate, type and concentration of surfactants and the molar ratio of reaction mixture and increased reaction temperature.[34,35,36,37]

The ellipsoidal MSNs preparation also exists in the literature but still it is a big challenge since common spherical shaped MSNs are promoted during the minimization of surface free energy. In the literature, the mesoporous silica ellipsoids were prepared by the addition of KCl and ethanol into SBA-15 type MSN synthesis with mesoporous channels along the long axis.[38] The spontaneous organization of polymeric surfactant into spherical micelles and further transfer to non-spherical rod-shaped shapes has been presented in the presence of different salt additions and ethanol.[39] The ellipsoidal MSNs with the texture of channels along the short axis have had a great attraction in the literature. The synthesis of such ellipsoidal MSNs has been carried out by altering the reaction components of MCM-41 and SBA-15.[40] In SBA 15 synthesis, parallel channels running along the short axis was succeeded by using a large amount of decane as a co-solvent in the presence of NH_4F during the synthesis. [41] MCM-41 type mesoporous silica nanoparticles with ellipsoidal shape were also produced by Mann and co-workers[42]. In their work, cationic surfactant templated oblate mesoporous silica nanoparticle synthesis reaction was quenched by the addition of HCl. In the study of Hao *et al.*, ellipsoidal MCM-41 mesoporous silica nanoparticles were obtained by using the cetyltrimethylammonium bromide (CTAB) and sodium dodecylbenzene sulfonate (SDBS) as a template.[43] In these syntheses, the ellipsoidal shape transformation of nanoparticles was carried out during the onset and development of mesophases ordering via side-on ordering and wall formation between the micelles produce a nematic-like silica-surfactant interior that aids to a sphere to ellipsoid transformation.

In addition, design of MSNs with large hollow cavities and mesoporous shells (H-MSNs) has also gained extensive attention in both fundamental and practical studies because of their unique properties[44] such as low density, large surface area, high

cargo-loading capacity, as well as their potential applications in drug/gene delivery[45, ,46], biomedical imaging[47], catalysis[48], etc.

To date, a number of different H-MSNs fabrication routes have been developed by typical soft-/hard-templating strategies [49, 50, 51, 52] in which the templates are removed by etchants such as hydrofluoric acid (HF) or alkaline solutions (NaOH or ammonia).[44] The varied etching processes can elaborately provide structural differences in nanoparticulate systems, such as, hollow porous spheres, porous spheres with solid core and yolk-shell (rattle-type) porous spheres, and so forth.

2.1.4 Surface Engineering of Silica Nanoparticles

Preparation of multifunctional mesoporous silica nanoparticles is another interest in the field. The core, coating and surface functional groups of silica nanoparticles make them amenable to modular design. Many functionalities of silica nanoparticles have been demonstrated in the literature, and the consolidation of the carefully selected functionalities make them applicable for simultaneously diagnosing and curing diseases.[53,54,55]

One of the main ways to obtain multifunctional silica nanoparticles is to modify the surface groups of silica particles. This can be provided via co-condensation or post-synthesis surface modification approaches.[56] In the co-condensation method, the functional groups are already introduced during the synthesis step, whereas post-synthesis functionalization approaches are carried out after the particles are synthesized.

The surface modification strategies should be decided in advance by considering the aimed applications, since the existing surface properties plays several roles in the interactions between the particles and the physiological environment and also target cells/tissue.[57] In the literature, possible advantages and disadvantages of different modification strategies have been investigated for the final applications. For instance, while aiming for targeted drug delivery applications, additional functionalities, such as targeting groups are recommended to be introduced to the outer particle surface.[58] In the case of preparing fluorescent nanoparticles, uniformly dispersed and segregated fluorophores in the silica network can be obtained with the co-condensation approach and by this way, self-quenching can be avoided to a large extent and, thus, the enhancement in the fluorescence detecting can be provided.

The organo-functionalization of internal and external surfaces of the silica nanoparticles via co-condensation (Figure 4a) and post-synthesis functionalization (Figure 4b) are presented in the below figures.

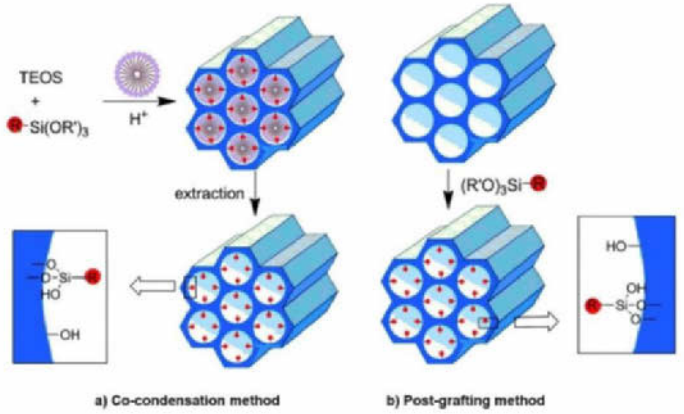

Figure 4. Surface functionalization approaches a) Co-condensation b) Post-grafting methods. [59]

Co-condensation of functional groups

In this method, the reaction of silica source and functional silanes is carried out via one-pot synthesis by substituting part of the silica source (tetraalkoxysilanes) with organosilanes.[25] In this way, the inorganic-organic hybrid network can be achieved. The organic functionalities are directly incorporated into the matrix of silica during the co-condensation approach, which has both advantages and disadvantages. The organic functionalities can be evenly distributed.[25] However, there is a risk of decrease in the degree of mesoscopic order of products with the increased concentration of organosilanes. Moreover, the reduction in pore volume, pore diameter, and specific surface area might be obtained due to the co-condensation of the organic groups into the silica network. A further point that needs to be taken care of in the co-condensation approach is the template removal step so the destruction of organic groups and silica linkage should be avoided. This is why commonly solvent extraction methods are employed to remove the template from the co-condensed porous silica nanoparticles.

Post-synthetic functionalization

The post-synthetic modifications might be carried out by chemical conjugation or adsorption of functional groups. The chemical conjugation process (to surfaces) is also known as grafting. In the grafting process, the silanols groups of the surface serve as anchors for reacting with organosilanes via elimination reactions. By this method, the mesostructures of the starting silica material is usually retained; but in the case of high density of organosilanes grafting, reactions at the pore openings might result in the inhomogeneous distribution of functional groups. This may even lead to blocking of the pores and incomplete grafting of center part of the pore

channels, albeit depending on the size of the functional moieties and the degree of occupation. Limited surface functionalization by post-synthetic functionalization has been reported due to low reactivity of surface silanols, the solvent polarity and dielectric constants used in the grafting. [60, 61] In the grafting process, the number and accessibility of the silanol groups are the most determinant factors for the concentration and the distribution of functional groups.[62] Water free conditions are also crucial to prevent the risk of organosilanes reaction with water and hierarchical polymerization of organosilanes in the pores.

Thermogravimetric analysis is a commonly used method to determine the extent of grafting. However, there are more quantitative and straightforward methods to define the extent of functionalization. In the literature, ^{13}C and ^{29}Si NMR were performed to determine the degree of silane condensation and hydrolysis which provide more quantitative information about the degree of grafting.[63]

Adsorptive methods are also used for post-synthesis functionalization of particles. By this method, a huge amount of different surface modifiers can be used for functionalization, such as small molecules, synthetic homopolymers and copolymers, natural polymers and so on. It is crucial to have sufficient interaction between particle surfaces and modifiers for the preparation of surface modified particles via adsorptive methods. In the present study, adsorptive methods were employed as the main strategy for surface modification. Adsorption of polymers and copolymers were carried out.

During the adsorptive functionalization process, the adsorption of ionic molecules on the particles is provided by the electrical interactions within the electrical double layer of the particles. The charge generation and the structure of electrical double layer aid to predict the electrical interactions during the adsorption process. The contributions of electrical interactions and specific interactions should be considered when the total adsorption energy is given during the adsorption process. The adsorption energy equation can be written as[64]:

$$\Delta G_{ads} = \Delta G_{elec} + \Delta G_{spec} \qquad \text{Eq. 4}$$

where ΔG_{elec} contains electrostatic interactions in the systems and ΔG_{spec} depends on the nonelectrical nature of the system. During the adsorption process high and low coverage of surfaces might result due to dominant electrical adsorption energy. In the adsorption process of similarly charged species and surfaces, adsorption cannot be succeeded efficiently due to the repulsion forces whereas the attraction forces between different surface charges help to have high surface coverage.

Several trends have been confirmed especially for the adsorption of homopolymers and the occurrence of the adsorption process take place only if the

critical value of the adsorption energy per chain be accomplished.[65] Within the explained trends, the adsorption is found to increase with decreasing solvent-polymer interaction, the adsorption increases with increasing molecular weight.[66] The exchange with shorter chains is possible during the adsorption process. On the other hand, the adsorption of polymers is irreversible when the adsorbed layers face pure solvent. In the case of uncharged or neutral polymer adsorption on the colloidal surfaces, there are three possible scenarios. The first one is the efficient amount of polymer adsorption on colloidal surfaces and thereby provided steric stabilization, the second one is the formation of flocculates caused by the bridging of the same polymer chain on two particles, and the third one is depletion due to no polymer adsorption on the surfaces. In the case of charged polymers, the electrostatic interactions between polymer/particle, polymer/solvent, and polymer/polymer need to be considered. Generally, charged polymers adsorb strongly on oppositely charged particles, but also charged polymers may also adsorb on surfaces of the same charge if the non-electrostatic affinity is strong enough to overcome the electrostatic repulsion.[67] When the process of homopolymers and copolymers adsorption is compared the adsorption of copolymers is very quickly at the contact with the surface whereas longer time is required for homopolymers adsorption, due to many surfaces–polymer encounters before adsorption or surface arrangement, so that specific surface sides can interact. The total adsorbed copolymer is also found to be higher than the values calculated for homopolymers.[68]

In the adsorptive surface functionalization method, the important system parameter is grafting density (or area per chain) ρ, which is the inverse of the average area available for each polymer at the surface. The grafting density also determines the conformation of the occupying polymers on the particle surface. In the case of low grafting densities, the polymers accommodate far apart from each other and hardly interact with each other when having mushroom conformation. For the higher grafting densities, the chains begin to overlap and the polymer extends away from the adsorbed surface in order to avoid each other and transformed to brush conformation with vertical height.[69]

In order to confirm the occurrence of polymer adsorption on particles, thermodynamic analysis between particle and polymer is carried by calorimetry and the extent of adsorbed polymers on the particle surfaces might be determined via thermogravimetric analysis methods.

Consequently, when the different surface modification methods are compared, one realizes that co-condensation method reduces time, energy, or other disadvantages of the post-synthesis modification. However, while one-pot co-condensation synthesis affects the structure and morphology of the particles due to

the existence of organic groups in the synthesis, the post-synthesis modifications do not affect much the size and size distribution of the particles.

2.2 The Role of Nanoparticles in Medicine

In the last decade, the fascinating developments within material science and collaborative interdisciplinary efforts to design novel nanoparticulate systems have provided advantages over molecular technologies in nanomedicine applications. In the literature, nanoparticles are extensively employed in biomedical applications and continue to be considered as a boon[70] for diagnosis and therapy. The flexible modification possibilities of nanoparticles aid to retain efficient solubility and colloidal properties to utilize in complexed biological environments (e.g. blood, tissues, etc.). The modest alterations in structure, surface modification, and affinity ligand choices prompt to plenty of advantages for sensing, imaging, and targeting of nanoparticles in biological systems.

In medicine, the successful disease combating requirements are listed as early detection of the lesion, identification of the disease with the aid of biomarker's signal that will help to choose right therapy and efficient delivery of therapeutic reagents to the lesion, and reduced unwanted side effects. Nanoparticles can easily meet all these demands in the nanomedicine platform. For instance, the essential event in most nanoparticle-based biomedical applications is the binding of a label or probe to the particles that will help to diagnose of the lesion area by tracking of nanoparticles with a measurable characteristic signal. Various types of nanostructures has been used for diagnostic purposes, including quantum dots, nanoshells, metal nanoparticles, carbon nanotubes, and cantilevers. These nanostructures might be employed for *in vitro* and *in vivo* diagnosis to meet the demands of clinical diagnostics for high sensitivity and earlier detection of disease. In this sense, nanoparticles have been considered to have the potential as novel intravascular or cellular probes for diagnostic (imaging) purposes.

The use of nanoparticle-based diagnostics has a great importance, especially for cancer treatment. For instance, biomolecule coated superparamagnetic iron oxide nanoparticles (SPION) are used for detecting cancer cells by magnetic resonance imaging. The presence of specific molecular markers on the particles bind to the cancer cells which induce a specific measurable signal is imaged by magnetic resonance imaging. Such technology helps to determine individual cancer cells months or years earlier than the conventional diagnostic tools and might be employed to find out residual or metastatic cancer cells after therapy.[71]

Besides using nanoparticles solely for imaging they can also be used to overcome the second demand, delivering therapeutic compounds to the lesion. In the drug delivery technologies, the traditional treatment by therapeutic agents has been reported to have poor solubility, lack of targeting to lesion site, non-specific

biodistribution, toxicity, and low therapeutic index.[72] These limitations and drawbacks can be overcome by integrating the therapeutic agent in nanoparticles to deliver to the place of action with the provided protection from rapid degradation and with enhanced concentration in lesion tissues. When the accumulation of therapeutic compounds in the targeted site is increased, consequently, the required doses of drugs become lower which helps to overcome the especially disparity problem between the dose of drug and its therapeutic results or toxic effects. In the literature, a variety of inorganic or organic nanostructures, such as liposomes, polymers, dendrimers, silicon or carbon materials, and magnetic nanoparticles, have been reported as carriers in drug delivery systems.[73]

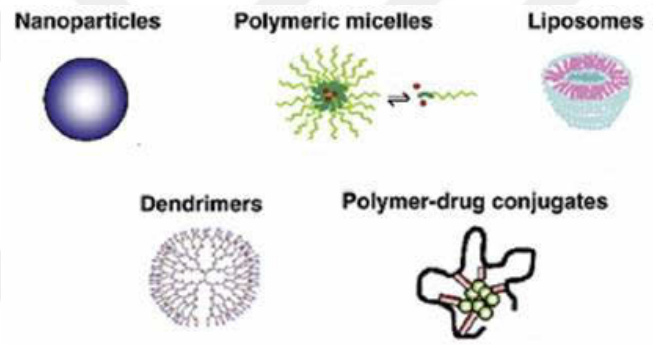

Figure 5. Types of nanostructures used for drug delivery in the literature (Adapted from reference [74]).

It is also possible to design nanoparticles as theranostic agents, which allow simultaneous diagnosis and therapy. The term "theranostic" is used to imply a proposed strategy that combines the diagnostic and therapeutic action. It was used by the Chief Executive Officer of PharmaNetics as a treatment strategy for the first time in 1998, to signify the concept of the ability to affect therapy or treatment of a disease state. The treatment strategy theranostic aims to monitor the response to treatment and increase drug efficacy and safety, which leads to individualized therapeutic strategies towards personalized medicine. In order to succeed in the mentioned strategy, the therapeutic and diagnostic capability needs to be combined into one single agent. Such combination agents can be provided with the offered opportunities of emerging nanotechnology. Accordingly, it was reviewed in the literature that theranostic nanoparticles should have at least three components, i.e., carrier, the payload for therapeutic intervention and surface modifier, depending on both their roles and their physical locations, as illustrated as in Figure 6.

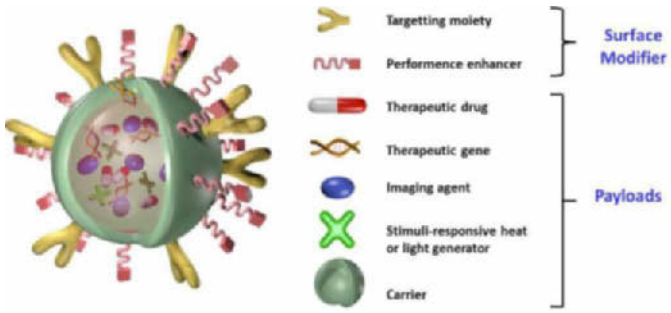

Figure 6. Schematic illustration of a theranostic nanocomposite.[75]

Although the field is relatively novel, numerous of nanoparticulate formulations are already in clinical trials and successfully marketed. [76, 77] The nanoparticulate formulations offer advantages over conventional therapeutics.[75] With the optimization of preparation techniques, achievements in the field of nanoparticles characterization and a better understanding of nanoparticles in complex biological environment has raised hopes for the use of nanoparticles as platform in medicine.[70]

2.2.1 Silica Nanoparticles in Biomedical Applications

Silicon is the most abundant element (27.2%) in the Earth's crust after oxygen (45.5%).[78] By virtue of its chemical and physical characteristics, silicon and its oxide forms take place in variety of industries, such as electronics, construction, food and biomedical industries. Among all these fields, biomedical applications attract great attention and grow rapidly. For instance, silicon-based materials have been employed as dietary supplements, implant, dental fillers, and contact lenses. [79] Especially the fundamental characteristics of silicon dioxide (silica)-based nanoparticles such as size (generally from 5 to 1000 nm), optical properties, high surface area, low density, adsorption capacity, capacity for encapsulation, biocompatibility, and low toxicity, make them widely utilized as an inert solid in diverse biomedical applications. [80] Therefore, silica-based nanoparticles offer numerous of advantages with its existing characteristics and prompt novel applications in biomedical research, such as biosensors, enzyme supporter, controlled drug delivery and release and cellular uptake in addition to its applications in protein adsorption and separation, gene delivery, imaging, and pharmaceuticals.

Recently, silica nanoparticles in the form of 'C-dots' (Cornell dots)[81] were US FDA approved for stage I human clinical trial.[82] Silica is an endogenous substance, especially abundant in bone, cartilage and other supporting tissue. Silica is 'generally recognized as safe' by the US FDA.[83]

There exist two common types of silica nanoparticles in the literature; solid silica nanoparticles (SiNP) and mesoporous silica nanoparticles (MSN) both of which consist of an amorphous silica structure. Both types are extensively used in biomedical research. [58] Researches on mesoporous and solid silica nanoparticles for biomedical applications has expanded greatly and various studies have been carried out regarding the application of them. When the ordered mesoporous silica materials are considered, there were initially developed for catalysis applications. However, its potential was recognized quickly by the researchers to be used in many different research areas, such as magnetism, sensors, optical materials, photocatalysis, fuel cells, thermoelectrics, and even in pharmaceutical field. One of the first attempts regarding the capability of mesoporous silica nanoparticles (MCM-41 type) to act as a reservoir for drug delivery was done by Vallet-Regí *et al.* in 2001.In the study, ibuprofen was employed as guest molecules and loaded into the pores of silica nanoparticles, and subsequently drug release in simulated body fluid was investigated.[84] Similar types of applications also take place in the literature for non-porous silica nanoparticles in which the guest molecules usually are linked to solid silica nanoparticles via covalent conjugation[85] or can be encapsulated in the silica matrix during the synthesis of particles.[86,87]

Especially after the introduction of MSNs, due to their intrinsic characteristics such as large surface area, high pore volume, tunable pore sizes, abundant inner/outer surface chemistries and biocompatibility, they gained great interest as probes for diagnosis, repair materials for tissue engineering, synergistic or radiosensitive agents for ultrasound therapy or radiotherapy. [88] Today the exploration of MSNs still continues as one of the hottest topics both for *in vitro* and *in vivo* research in the biomedical research field. Despite the existence of well-established *in vitro* research of MSNs, the *in vivo* assays of MSNs regarding to bio-safety, imaging and therapeutic efficiency to encourage the application of MSNs into preclinical stage were started in 2008 by Wu *et al.*.[89] The main reason for such delay is the complexity of *in vivo* physiological environment which makes it difficult to imitate and leads to less reproducible results. The other point regarding applicability of MSNs in clinical trials is the characteristics of MSNs. The design of MSNs should be well addressed to be utilized in the physiological environment because the bio-behavior of MSNs are strongly related to their preparation that varies the size, shape and surface chemistry of particles.[90] For instance, when MSNs are administered by intravenous injection the biodistribution and blood circulation time depend on the MSN's size and surface chemistry. The surface chemistry of MSNs also limits *in vivo* efficacy due to unspecific protein adsorption which leads to reticuloendothelial system (RES) uptake and elimination. [91, 92]

Consequently, recent developments in MSN-based theranostic designs have promoted the preclinical and clinical studies that contribute human health and personalized medicine platforms but still stronger cross-disciplinary collaborations are required to develop MSN based smart nanomedicine.

2.2.2 Modulations in Design of Silica Nanoparticles for Biomedical Applications

Physicochemical properties such as size, shape and surface characteristics of silica nanoparticles play a key role in biomedical applications. The physicochemical properties of silica nanoparticles help to predict their behavior during their *in vivo* journey and reaching the destination, biodistribution, intravascular and transvascular transport, and targeting capability to lesion sites.[93] The inherent properties of nanoparticles such as their surface modifications, surface to volume ratios, controllable shapes, and unique optical properties make them excellent candidates for future biomedical applications, and many efforts have been made to control these properties of silica nanoparticles which are the prerequisite for biomedical applications.[94]

2.2.2.1 Modulating the Size & Shape of Silica Nanoparticles

Among all the physicochemical properties of silica nanoparticles, controlling their size and shape is a significant issue because these properties strongly affect the efficacy of the particles in biomedical applications.[95] In the literature, studies with mesoporous silica nanoparticles (MSNs) have been carried out in order to investigate the effect of size and shape, especially on cellular uptake, and cytotoxicity. MSNs are favored for such research because tight control in their morphology can be achieved by the employed synthesis routes. Lu *et al.* reported MSNs cellular uptake is highly particle-size-dependent in the order 50>30>110>280>170 nm for the studied particle sizes, ranging from 30 nm to 280 nm.[96] In the study of Jiang *et al.* different cellular uptake efficiencies and mechanisms were observed for cervical cancer cell line (HeLa) with the altered MSN sizes and the most effectively internalized particle size was mentioned as 50 nm among the studied particle sizes.[97] On the other hand, regardless of particle type, even though smaller particle sizes induces facile cellular internalization still no size limit up to 5 μm is observed for the internalization of the particles.[98]

While the shape effect of MSNs is studied, two main categories are considered. The first one is the aspect ratio and the other one is morphology, as presented in Figure 7.

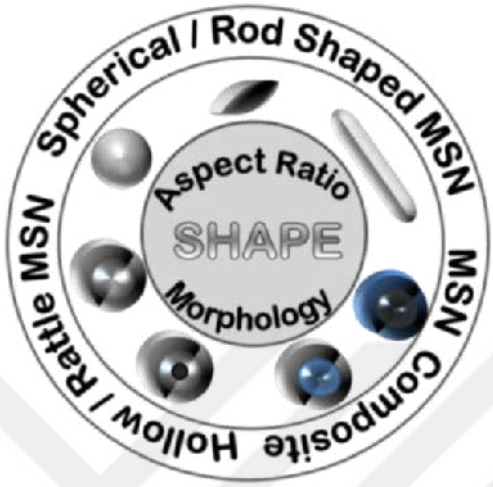

Figure 7. Mesoporous silica nanoparticles (MSNs) can be divided into categories by particle aspect ratio and morphology (Adapted from reference [99]).

Lately, MSNs with different aspect ratios have been thought to provide various inclination possibilities at bio-nano interfaces and higher internalization rate, longer circulation time and better therapy efficacy. [100], [101] In the study of Huang *et al.* [100] the shape effect of MSNs, with the aspect ratios (AR) 1, 2, 4, on cellular uptake and behavior was demonstrated. Their findings revealed that MSNs with larger ARs were internalized in a particular cell line by non-specific cellular uptake, in larger amounts with faster rates compare to other particles with smaller ARs, which were also internalized by non-specific cellular uptake. A possible explanation for this behavior was given as the differences in the curvature of the differently shaped MSNs. For example, when the longitudinal axis of rod-shaped NP interacted with cell membrane, a larger contact area is provided compared to spherical NPs. An additional suggestion on this topic is the resemblance of rod-like particles with rod-like bacteria, which could be a reason for the observed enhancement in internalization rates in non-phagocytic cells.[101] Moreover, the particles with higher ARs was found to have greater impact on different aspects of cellular functioning such as cytoskeleton organization and migration, cell proliferation and apoptosis. All in all, available results suggest that, as compared to their spherical counterparts, elongated nanoparticles can be more favorable for therapeutic applications.

2.2.2.2 Modifications on Surface Functionality of Silica Nanoparticles

The available surface modifications of silica nanoparticles allow precise control of surface chemistry to modulate surface charge, colloidal stability in suspension, anchoring for bio-functionalization (antibodies, proteins, peptides targeting ligands

and drug molecules), molecular gate-keeping, and stimuli responsiveness, controlled cleavage of surface-bound coatings or moieties. The ability to combine these properties makes silica nanoparticles an even more desirable platform for theranostic applications. The surface chemistry can be diversified by various methods, including covalent conjugation of complexes, co-condensation, surface grafting and physical adsorption of polymers.

Physical adsorption of small molecules, macromolecules like branched polymers, copolymers, dendrimers or phospholipids are also frequently used in the literature since they can provide higher amounts of functional groups than the ones provided by co-condensation and surface grafting methods.[102, 103, 104, 105]

The dispersion stability of silica nanoparticles is one of the relevant concerns with the surface modified silica nanoparticles which means silica nanoparticles should be stable in biologically relevant aqueous media without aggregation. Net surface charge primarily determines the dispersibility and stability of nanoparticles by electrostatic stabilization, where highly charged nanoparticles are necessary to provide colloidal stability.

The surface charge of the particles also plays a vital role to determine the fate of the particle's interaction with cells and biological environment. For instance, the net positive surface charge is attributed to be beneficial in maximizing cellular uptake, whereas net neutral charge is favorable for diminishing non-specific interactions in biological environments.[106] The net surface charge of silica nanoparticles also has a great impact on the *in vitro* cytotoxicity together with the dose and treated cell types.[107] The studies exploring the positively charged nanoparticles have shown that particles with positive surface charges penetrate cell membranes, regardless of the type of particle, which may contribute to the possible cytotoxicity of such particles.[106]

The surface characteristics of the silica nanoparticles can facilitate prolonged tracking of the particles and labeling of cells with the provided appropriate conjugating anchors for the dyes and also an environment for the incorporated dyes. As presented in the study of Rosenholm *et al.*[108], by employing different surface functional groups hydrophobic/hydrophilic fluorophore incorporation can be provided. In addition, surface characteristics of silica nanoparticles may contribute to the sustained release of loaded drug when the particles are employed in drug delivery. Hydrophobic and hydrophilic characteristics of silica nanoparticles may lead to varying of drug release profiles from the particles. [109,110]

The architecture of the accumulated groups on the surface of silica nanoparticles influences the control of nanoparticle interactions at the bio-nano interface and their fate within the biological system. Among various nanoparticle surface modification approaches, polyethylene glycol (PEG) is one of the most commonly used polymers, which has been proved as a successful strategy for stealth particle preparation and

prolonging the circulation times, [111] as well as improving the enhanced permeability and retention (EPR) effect. In order to provide high efficiency of the process, the conformation and surface density of the polymers are important along with other characteristics of the polymer i.e. chain length, layer thickness and molecular weight of the polymer.[112, 113]

Consequently, in light of literature investigations the structure and morphology of silica nanoparticles can be altered by controlling the synthesis steps of silica nanoparticles. Sufficient surface functionalization can be provided both with post- and one-pot co-condensation synthesis methods. When the surface modification methods are compared, one realizes that the post-synthesis modifications do not significantly affect the morphology of particles, whereas one-pot co-condensation synthesis affects the structure and the morphology of the particles. Therefore, it is beneficial to know the advantages and drawbacks of the aimed strategies, while synthesis and surface modification methods are being decided.

3 AIMS AND HYPOTHESIS OF THE STUDY

In this thesis, physicochemical characteristics of silica nanoparticles were used as a tool to facilitate the utilization of silica nanoparticles for biomedical applications. For this purpose silica nanoparticles were prepared with controllable physicochemical characteristics i.e. size, shape, structure, surface and composition. The influences of these features were examined for diagnosis and therapy applications.

The specific aims of the study were to :

- examine the effects of surface modifications on colloidal stability and redispesibility of silica nanoparticles in biologically relevant media and *in vitro* conditions

- enhance the drug loading capacity of silica nanoparticles by altering the structure of the nanoparticles

- improve therapeutic action of silica nanoparticles by employing targeted drug delivery strategy

- improve the imaging and cell labelling capability of silica nanoparticles by employing different surface modifications, altering the morphology of silica particles, and diversifying the incorporation strategy of imaging agents into the particles

- evaluate the interactions of shape and surface engineered silica nanoparticles in biological environment

The overall hypothesis is thus: silica nanoparticles can be prepared controllably and tailoring the aforementioned features of silica nanoparticles has an impact on facilitating their usage in nanomedicine.

4 CHARACTERIZATION METHODS

4.1 Dynamic Light Scattering

Dynamic light scattering method is one of the ensemble particle sizing methods by which the size of the particles are measured in suspension of the sample and the size distribution data is extracted from the obtained signal of the measurements.[114] Dynamic light scattering (DLS) is widely used to determine the hydrodynamic diameter of nano and micron sized particles in colloidal dispersions. The variations in the intensity of scattered light from a colloidal dispersion are measured on the microsecond time scale by DLS technique. The particles in dispersion undergo random thermal motion known as Brownian motion, which is related to the size of the particles. The motion is modeled by the Stokes-Einstein equation (Eq. 5) from the translational diffusion in the form most often used for particle size analysis.

$$D_H = \frac{kT}{3\pi\eta D_t} \qquad \text{Eq.5}$$

Where D_H is the hydrodynamic diameter of the particle, D_t is the translational diffusion coefficient, η is the solvent viscosity, T is the absolute temperature and k is the Boltzmann's constant.

The translational diffusion coefficient will depend not only on the size of the particle. So “core” is not the only determinant in dynamic light scattering measurements, but also the existing surface modifications, as well as the concentration of the sample and type of ions in the medium.

The shape of the examined particles has also a pivotal effect on the resulting hydrodynamic size, especially in the cases which the shape of the particles affects the diffusion speed. The changes in the width of rod-like particles will not affect the diffusion speed significantly, so will not result in a big difference in hydrodynamic size; whereas any small change in the length of a rod-like particle will directly affect the diffusion speed and the apparent size. In such cases, the obtained size value is the diameter of a sphere that has the same average translational diffusion coefficient as the particle being measured.

In this technique, usually a laser is used as a light source and shot through the sample. When the molecule and/or particles are hit the light, it causes a scattering of the light in different directions. In the rate of the intensity, fluctuation is measured and used to calculate the size of the particle. In order to interpret the intensity fluctuation data, a correlator measures the degree of similarity between two signals over a period of time. A correlation function plot is obtained by comparing the

intensity signal of a particular part of speckle pattern (where scattered light is detected) at one point in time and the one at a very short time later. In this way, strongly correlated intensity signals are obtained. Further in time, the compared signals will not be as good correlated as first-time points so the correlation will reduce in time and reach the zero-value. A typical correlation function against time is presented in Figure 8.[115]

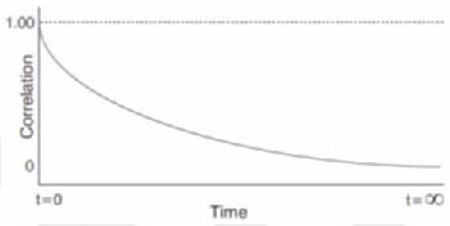

Figure 8. Illustration of dynamic light scattering correlation function of particles.[115]

After the correlation function is obtained, it is used to calculate the size distribution by knowing the rate of decay in the correlation function is related to particle size. The rate of decrease is much slower for large particles than it is for small particles. The decay rates for a number of size classes are extracted from the correlation function by using software algorithms and size distribution data is obtained. The relative intensity of light scattered by diverse classes of particle size is presented as intensity size distribution. The obtained intensity size distribution can be converted to number and volume size distribution (Figure 9) by considering the scattering light intensity and particle size relation described in Rayleigh approximation as the intensity of scattered light is proportional to the sixth power of the particle diameter.

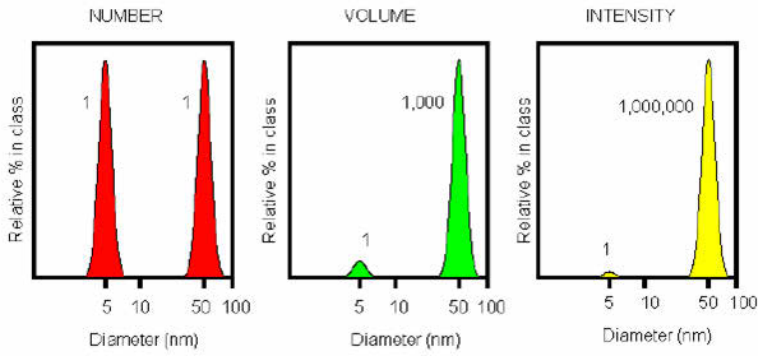

Figure 9. Particle size distributions for a sample containing equal number of 5 nm and 50 nm particles by number, volume and intensity.[115]

In the report of DLS results, the Z-average value is presented, which is the intensity weighted mean diameter derived from the cumulants analysis. Also, polydispersity index (PDI) is represented in the report as a measure of the size distribution broadness.

In this study, the presented size values are given as Z-average values, and in each measurement the PDI values are considered as a quality of analyzed sample suspension.

4.2 Zeta Potential Measurements

Zeta potential is an experimentally determined physical property of particles when they are suspended in a liquid media. In the liquid media, the particles are surrounded by an electrical double layer (Figure 10).

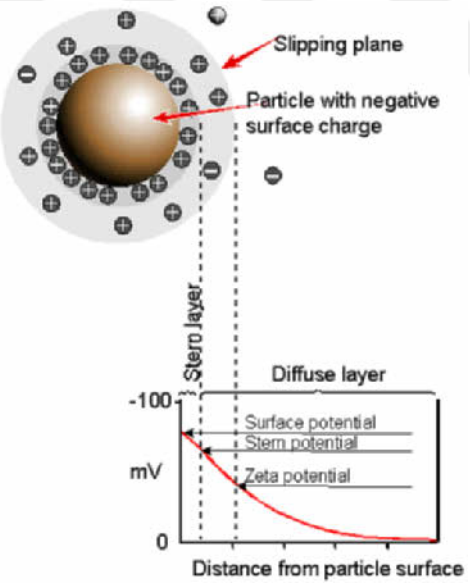

Figure 10. Illustration of ion distribution around charged particles in the dispersion.[116]

In the electrical double layer, ions with opposite charges adsorb on the particles surface and a net charge at the particle surface is formed which affects the distribution of ions in the surrounding media. The surrounding liquid layer of particles is composed of two parts; an inner layer known as Stern layer and an outer region named diffuse layer. The Stern layer consists of strongly adsorbed counter ions on the particle surface, whereas diffuse layer has both loosely associated positive and negative ions. In the electrical double layer, the strongly adsorbed ions (in the

Stern layer) are not mobile during the movement of particles in the liquid. When the particles move due to gravity or an applied voltage the ions, the Stern layer also move along with the particle. In the diffuse layer, there is a boundary called as Slipping plane and the ions beyond the boundary stay with a bulk liquid media The potential at this boundary is called zeta potential (ζ-potential). The magnitude of the zeta potential indicates the stability of colloidal suspensions. When the zeta potential value of the particles is highly negative or positive, it will aid to have well-dispersed particles in the liquid phase, that is, a stable colloidal suspension.

The zeta potential value also depends on the pH of the dispersion for the aqueous media. It is crucial to mention the pH of the media for the zeta potential measurements. As presented in Figure 11 the isoelectric point (IEP) of the colloidal systems can be determined by altering the pH of the dispersion. Isoelectrical point determination provides the information of the pH value at which the net effective surface charge is zero and it is a vital practical consideration for preparing stable colloidal systems. As shown in Figure 11 below, sufficient negative potential value provided when the pH value is higher than pH 7 (approx. -30 mV) and when the pH value is lower than 4 sufficient positive potential value (approx. +30 mV) is obtained to provide stable colloidal system which has the IEP at pH 5.5.

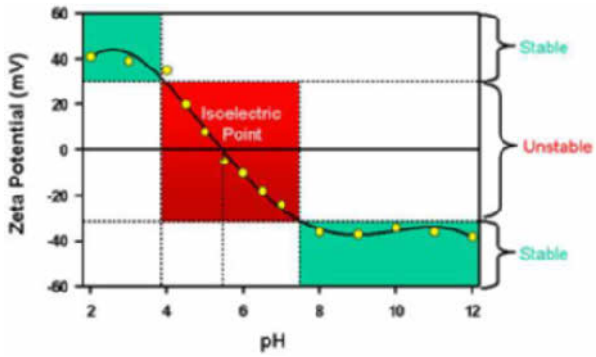

Figure 11. Typical plot of zeta potential versus pH showing the position of the isoelectric point and the pH values where the dispersion would be expected to be stable.[117]

Electrophoresis is the most widely used technique for zeta potential measurements by which the movement of charged particles can be measured with applied electric field. The direction and electrophoretic mobility (velocity) of the particles, which are dependent on the strength of the applied electric field, the dielectric constant of the liquid, the viscosity of the liquid and zeta potential can be

determined with this technique. Zeta potential value of the particles can be determined with the help of Henry equation (Eq. 6).

$$U_E = \frac{2\varepsilon\zeta f(\kappa a)}{3\eta} \qquad \text{Eq. 6}$$

UE is electrophoretic mobility, ζ is Zetapotential, is dielectric constant, η is viscosity of the dispersed media and κ(α) is Henry's function approaches value 1 for low of which represents the ratio of particle radius (a) to electrical double layer thickness (Debye length, 1/κ) of the particle, and for large values, it approaches 1.5.

In the present study, the zeta potential measurements were carried out at room temperature in buffer solutions, and the presented values are average of 3 sequential measurements, each with more than 10 runs.

4.3 Electron Microscopy

Electron microscopes are instruments that use a beam of electrons to image a specimen on a very fine scale. The topology, morphology, composition and crystallographic information of the objects can be obtained. The limitations of light microscopes in getting fine resolution and high magnification create the need of electron microscope development. Due to the fact that light microscopes use the photons of light to visualize the specimen, they are just able of magnification up to 1000-2000 times, whereas electron microscopy can show higher magnification up to 2 million times. This is a physical limit imposed by the wavelength of the light. Electron microscopes use a beam of electrons with a shorter wavelength than photons, therefore, they allow for the visualization of structures that would normally be not visible by light microscopy.

There are two types of electron microscopes, scanning electron microscope (SEM) and transmission electron microscope (TEM). In both types the mentioned steps are followed regardless of type; a stream of electrons is formed by an electron gun and accelerated in a vacuum towards the specimen. The stream is confined and focused using metal apertures and magnetic lenses into a thin, focused, monochromatic beam. The beam is focused on the specimen by a magnetic lens and the sample is irradiated by the beam. The interactions occur inside the irradiated sample, affecting the electron beam which is transformed into an image (Figure 12). However, there is also some operational diversity between SEM and TEM. In SEM, the beam of electron scans the surface of the specimen and the morphology and topology information is obtained; while in TEM the electrons are transmitted through an ultra-thin specimen, and this enables to examine fine details in the specimen.

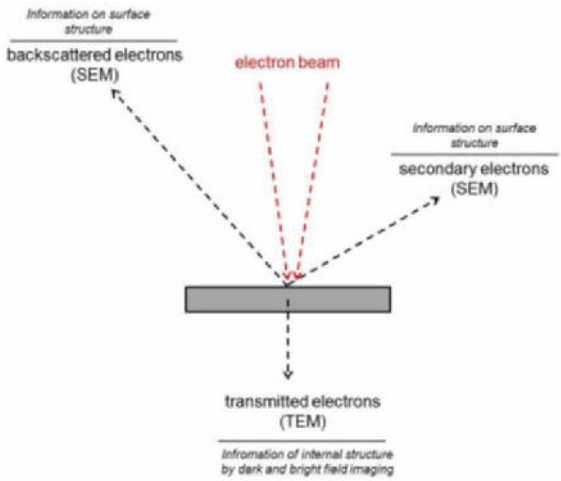

Figure 12. Schematic illustration of information produced by the interaction between specimen matter and the electron beam (Adapted from reference [118]).

In SEM, electron beam scans across the specimen and the electrons interact with the specimen. The two signals, back scattered electrons and secondary electrons are used to generate the SEM images. Elastically scattered electrons from the specimen are called back scattered electrons and the in-elastically scattered electrons, due to the loss in kinetic energy upon their interactions with orbital shell-electrons, are called secondary electrons. Electrons captured by the scintillator/ photomultiplier are then amplified and used to form an image in the SEM. When the electron beam knocks off the inner shell electron, the electron from higher energy levels drops to lower energy levels resulting into emission of Auger electrons, which are used to get information of the chemical composition of the sample. This technique is called as Auger electron spectroscopy (AES). The emission can also be in the form of photons known as X-ray photons and have high energy, which are used for the compositional analysis of the sample. This technique is known as energy dispersive analysis of X-ray (EDAX) and is used extensively to study the elemental composition of the sample.

In TEM, the specimen is illuminated by an electron beam, and electrons transmit through the specimen. As the electrons travel through the sample, they are either scattered or are transmitted unaffected through the sample. This results into a non-uniform distribution of electrons in the beam that comes out of the sample, which presents all the structural information of the sample. The transmitted electron beam strikes the fluorescent screen with the aid of magnetic lenses and generates an image with varying contrast. The darker areas with higher contrast are those from where

fewer electrons have been transmitted due to high density or thickness of the sample while the of lower contrast show the areas in the sample, which have less density or thickness, and thus more number of transmitted electrons are present. The obtained image is detected by CCD (charge-coupled device) in real time.

In this study, both SEM and TEM microscopy techniques were employed to investigate the size, morphology and mesoscopic structures of the samples. For SEM investigations, a thin layer of dried samples was mounted on copper tape and coated with carbon, gold or gold-platinum. TEM specimens were prepared on TEM grids as a drop from ready sample suspensions in order to provide thin layer.

4.4 Small-angle X-ray Diffraction (SAXRD)

The scattering of X-rays by (solid) materials provides a wealth of structural information in ångström level. The nature of knowledge depends on the scattering vector. The technique is constructed on how X-rays are diffracted by electron clouds of the atoms. The intensity of the scattered radiation is directly related to the electron density differences in the matrix. The position of diffraction peaks, their intensity, and their angular distribution provide information about the structure within a sample.[119] The position of reflections in the diffractograms aid to calculate the location of scattering entities by using Bragg's equation;

$$\eta\lambda = 2\, d_{hlk} \sin(\theta) \qquad \text{Eq. 7}$$

Where λ is the wavelength of the radiation, n is the integer number of the wavelength and d_{hkl} is the repeating distance between the lattices with indexes h, l, k and θ is the angle at which constructive interference occurs.

Different diffractograms are obtained for differently assembled lattice spacing of the samples. SAXRD analysis provides information about the mesoscopic ordering of the amorphous materials such as pore architecture of the mesoporous material.[120] Mesoporous materials exhibit lamellar, hexagonal or cubic pore orderings, which appears differently in diffractograms as presented in Figure 13.

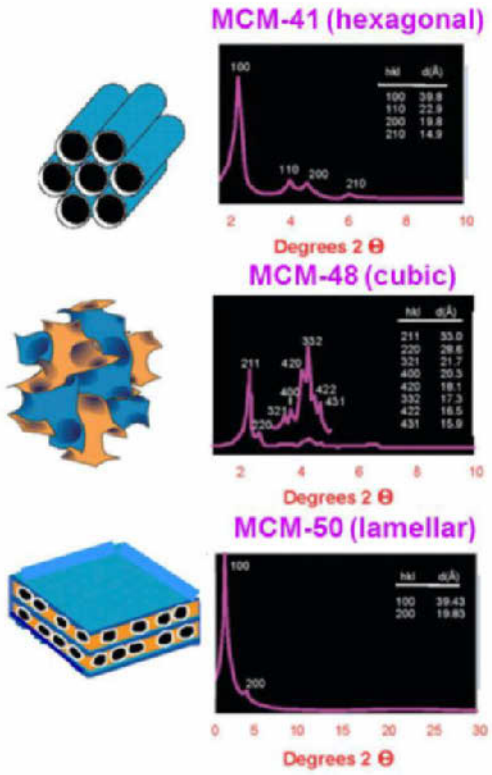

Figure 13. X-ray diffraction pattern of different mesoporous silica materials (Adapted from reference [23]).

In the lamellar structure, the repeating distance, *d*, directly gives the lattice (unit cell) parameter, *a*. The unit cell parameter, *a*, for the hexagonal network is obtained with Eq.8;

$$a = 2d_{hkl1}3^{-1/2} \qquad \text{Eq. 8}$$

where *a* (unit cell parameter) is the repeating distance between the centers of pores in the hexagonal structure. In this case, d_{hkl} is the d_{100} spacing as presented also in Figure 14.

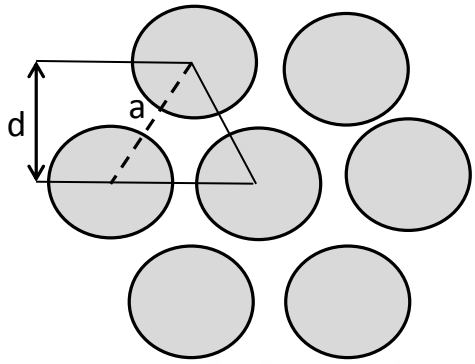

Figure 14. Schematic illustration of the hexagonal structure with the d_{100} spacing and unit cell parameter a.

By combining the obtained information from SAXRD analysis and N_2-sorption measurements for the hexagonal structured mesoporous materials, the mesopores wall thickness and also diameter can be evaluated.

4.5 Nitrogen Physisorption

Nitrogen physisorption analysis is one of the widely used methods that help to characterize porous structured materials. The technique gives information about the specific surface area, pore size distribution and pore volume of the material. Both routine controls and investigation of novel materials may be carried out by using existing user-friendly commercial equipment and on-line data processing.

In this method, the adsorption/desorption isotherms of nitrogen are first determined as a function of relative pressure (p/p_0) at the temperature of liquid nitrogen (～77 K). Then, further analysis of obtained isotherms provides the information about surface characteristics of the sample.

The isotherms can be obtained by using both discontinuous (point-by-point) and continuous approaches. The latter approach is more recent and dependent on the principle of 'quasi-equilibrium'. In this case, the introduction of the adsorptive is introduced slowly in order to obtain a continuous 'equilibrium' isotherm which provides the advantage to reveal inconspicuous features (e.g. sub-steps) that may not be detected by the discontinuous approach. In the discontinuous approach, successive amounts of the adsorptive are introduced and at each stage, the system is allowed sufficient time to attain equilibrium, which of course corresponds to a series of single points on the adsorption isotherm.[121] The amount of gas adsorbed by the solid is dependent on the equilibrium pressure, temperature and the nature of the gas-solid system. The existing relationship between all these are presented in graphical form and called as adsorption isotherm. According to IUPAC

classifications, there exist six different types of physical adsorption isotherms as presented in Figure 15.

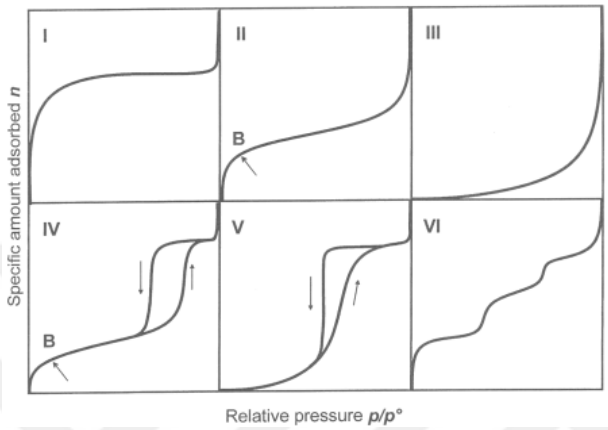

Figure 15. Six main types of gas physisorption isotherms, according to IUPAC classification.[122]

In discussing the adsorption isotherm types, it is expedient to classify pores according to their size, and mention that it is important to outgas the sample prior to analysis in order to eliminate most of the physisorbed species on the sample and to reach well-defined, reproducible state that is suitable for the purpose.[123] According to IUPAC, ultramicro pores have widths less 0.7 nm and micropores have widths in the range of 0.7 nm and 2 nm, mesopores in the range 2-50 nm. The largest pores are termed macropores, and have widths exceeding 50 nm, but these have less significance in the context of the physisorption of nitrogen.

Type I isotherms are observed for the adsorption of gasses on microporous solids, whose pore sizes are not much larger than the molecular dimensions. Enhanced adsorbent-adsorbate interactions occur in micropores of molecular dimensions. Limited range of pore sizes and the very small external surface is implied by he obtained horizontal plateau, which is attained by a narrow range of relative pressure. Type I isotherm signify that adsorption is limited to the completion of a single monolayer of adsorbate on the adsorbent surface.

Type II isotherms are obtained for non-porous and macropores adsorbents. Both monolayer and multilayer adsorption occurs. The knee point B is ascribed as where the monolayer adsorption ends and multilayer adsorption starts. With the aid of point B, the monolayer capacity can be estimated.

Type III isotherms are obtained for weak adsorbate-adsorbent interactions where adsorption hardly occurs.

Type IV isotherms are typical for mesoporous adsorbates, in which characteristic hysteresis effect is also observed due to capillary condensation inside the mesopores. The shape of the hysteresis loop between adsorption and desorption branches may vary due to the differences while filling and emptying the pores of different systems. Again, in this type of isotherm, point B can be considered as a point where the monolayer adsorption is completed and multilayer adsorption begins.

Type V isotherms indicate weak adsorbent-adsorbate interactions as in type III. Different type of hysteresis is caused by the filling and emptying the pores. For these materials usually, the pores are different in shape and size.

Type VI isotherms appear as a stepped isotherm. It is associated with the layer-by-layer adsorption on a highly uniform surface. Usually, non-polar molecules on uniform surfaces result in such isotherms.

By using the physisorption data, the specific surface can be determined. The most widely used procedure to obtain the specific surface area of porous and finely divided materials is by the application of Branauer-Emmett-Teller (BET) equation (Eq. 9).

$$\frac{p/p_0}{n(1-p/p_0)} = \frac{1}{n_m c} + \frac{c-1}{n_m c}\left(\frac{p}{p_0}\right) \qquad \text{Eq. 9}$$

n is the amount adsorbed at the relative pressure p/p_o and n_m is the monolayer capacity. The BET equation is essentially a multilayer extension of Langmuir theory. In order to calculate the specific surface area of the material the monolayer capacity, n_m, value from the BET plot is derived. Then, the specific surface area can be calculated from n_m with the knowledge of the average area, a_m occupied by each molecule in the completed monolayer (a_m for N_2 at 77K is taken to be 0.162 nm^2).

$$A_s(BET) = n_m \cdot N_A \cdot a_m \qquad \text{Eq. 10}$$

$$a_s(BET) = A_s(BET)/m \qquad \text{Eq.11}$$

where *A(BET)* is the total area and *a(BET)* is specific surface area respectively of the adsorbent with the mass m and Avogadro number N_A.

When the pore size determination is concerned, a variety of methods are proposed and extensively applied. The use of nitrogen adsorption for pore size analysis dates back to the late 1940s. Many of them relate the pore size with the pressure of the capillary condensation and evaporation, which is presented with the

Kelvin equation.[124] According to the classical Kelvin equation, the relative pressure can be given as function of mean radius of the meniscus (pore radius) as:

$$In\frac{p}{p_0} = -\frac{2\gamma V_L}{RT}\left(\frac{1}{r_m}\right) \qquad \text{Eq. 12}$$

where p/p_0 is the relative pressure, γ is the liquid/vapor surface tension, V_L the molar volume of liquid at temperature *T*, the gas constant R and r_m is the mean radius of the meniscus. After investigating the importance of adsorbed films on the pore walls during the adsorption process, the statistical film thickness (*t*) was introduced to the Kelvin equation as a correction and implemented in Barrett-Joyner-Halenda (BJH) method to calculate actual pore size distributions under the assumption of a cylindrical shape of pores (r_p). It is essential to consider the stability limit of the meniscus for the capillary condensation while estimating the pore diameter. The relative pressure p/p_0 =0.42 is considered to be the stability limit for capillary condensation and the capillary condensation of N_2 cannot occur at a relative pressure lower than 0.42 at 77 K. Therefore, theoretical basis for BJH analysis is fairly weak for the materials with pore sizes smaller than 4 nm since the adsorption-desorption steps lie below the lowest limit for the capillary condensation. Due to the inaccurate calculations of the BJH method especially for pore sizes below than 4 nm, and even large ones as 20 nm, alternative and more accurate methods developed to determine the pore size distributions; density functional theory (DFT).[125] Over the past few years, density functional theory (DFT) has become an important method for the characterization of porous materials. The approach is established on the assumption of the pores of different size all have the same regular shape (e.g. cylinders or slits) and generally each pore acts independently. The adsorbate is pictured as an inhomogeneous fluid, which is characterized by its density profile across the pore. The DFT creates equilibrium profiles for all locations inside the pore by minimizing the free energy. The interpretation is more complicated when the free energy is associated with both fluid-fluid and fluid-solid interactions which can be obtained, and become more accurate by non-local density functional theory (NLDFT). NLDFT method allows the calculation of pore sizes from micro- to mesopores.

In this work, nitrogen sorption measurements were performed to determine the structural parameters related to the mesoporosity (surface area, pore size, and pore volume) of prepared particles and data analyzes was carried out with AS1Win software (Version 2.02, Quantachrome Inst.). BET and NDLFT theories were

employed to determine the specific surface area and pore size and pore size distribution of the particles.

4.6 Spectroscopic Methods

Study of the the interaction between radiated energy and matter is principally named as spectroscopy. Historically it is originated from the pass of a narrow beam of sunlight through a triangular glass prism and the white light is dispersed into a visible spectrum of primary colors according to its wavelength. Then, the notion was expanded to cover any interaction with radiative energy as a function of its wavelength or frequency. Spectroscopic data is often presented by a spectrum, a plot of the response of interest as a function of wavelength or frequency.

Many sub-disciplines exist in spectroscopy, each with numerous approaches of specific spectroscopic techniques. The approaches can be classified according to the type of radiation energy, nature of interaction and type of interacted materials.

In many applications, the spectrum is obtained by the changes in the intensity or the frequency of the incident radiative energy as a result of interactions. The radiative energy types may vary according to its source as; electromagnetic radiation, particles (due to their Broglie wavelength), pressure waves and mechanical methods.

The spectroscopic techniques are classified according to the wavelength of the incident radiation as presented in the electromagnetic spectrum in Figure 16 and include microwave, infrared, visible and ultraviolet, x-ray and gamma spectroscopy.

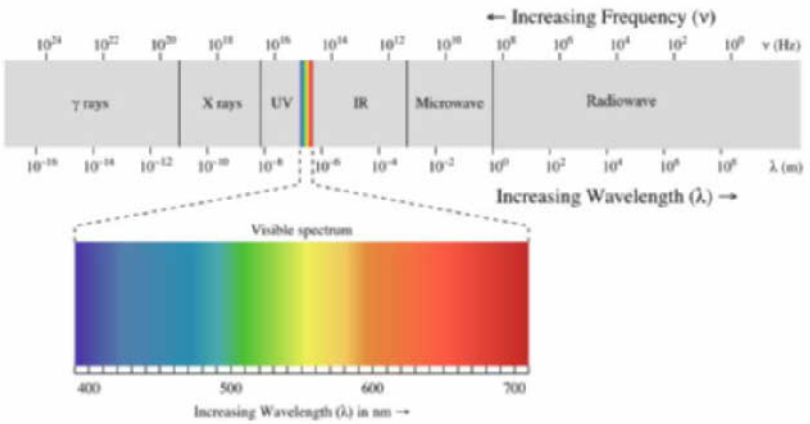

Figure 16. Electromagnetic spectrum as a function of wavelength and frequency with the detailed visible region (Adapted from reference [126]).

Types of spectroscopy can also be distinguished by the nature of the interaction between the energy and the material. These interactions are named as in Figure 17.

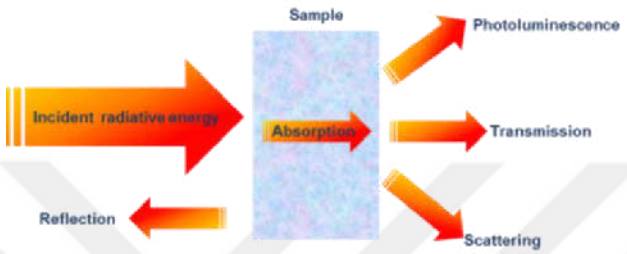

Figure 17. Interactions of radiation and matter.

Absorption occurs when energy from the radiative source is absorbed by the material. Absorbance is a quantitative measure which is expressed as;

$$A_\lambda = \log_{10} \frac{I_0}{I} \qquad \text{Eq.13}$$

where A is the absorbance at a certain wavelength (λ), e and I_o is the incident light before the interaction with the sample and I is the transmitted light through the sample. Absorbance is closely related to transmittance T, the ratio of the intensity of transmitted light and incident light (I/I0) and given as,

$$A_\lambda = \log_{10}(T^{-1}) = \log_{10} T \qquad \text{Eq. 14}$$

In absorption spectroscopy, a photon absorbed by an atom or molecule and results in a transition from a lower-energy state to a higher energy state or excited state as presented in Figure 18. The type of transition is depicted by the photon's energy. Electrons are promoted to higher electron levels by ultraviolet or visible light, changes in vibrational energy and rotational energy are caused by infrared lights and microwaves, respectively. When an atom or molecule in excited state returns to a lower energy state, the excess energy often is released as a photon and the interaction is called as emission (Figure 18). There are several ways in which an atom or molecule may end up in an excited state, including thermal energy, absorption of a photon, or by a chemical reaction. Emission following the absorption of a photon is also called photoluminescence, and that following a chemical reaction is called chemiluminescence.

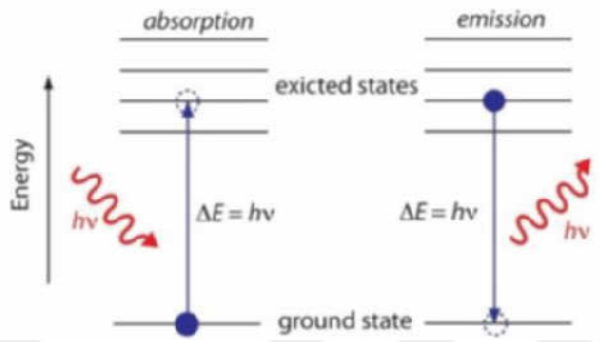

Figure 18. The energy diagram to present the absorption and emission of a photon by an atom or a molecule.[126]

Measuring the concentration of an absorbing species in a sample is accomplished by applying the Beer-Lambert Law. The Beer-Lambert law is the linear relationship between absorbance and concentration of an absorbing species. The general Beer-Lambert law is usually written as:

$$A = \varepsilon \cdot b \cdot c \qquad \text{Eq.15}$$

where A is the measured absorbance, ε is the molar absorbtivity ($Lmol^{-1}cm^{-1}$), b is the path length of the sample that is, the path length of the cuvette in which the sample is contained and c is the concentration of the compound in solution($molL^{-1}$).

Scattering takes place when the radiation deviates from its straight trajectory after interaction with the matter and reflection is the change in direction of a wavefront after interaction of the radiation with the material. Determination of elastic reflection or scattering of incident radiation is carried out in elastic scattering and reflection spectroscopy which aid to examine the arrangement of atoms in solid crystals. Crystallography employs the scattering of high energy radiation, such as x-rays and electrons.

In spectroscopic studies, radiant energy may interact with atoms, molecules, and nuclei which are named as techniques according to interacted matter type. Atomic spectroscopy was the first developed application of spectroscopy in which visible and ultravisible lights are involved in both atomic absorption spectroscopy (AAS) and atomic emission spectroscopy (AES). The atomic spectral lines are obtained with the techniques due to electronic transitions of outer shell electrons from one electron orbital to other caused by the absorption and emission interactions. The atomic spectral lines aid to quantify and identify the elemental composition of the sample since atoms of different elements have distinct spectra. Modern

implementations of atomic spectroscopy to study visible and ultraviolet transitions were carried out by flame emission spectroscopy, inductively coupled plasma atomic emission spectroscopy, glow discharge spectroscopy, microwave induced plasma spectroscopy, and spark or arc emission spectroscopy.

The interaction of combined atoms formed into molecules and radiative energy creates unique types of energetic states, and also spectra of transitions between the energetic states is known as molecular spectroscopy. Molecular spectra can be obtained due to electron spin states (electron paramagnetic resonance), molecular rotations, vibrations and electronic states. Rotations are collective motions of the atomic nuclei and typically lead to spectra in the microwave and millimeter-wave spectral regions; rotational spectroscopy. Vibrations are relative motions of the atomic nuclei and are studied by both Infrared and Raman spectroscopy.

When the nuclei of atoms absorb and reemit the electromagnetic radiation in a magnetic field distinct nuclear spin states are obtained which lead to gamma ray spectra. This selective technique is called as nuclear magnetic resonance (NMR) spectroscopy that eases to determine the structure of many compounds. It helps to distinguish among many atoms within a molecule or a collection of molecules of the same type, but which differ only in terms of their local chemical environment. NMR spectroscopy is used to identify known and novel compounds.

In thesis, UV-VIS spectroscopy was employed to determine the drug loading efficiencies on the particles and also determine the drug release profiles from the particles when they are designed as drug carriers. In addition, the same technique was employed in order to quantify the amount of fluorophores on the fluorescent particles. The success of specific ligands conjugations on the particles was confirmed by this spectrometric method. In these experiments, the absorption spectra of the interested molecules were recorded on UV-VIS spectrophotometer with the help of standard curves prepared at different concentrations. The fluorescence intensity of labelled particle suspensions was determined by fluorescence spectrometry by dispersing them in various media at certain concentrations. Fourier transforms infrared spectroscopy (FTIR) and NMR was employed to quantify the structural confirmation and the composition of the in-the-house prepared copolymers respectively. Inductively-coupled plasma atomic emission spectrometry (ICP-AES) was employed to analyze the extent of paramagnetic Gd (III), in the particles when the particles are designed as contrast agents.

4.7 Isothermal Titration Calorimetry

Isothermal titration calorimetry (ITC) is an approach that examines the heat exchange accurately during a chemical or biochemical reaction. The technique provides information about the changes in enthalpy (ΔH) and entropy (ΔS) of the process as well as the characterization of interactions such as binding affinity (K_a) of macromolecules and ligands.

In the isothermal titration experiments, a sample solution containing a reactant is titrated with another reactant at an appropriate temperature. After each addition of the titrant absorbed or released heat is monitored by the calorimeter and the recorded heat changes are used as an indication of interactions.

The quantitative characterization of the energetic processes associated with the accompanying reaction is carried out by the thermodynamic analysis of the observed heat changes.[127, 128] Therefore, ITC became the instrument of thermodynamic analysis of molecular interactions, the knowledge about ΔH, ΔG, and the ΔS can be obtained in one experiment (Figure 19). Furthermore, there is no size limitation on the investigation molecules and the experiment can be conducted in turbid or colored solutions or in the presence of suspensions.

.

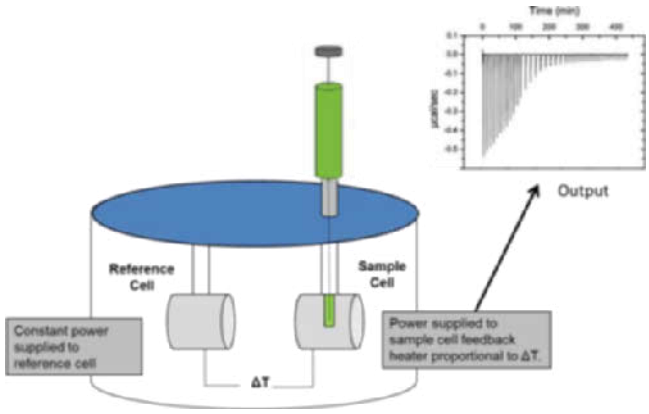

Figure 19. ITC instrument performing a titration. When an injection is made, the change in heat associated with binding (endothermic or exothermic) results in a change in temperature in the sample cell. A change in power (heat/s) is required to return the cells to identical temperatures. This change in power is recorded as a series of injections is made. The inset presents a heat signal after each injections and how it reduces due to the saturation of binding sites.

In thesis, polymer adsorption on nanoparticles was investigated Isothermal Titration Calorimetry (ITC) by titrating the polymer solution into a calorimetric

vessel containing particle dispersion and recording to the occurring enthalpy changes with. The differential enthalpy changes were calculated with the help of the software DIGITAM 4.1. The differential enthalpy change is considered to reflect different interactions between the polymers and the particles and hence might give an indication of the adsorption process.

4.8 Thermogravimetric Analysis

Thermogravimetric Analysis (TGA) is a technique in which mass change of the specimen is monitored either as a function of increasing temperature or isothermally as a function of time in a controlled atmosphere. TGA mainly provide information about the characteristics of materials that exhibit either mass loss or gain due to decomposition, oxidation, or loss of volatiles. TGA is also employed to get information about the temperature at which phase transitions take place during combustion and/or evaporation of sample. Common approaches of TGA are (1) studying the degradation mechanisms and reaction kinetics, (2) characterizing materials with the analysis of characteristic decomposition patterns, (3) determining the organic and/or inorganic (e.g. ash) content in the sample, which might aid to predict sample structures or simply used as a chemical analysis.

In TGA analysis, reproducibility is an important matter in order to compare one set of data to another. There some operating variables in TGA, which are calibration, specimen preparation, furnace cleanliness, temperature scanning rate, temperature range and analysis atmosphere, can contribute to reproducibility. The appearance of TGA-curve may differ with any change in the given variables, therefore, it is crucial to choose same temperature programming for the run of samples whose data sets are going to be compared.[129]

TGA-Netzsch STA 449F1 Jupiter instrument was used in this study in order to find out the extent of surface modifications on dried samples. The recorded thermograms were analyzed with the help of software Proteus 5 in order to estimate surface modification degree on the samples.

5 RESULTS AND DISCUSSION

5.1 Silica Nanoparticles with Diverse Size and Morphology

In the thesis, silica nanoparticles with spherical and rod-like shapes, porous, non-porous and hollow structure were prepared on the submicron scale for biomedical approaches. The morphology and size of silica nanoparticles were altered by controlling the hydrolysis and condensation steps of the sol-gel approach. Spherical non-porous silica nanoparticles (SiNP), spherical mesoporous silica nanoparticles (MSN), rod-like mesoporous silica nanoparticles (NR-MSP) and, additionally, hollow structured spherical mesoporous silica nanoparticles (H-MSN) were abbreviated as given.

Spherical non-porous silica nanoparticles (SiNPs) were formed by Stöber method which consists of an ethanol/NH_3/TEOS mixture.[130] 100 nm sized SiNPs were obtained by modifying the Stöber procedure. The obtained SiNPs were synthesized for Paper I, named as 100 SiNP, in order to evaluate the utilization of PEG-PEI copolymers for the facilitation of silica nanoparticulate systems in biomedical applications. There, 100 SiNPs were employed as, in nanotechnology definitions, 100 nm is typically taken as the 'classical' cut-off value.[131] In addition, SiNPs aid to avoid the complexity of porous surfaces in MSNs during the investigation of the surface functionalization process. Moreover, the 100 nm sized SiNPs can be considered as a model for nanoparticles in biomedical applications. Similarly sized and bigger SiNPs were also prepared for SUPPORTING PAPER III. They were employed to investigate their interaction with living cells by establishing correlations between their physicochemical properties and their potential to induce toxicity with respect to cellular viability, oxidative stress, and hemolysis.

In this thesis, MCM-41 type mesoporous silica nanoparticles with different characteristics (size, shape, mesoscopic orderings, and surfaces) were prepared in order to investigate their behavior in the bio-relevant environment. The studies were started with the synthesis of mesoporous silica nanoparticles (MSNs) with pore sizes about 3 nm and BET surface area higher than 1000 m^2/g. In MCM-41 type MSNs synthesis, cetyltrimethylammonium bromide (CTAB) was used as structure directing agent and tetraethylorthosilicate (TEOS) was the silica precursor. In the optimization of MSNs synthesis protocol absolute ethanol was added to aqueous basic reaction solution at various portions. In this synthesis protocol ethanol was employed as co-solvent to promote the desired size, of particles with the slight modification of the synthesis protocol described by He *et al.*.[132] In the reference study of He *et al.*, the synthesis was carried out in basic aqueous condition with the following molar composition of reagents: 1 TEOS/ 0.31 NaOH/ 0.122 CTAB/ 1186

H_2O. In their study, MSNs with the sizes about 150 nm and high mesoporous channels and 863 g/m^2 BET surface area was obtained.

In the unpublished experimentation part of the thesis, the synthesis protocol of the He *et al.* study was modified as follows. Alcohol was added to reaction solution as the co-solvent to provide better miscibility for TEOS and water, and facilitating the hydrolysis during the reaction. When the precursor and the water are mechanically mixed, a single phase mixture can be obtained by the addition of alcohol, which induces the reaction. During the optimization of the synthesis protocol, the added amount of ethanol was increased as: 10 $v/_V$%, 15 v/v%, 20 v/v %, 25 v/v%, 40 v/v % in the reaction. After the synthesis of the series of MSNs, the particles were collected by centrifugation n solution and washed with acetone after which calcination at high temperature (550 ◦C) was carried for 6 h in order to remove SDAs. The morphology of the particles was explored by SEM imaging. According to the unpublished images presented in Figure 20, spherical and non-aggregated MSNs were obtained with the addition of absolute ethanol to the MSN synthesis solution between the ranges of 15-25 v/v %.

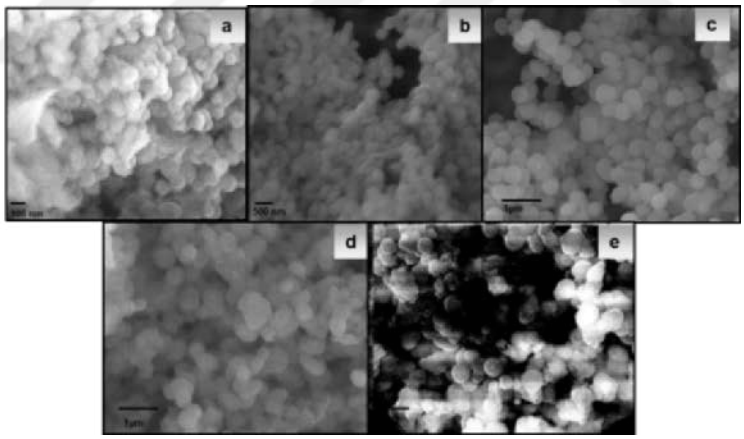

Figure 20. SEM image of a)10 v/v% b)15 v/v % c) 20v/v % d)25 v/v e)40 v/v % ethanol content in modified MSN synthesis of the He et al. study. [132]

Hydrodynamic sizes and the polydispersity indices (PDI) of MSNs series were determined by redispersing them in HEPES buffer solution (25 mM at pH 7.2) with ultrahigh sonication treatment. The lowest PDI value of 0.3 was obtained for the MSNs that was produced by the synthesis protocol containing 20 v/v% ethanol as co-solvent in the reaction solution. The Z-average value of the DLS measurement was about 700 nm (as presented Figure 21).

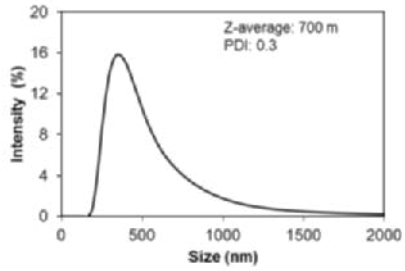

Figure 21. Hydrodynamic size distribution of MSNs (Figure 20c) in HEPES buffer solution.

In the unpublished experiments of the thesis, various post-synthesis treatments, before SDAs removal, were applied for the further optimization of the MSNs synthesis protocol. In Table 1 the steps of these post-synthesis treatments were given in detail for the MSNs (obtained with the 20 v/v% ethanol content in the synthesis).The hydrodynamic size values and ζ- potential values of the differently treated particles suspensions were listed. In the MSNs synthesis optimization part of the unpublished investigations, the elevated temperature 80 °C was also lowered to 30° C in order to ease the synthesis conditions. Moreover, different portions of (3-aminopropyl)triethoxysilane (APTES) were co-condensed with the portions 0, 1, 10 mol % of added TEOS. The aim of altering the APTES content in the synthesis solution was to provide functional groups for further modifications and also to alter the net surface charge of the MSNs in the suspension. As presented in Table 1, good redispersibility for the particles was obatined when they were treated with vacuum drying–calcination (C), and solvent extraction protocols (D) as post-synthesis treatments, which was assigned by the low PDI values.

Table 1. Description of the varied MSN synthesis and obtained hydrodynamic size (nm) and ζ- potential results for the MSNs in HEPES buffer solution.

Samples	Explanation for the prepartion protocols	PDI	Z-average [nm]	Zeta Potential [mV]
0-MSN-A	1-no APTES addition 2- collect particles by centrifugation 3- redisperse them in water with high sonication 4- freeze dry over night 5- calcination @550 C for 6h.	0,73	673	-44
0-MSN-B	1-no APTES addition 2- collect particles by filtration 3- freeze dry over night 4- calcination @550 C for 6h.	0,55	498	-40
0-MSN-C	1-no APTES addition 2- collect particles by centrifugation 3- wash with acetone 4-vacuum dry overnight 5- calcination @550 C for 6h.	0,29	244	-38
0-MSN-D	1-no APTES 2- collect particles by centrifugation 3- wash with acetone 4-solvent extraction in ethanolic NH_4NO_3 for three times. 5- Overnight vacuum drying .	0,304	546	-27
1-MSN-A	1-1 mol % APTES 2- collect particles by centrifugation 3- redisperse them in water with high sonication 4- freeze dry over night 5- calcination @550 C for 6h.	0,42	473	-35
1-MSN-B	1-1 mol % APTES addition 2- collect particles by filtration 3- freeze dry over night 4- calcination @550 C for 6h.	0,38	341	-34
1-MSN-C	1-1 mol % APTES addition 2- collect particles by centrifugation 3- wash with acetone 4-vacuum dry overnight 5- calcination @550 C for 6h.	0,36	291	-33
1-MSN-D	1-1 mol % APTES addition 2- collect particles by centrifugation 3- wash with acetone 4-solvent extraction in ethanolic NH_4NO_3 for three times. 5- Overnight vacuum drying .	0,24	426	-10
10-MSN-A	1-10 mol % APTES addition 2- collect particles by centrifugation 3- redisperse them in water with high sonication 4- freeze dry over night 5- calcination @550 C for 6h.	0,41	532	-40
10-MSN-B	1-10 mol %APTES addition 2- collect particles by filtration 3- freeze dry over night 4- calcination @550 C for 6h.	0,36	418	-39
10-MSN-C	1-10 mol % APTES addition 2- collect particles by centrifugation 3- wash with acetone 4-vacuum dry overnight 5- calcination @550 C for 6h.	0,25	325	-37
10-MSN-D	1-10 mol% APTES addition 2- collect particles by centrifugation 3- wash with acetone 4-solvent extraction in ethanolic NH_4NO_3 for three times. 5- Overnight vacuum drying .	0,15	539	22

The influence of post-synthesis treatments on the mesoscopic ordering of MSNs, prior to calcination, was investigated with SAXRD measurements in the unpublished investigations of the thesis. The samples were analyzed before and after the calcination processes. The presented diffractograms, (Figure 22) from the unpublished data of the thesis, revealed that the treatments coded A, B, C before calcination do not cause any distortion in the mesostructure ordering of the MSNs for the 10-MSN series, whereas already slight distortions were observed for 0-MSN, 1-MSN series. However, after the calcination of the same samples, the alterations become more obvious in the diffractograms, as presented in Figure 23. Treating the non-APTES MSNs (0 series) by ultra-sonication before calcination (the treatment coded A) is harsh for the porous structure even before calcination. After the calcination, no pore ordering was observed for B and C treatments. The reason for such an observation could be the shrinkage during the calcination. Only the treatment coded D (which is solvent extraction) helps to preserve the porous structure ordering, which results in an increase in *d*-spacing compared to untreated 0-MSN. For the synthesis of MSNs, it seems the addition of APTES (series 1 and series 10) to the synthesis solution aids to preserve the porous structure of MSNs even after various post-synthesis treatments. The reason for such an observation was given as APTES being able to strengthen the assembly between the template and silica sources, due to the hydrophobic packing by the aminopropyl groups of the APTES, which also yields high mesoporous ordering.[133]

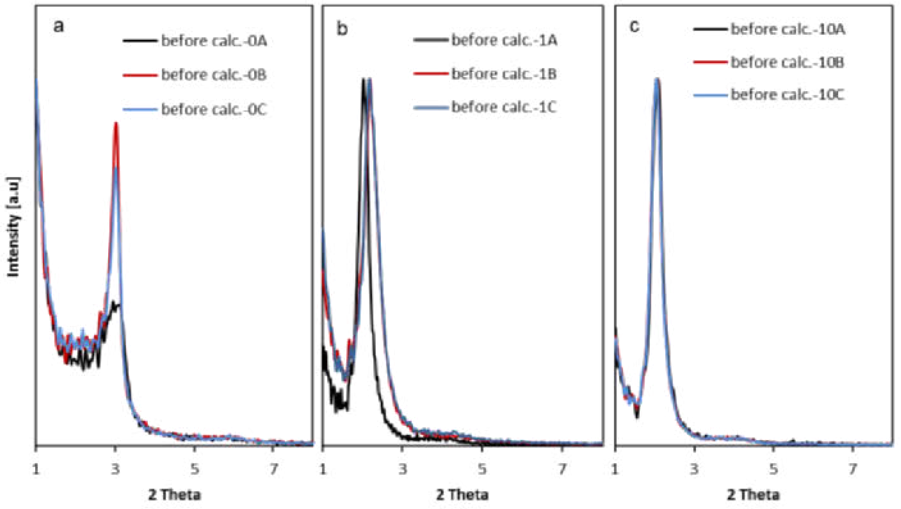

Figure 22. SAXRD diffractograms of MSN series after post-synthesis treatments and before calcination.

For the 1-MSN series, no significant changes were observed due to post-synthesis treatments prior to calcination (Figure 22b) and no change in the *d*-spacing values was obtained, whereas variations were observed after calcination process. (Figure 23b) The peak positions were shifted from 2.02, 2.18, 2.17, 2.17 to 2.08, 2.68, 2.66, and 2.14 for the 1- MSN series respectively. As seen in Figure 23b there is a clear shift in the peak positions of 1B and 1C preparations after the calcination process. These results are ascribed to the shrinkage of the pores of MSN during the calcination process. In the series 10-MSN, the ultrasonication process does not cause any significant distortion as in the other series (Figure 22c*)*. The distortions become obvious after the calcination process for all type of post-synthesis treatments, except solvent extraction (10D-MSN).

The deduced information from the unpublished investigations of the thesis helped us to derive detailed information about the critical points of MSNs preparation, which were also adopted for the material preparations in Paper II, Paper IV, Paper V, and Paper VI.

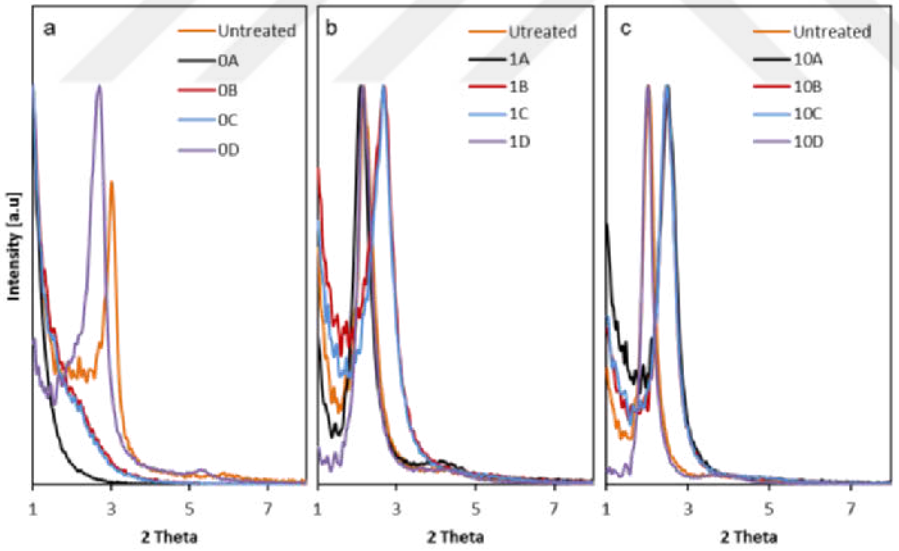

Figure 23. SAXRD diffractograms of MSN series with different post-synthesis treatments and calcination.

The morphology and aspect ratio of MSNs were altered as presented in PAPERs II, III, and IV. The rod –shaped mesoporous silica nanoparticles (NR-MSPs) were provided by our collaborators from Linköping University, Sweden. The particles were used either as pristine or with surface modification to compare them with the

spherical shaped MSNs. The morphological overview and the mesoscopic properties with the hydrodynamic radius value in a water suspension of the NR-MSPs were given in Figure 24.

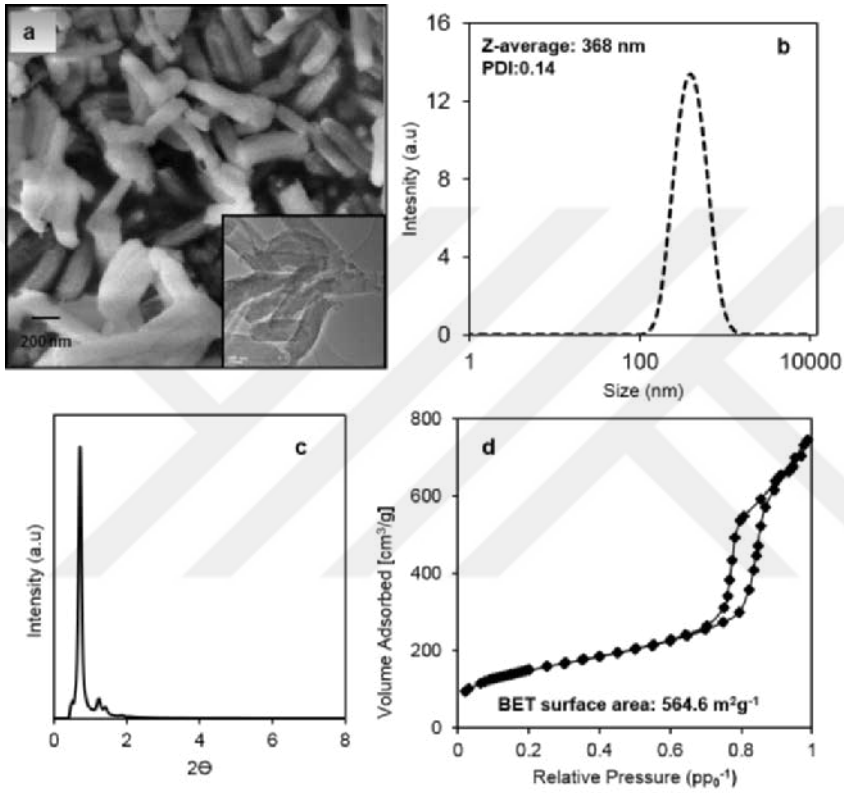

Figure 24. a) SEM images of NR-MSP, inset TEM images, b) Hydrodynamic size distribution of NR-MSP in aqueous suspension, c) SAXS diffractogram of NR-MSP, d) N2 sorption isotherm of NR-MSP.

Additionally, hollow-structured mesoporous silica nanoparticles (H-MSN) were prepared with the modulation of the MSNs synthesis conditions, as explained below in the text. The synthesis of H-MSNs was carried as one–pot hard/soft template-free, enlarged pore sizes as explained in PAPER V. For the preparation of pore expanded H-MSN, the inhomogeneous nature of the silica network was taken as an advantage which was obtained by the incorporation of pore swelling agents and aminosilane reagents into the synthesis solution of MSNs. Especially by considering the difference in the condensation degree of the silica framework between the interior and shell section, we were able to fabricate H-MSNs by inducing preferential dissolution of the less-condensed silica sections. The selective etching/dissolution

was generated as an *in situ* hydrothermal treatment of the MSNs in the synthesis solution.

In the synthesis of H-MSNs, tetraethyl orthosilicate (TEOS) and (3-aminopropyl)-triethoxysilane (APTES) were employed as silica sources and the reaction was carried out in basic ethanol solution in which decane and 1,3,5-trimethyl benzene (TMB) were employed to form pore-expanded MSNs by introducing these hydrocarbons into the cylindrical micelles.[134] After an overnight reaction at room temperature, the solution was hydrothermally treated *in situ* at an elevated temperature of 70°C for 48 h. The organic template of the particles was removed by calcination (550 °C, 2.5 h). The morphology of the generated H-MSNs was investigated by SEM and TEM images as presented in Figure 25.

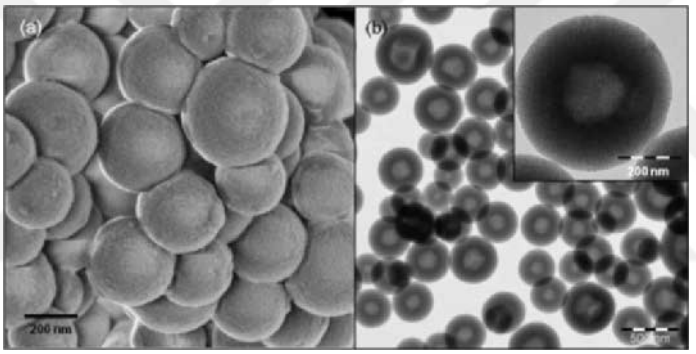

*Figure 25. Electron microscopy images of H-MSN a) SEM, b) TEM, b-inset zoomed-in view (*PAPER V*).*

The obtained particles are spherical in shape as shown Figure 25 with an average diameter of around 350 nm, as also measured by DLS in Figure 26. The hydrodynamic diameter distribution exhibits a narrow peak centered at 460 nm, further supporting the size uniformity of H-MSNs. A noticeable contrast between the interior section (150 nm in size) and the shell was found in the TEM image, which confirms the formation of the hollow structure. The shell of the particles has perpendicularly aligned mesopores and a typical IV nitrogen adsorption/desorption curve, was obtained for H-MSN with a high pore volume around 1.35 cm^3g^{-1} and mesoporous shell size of ~5 nm(calculated by NLDFT method) indicated by a steep increase of adsorbed nitrogen at relative pressures the (pp_0^{-1}) ranging between 0.4 and 0.5. An additional observation was H1-type hysteresis loop in a type-IV isotherm, where the adsorption and desorption branches are almost horizontal and parallel within a wide pp_0^{-1} range from 0.5 to 0.9 which is also characteristic of hollow spheres.

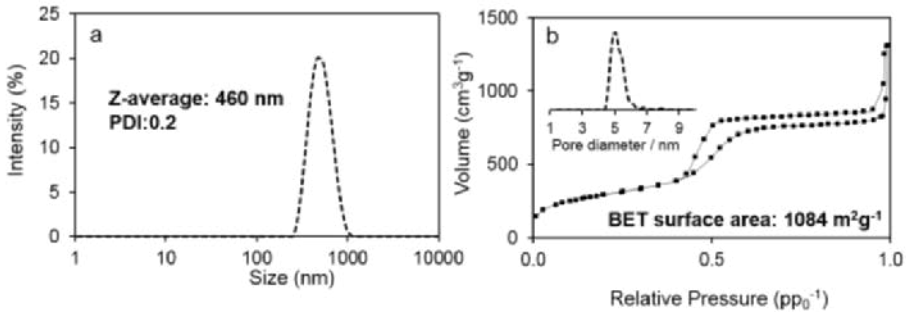

Figure 26. a) Hydrodynamic size distribution (b) N_2 sorption isotherm of the prepared H-MSN together with pore size distribution (PAPER V).

In this part of the study, our focus was also laid on the formation mechanism of the H-MSN architecture. A recent study by Wong and co-workers[135] have demonstrated that the silica shell on nanoparticles formed by a typical Stöber method (ethanol/water/NH_3/TEOS) is inhomogeneous in nature due to the sequential hydrolysis of TEOS in water, and the inner layer of the MSNs contain unhydrolyzed ethoxy groups are chemically less stable and thus, the inner layer can be selectively etched by hydrothermal treatment. In order to prove similar formation mechanism in the generated H-MSN, the same particles were prepared without hydrothermal treatments (H-MSN no HT) and TEM imaging and N_2 sorption measurements and thermogravimetric analysis (TGA) and differential scanning calorimetry (DSC) were carried out and the results were presented in Figure 27.

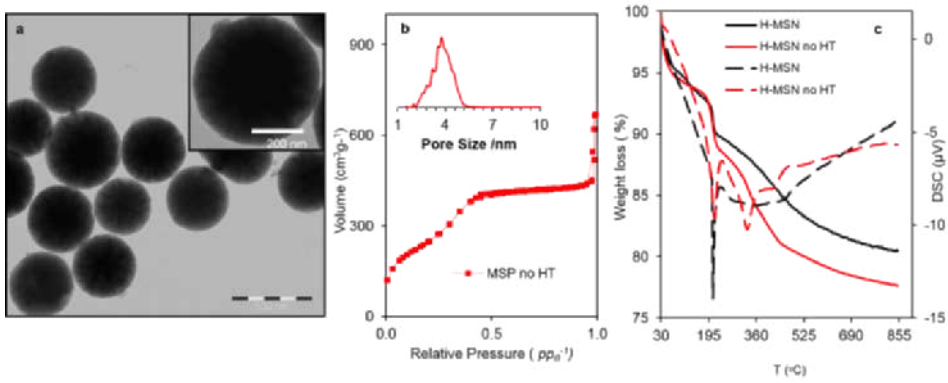

Figure 27. a) TEM images of MSNs prepared without hydrothermal treatment (MSN no HT) b) N2 sorption isotherm of H-MSN no HT together with pore size distribution c) TGA (continuous red and black lines) and DSC (red and black dash lines) curves of H-MSN and MSN no HT.

Solvent extraction was carried out to remove the SDA instead of calcination in order to preserve organic species in the silica network. As presented in Figure 27a, typical MSN structure without hollow voids was obtained and a typical H1 hysteresis loop (Figure 27b) was observed with a low pore volume value 0.7 cm^3 g^{-1}. The obtained characterization data for "H-MSN no HT" strongly support no hollow interior formation before the hydrothermal treatment. According to the obtained TGA and DSC curves in Figure 27c, a similar weight loss in the range of 170 and 250 °C for both H-MSN and "H-MSN no HT" samples were found with an accompanying exothermic peak at 212 °C in their DSC curves, which could be ascribed to the decomposition of aminopropyl groups from the co-condensed APTES silanes. Moreover, another notable exothermic peak at 325 °C is observed in the DSC curve of the sample before the hydrothermal treatment. It is difficult to determine the precise amount of organic species from the weight loss due to the overlapping of the dehydroxylation of silanols in the same temperature range. However, it is quite possible that the second exothermic peak resulted from the contribution of the unhydrolyzed ethoxy groups in the mesoporous silica network.[136]

The formation of ethoxy defects in the H-MSN network was also investigated by employing a similar MSN synthesis in the absence of APTES and TMB reagents. The negligible void formation in the MSNs was observed when the same synthesis was carried without APTES or TMB (MSN no APTES and MSN no TMB), as presented in the TEM images (Figure 28 a, b) Additionally, in the absence of APTES, chrysanthemum-like particles were formed with a wide pore size distribution ranging between 3 nm and 7 nm, as well as a significantly lower BET surface area (351 m^2 g^{-1}) was obtained (Figure 28c). On the other hand, in the absence of TMB, almost regular MSN morphology with 956 m^2g^{-1} BET surface area and with 4.9 nm average pore size value obtained (Figure 28 c).

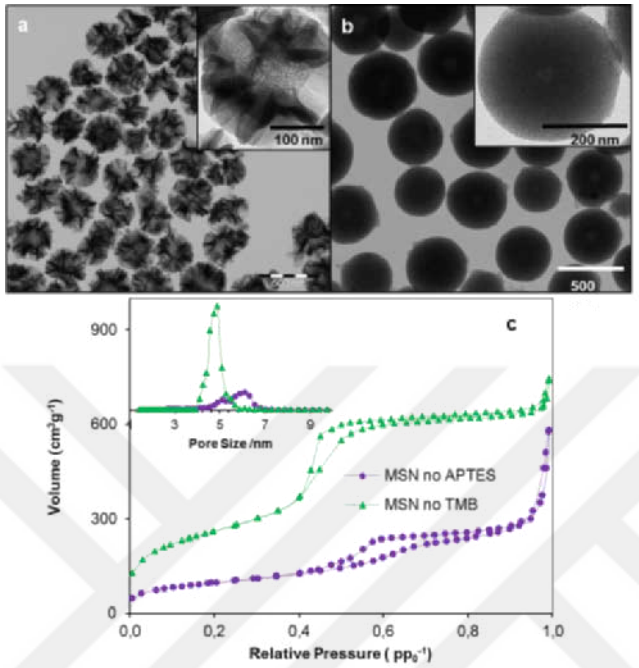

Figure 28. TEM images of (a) MSN synthesized without APTES (MSN no APTES), and (b) MSN synthesized without TMB (MSN no TMB) (PAPER V).

After investigating the generated MSNs under different synthesis conditions, the mechanism of H-MSN formation can be explained as a result of silica network formation with an accelerated speed in a controlled fashion during particle growth by the combination TMB and APTES reagents effect, which can, in turn, lead to less sufficient time for the hydrolysis of the silica source. Because TMB is a well-known reagent to accelerate the condensation of silica species due to the π-silanol interactions, while APTES can accelerate and strengthen the assembly between the template and silica source due to the increased hydrophobic packing by the aminopropyl group of APTES.[137] As a consequence, there are more and/or weaker defects preserved in the inner part of the particle during the particle growth, and a larger and more prominent hollow void was generated after the *in situ* hydrothermal treatment.

The obtained results from this part of the study provided information about synthesis of silica nanoparticles with controlled size, shape and structural characteristics in order to evaluate their impacts on biomedical applications.

5.2 Functionalization of Silica Nanoparticles

Surface chemistry of silica nanoparticles can be diversified by different methods, such as covalent conjugation of complexes, co-condensation, physical adsorption of polymers and surface grafting. In biomedical applications, surface modification of silica nanoparticles is usually utilized to increase their biocompatibility and reduce undesired interactions between the particles and their surroundings, tune the effective surface charge, enhance the colloidal stability of particles, provide affinity ligands for targeted delivery of cargo molecules and also to incorporate imaging modalities to silica nanoparticles. In this study, various type of surface modification strategies was also employed, including co-condensation and post-grafting of organosilanes with /without pre-reacting with fluorophores and physical adsorption of polymers and copolymers on silica surfaces.

As presented in the published papers and also the SUPPORTING PAPERs, the surface modification of silica nanoparticles is highly determinant for biobehavior of silica nanoparticles. When the surface functionalization of silica nanoparticles is carried out by using co-condensation approaches, in which the organosilanes are introduced already during the synthesis step, this leads to homogenous incorporation of the functional groups throughout the silica nanoparticles. This way of preparation is useful for the incorporation of fluorophores by pre-reacting it with organosilanes that are subsequently used in the co-condensation reaction and yielding inherently fluorescent silica nanoparticles as presented in PAPERs I and II.

In this study, the surface functionalization of silica nanoparticles was carried out to provide colloidal stability (PAPER I), to tune the effective surface charge (SUPPORTING PAPER II) on the particles, as capping agents for the pores (PAPER III, SUPPORTING PAPER I), to enhance the cellular uptake by cells (SUPPORTING PAPER II, VI) to incorporate imaging agents (PAPER III, IV, VI) and as anchor for affinity ligands (PAPER III and SUPPORTING PAPER IV, VI).

5.2.1 Surface Functionalization to Enhance the Colloidal Stability

In order to evaluate the colloidal stability of silica nanoparticles before and after surface modification, a model system with 100 nm sized non-porous silica nanoparticles was used with and without surface modification. The physical adsorption of prepared poly(ethylene imine) – poly(ethylene glycol) copolymers (mPEG-PEI copolymer) on SiNPs with two different grafting densities were carried out. The interaction mechanism between the prepared SiNP and copolymers were investigated by calorimetry and the effect of increased PEG grafting ratio on the attained colloidal stability of copolymer functionalized SiNP and its further implications on the biobehavior of SiNP were evaluated.

The study was started with the preparation of mPEG-PEI copolymers with low and high grafting densities of the mPEG unit. As presented in Figure 29, the grafting of mPEG (5000Da) portion on PEI (hyperbranched- 25000Da) was carried out by the linker hexamethylene diisocyanate (HMDI).

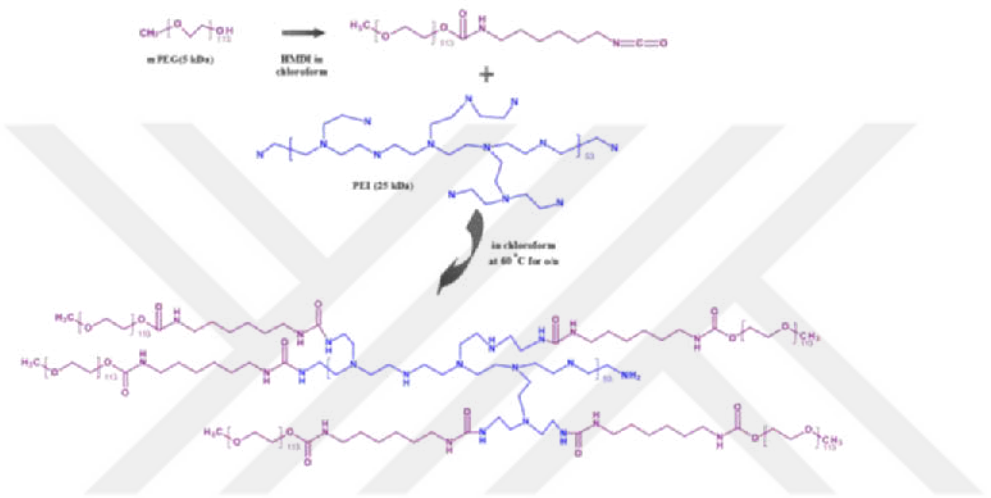

Figure 29. Synthesis of the mPEG-PEI copolymer (for $mPEG_{low}PEI$) (PAPER I).

The first grafting ratio was 6, abbreviated as "$mPEG_{low}$-PEI" and the second one was 50, abbreviated as "$mPEG_{high}$-PEI". The detailed description for the copolymer preparation and the success of preparation was discussed in PAPER I with the qualitative and quantitative structural confirmations. The success of reaction was claimed by FTIR analysis in which the peaks around 1660 cm^{-1} and 1540 cm^{-1} were referred to secondary amide I and II bands of PEI grafting on mPEG coupled HMDI, and also diminishing of the peak at wavelength 2275-2250 cm^{-1} was ascribed to the success of PEI grafting of mPEG-HMDI. In the same characterization part of copolymers, the accessible amine groups were quantified by titration method within the pH range 4 to 8 in order to predict the strength of possible electrostatic interaction between copolymers and SiNP. The accessible amine groups were calculated with the help of the plotted titration curves in Figure 30. The values 0.3, 0.15 and 0.07 molar equivalent (mequiv) amine groups for 1 g of PEI, $mPEG_{low}PEI$ and $mPEG_{high}PEI$ were estimated, respectively. The calculated values revealed that the accessibility of amine groups is decreasing with the increased grafting ratio between mPEG and PEI. This circumstance might also be predicted to result in less electrostatic interaction between $mPEG_{high}$-PEI and SiNP as compared to $mPEG_{low}$-PEI and PEI.

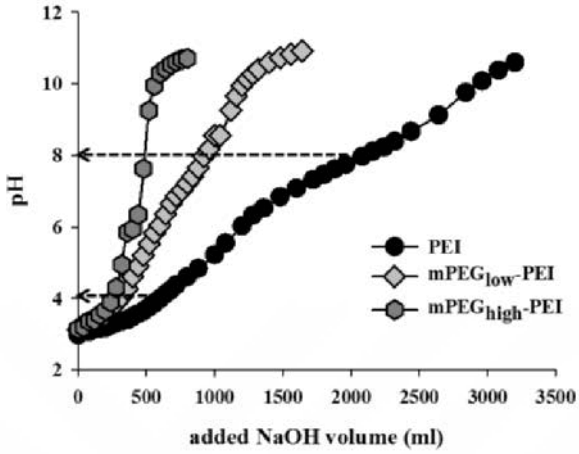

Figure 30. Plot of titration curves for PEI, mPEG$_{low}$PEI, mPEG$_{high}$PEI solutions (PAPER I).

Isothermal titration calorimetry (ITC) measurements were carried out after the characterization of copolymers, to monitor the interaction between copolymers and SiNP surfaces in detail. The same investigation was also performed for commercially available starting mPEG and PEI polymers in order to follow the change in the strength of interaction and the influence of mPEG grafting on the interaction with SiNP surfaces. The ITC measurements were carried out in HEPES buffer (pH 7.2, 25 mM) and the thermodynamic parameter, ΔH, was calculated from the absorbed or released heat due to the interactions between components. As presented in the following graph (Figure 31), ΔH vs. added polymer amounts, a clear change in the adsorption trend was observed with the altered mPEG grafting ratios.

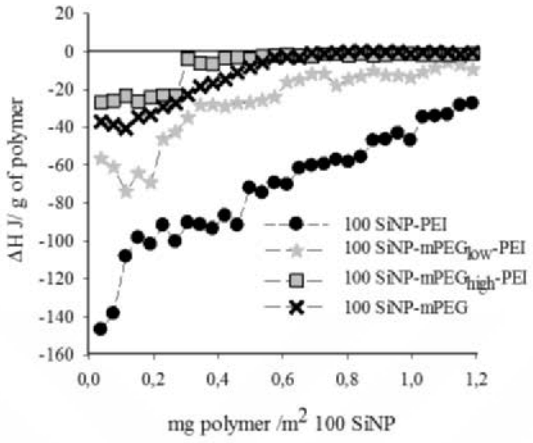

Figure 31. Enthalpy of interaction between mPEGlow-PEI, mPEGhigh-PEI copolymers, PEI, mPEG polymers and SiNP (PAPER I).

It is known that the silanol groups on the SiNP surface (IEP ~2) are negatively charged while the primary and secondary amine groups of PEI are positively charged in HEPES media. As presented in the plots, the strongest exothermic interaction is obtained between SiNP and commercial PEI due to the electrostatic interaction between them. The observed drop in the differential enthalpy from -140 to -97 J/g values were observed with 0.16 mg/m^2 PEI addition for 100 nm sized SiNP titration, after which the differential enthalpy value shows stepwise decrease to -27 J/g upon addition of 1.2 mg/m^2.Only exothermic enthalpy changes were observed, and differential enthalpy values have never reached a value of "0 J/g" which indicates that the saturation level of SiNP for the adsorption of PEI is higher than 1.2 mg/m^2. In the case of mPEG and SiNP interaction, weaker exothermic enthalpy changes were observed compared to PEI, which is attributed to binding of ethylene oxide residues to silanol groups of SiNP through hydrogen bonding.[138] The titration of SiNP with mPEG$_{low}$-PEI yields an exothermic interaction which decreases gradually up to the level of mPEG$_{low}$-PEI around 0.3 mg/m^2. Almost no changes were observed in differential enthalpy values after the addition exceeds the level of 0.7 mg/m^2. The titration processes of SiNP with mPEG$_{low}$-PEI never reached zero value, which indicates a continuous energy release during the interaction. This might be caused either by the reorganization of the mPEG$_{low}$-PEI copolymer on the SiNPs surfaces or multilayer formation. The interaction between mPEG$_{low}$-PEI and SiNP surfaces can be accepted as mostly supplied by the electrostatic interaction of amine groups on PEI and SiNP surface because the ITC plots reveal that PEI residues can increase the strength of interaction between SiNP and copolymers. In the adsorption process of

$mPEG_{high}$-PEI on SiNP surfaces, a sudden drop was observed at an addition of 0.3 mg/m^2, which yielded almost the same differential enthalpy value – 3.9 J/g for 100 nm SiNP, as was observed in the process of pure mPEG adsorption. The trend of the $mPEG_{high}$-PEI titration plot is similar to that of the mPEG titration plot, in which zero value was obtained for SiNP and mPEG interaction with a 0.5 mg/m^2 addition. This result implies that the binding of ethylene oxide residues of mPEG to silanol groups of SiNP become dominant with the increased mPEG grafting ratio on the expense of electrostatic interaction with amine groups of PEI.

We believe that the rational evaluation of interaction mechanisms between copolymers and SiNPs will aid to predict the colloidal stability of SiNP in suspensions. In order to examine the effect of grafting density of mPEG and copolymer concentration for dispersing and stabilizing the SiNP system, multiple light scattering (MLS) was employed to record transmission profiles for the prepared SiNP suspensions. The mean transmittances values for the SiNP suspension were obtained for the increased concentration of $mPEG_{low}$-PEI and mPEGhigh-PEI with respect to the SiNP amount ranging from 0.1 wt% to 7.5 wt % *(*Figure 32).

High mean transmittance values were observed for the 1 w% concentration level of $mPEG_{low}$-PEI and 1-5 wt% of $mPEG_{high}$-PEI after first 20 min of scanning, which is a possible result of "bridging flocculation", causes fast sedimentation of particles and leads to an increment in transmittance values. When the concentration of $mPEG_{low}$-PEI increased to 2.5 and 5 wt% lower mean transmittance profile was observed compared to naked SiNP suspension, which is possible stable flocculates with larger sizes than the particles. The 10-h colloidal stability profiles reveal that to attain sufficient dispersion stability for SiNP suspension, 7.5 wt% $mPEG_{low}$-PEI and $mPEG_{high}$-PEI addition is required. The ITC and MLS studies showed that with the increased PEG grafting ratio, mPEG parts of the copolymers are also taking part in the interaction of the copolymers and SiNPs surfaces, but still $mPEG_{high}$-PEI does not necessarily provide any superior efficacy for the stability of the nanoparticulate system as compared to the lower PEG grafting ratio in $mPEG_{low}$-PEI.

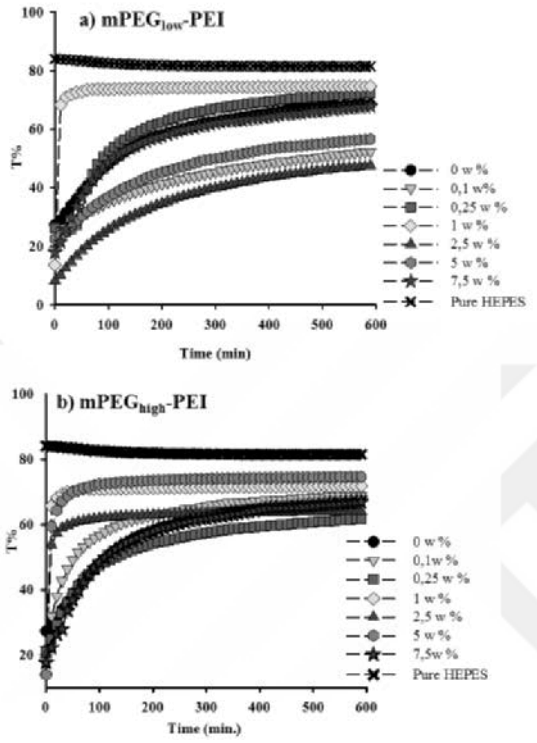

Figure 32. (a) The transmission of 100 nm SiNP with increased concentration of mPEGlow-PEI (from 0.1 to 7.5 wt%) and (b) mPEGhigh-PEI (from 0.1 to 7.5 wt%) addition (PAPER I).

After investigating the interaction mechanism between the in-house prepared mPEG-PEI copolymers and SiNPs surfaces, the effective colloidal stability type was also determined for the polymer coated and uncoated samples. In the experimentation part, the 100 SiNPs were coated with the amount of PEI, $mPEG_{low}PEI$, $mPEG_{high}PEI$ polymers which yielded the best colloidal stability. After coating process, 100 SiNPs were collected in order to remove excess polymers and re-dispersed in the suspension in which the ionic strength of the suspensions was increased stepwise with the addition of NaCl salt. The hydrodynamic size of SiNPs in the media without salt content (dh_0) and with the salt content (dh) was determined in order to predict existing colloidal stability mechanism in the suspension of particles. As presented in the plot (Figure 33), no significant difference was observed for the value (dh/dh_o) with the high NaCl addition (1 M) to the suspension of 100SiNP-$mPEG_{high}PEI$, which implies the effective stabilization type is steric stabilization. In the same plot dh/dh_o values for the 100 SiNP-PEI and 100 SiNP-$mPEG_{low}PEI$ suspensions increases significantly especially when the salt

content increased up to 1M. The observed increment in the values indicates the provided stabilization type by PEI and $mPEG_{low}PEI$ polymers is electrostatic stabilization.

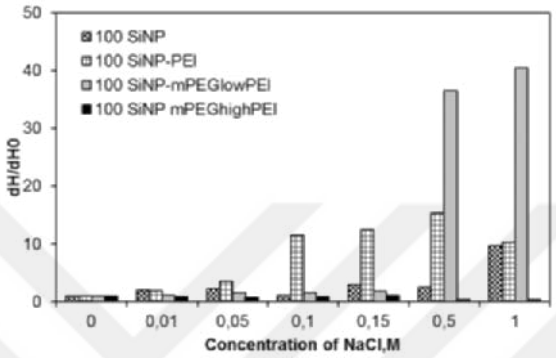

Figure 33. Hydrodynamic diameter change of 100 SiNPs with and without coatings of PEI, $mPEG_{low}$-PEI and $mPEG_{high}$-PEI as a function of increasing NaCl concentration in dispersing media.

As expected, the strongest aggregation with high ionic strength (1M) of the solvent was observed for the $mPEG_{low}$-PEI and PEI coated particles due to the shielding of charges, thus overcoming the clearly dominant electrostatic stabilization; whereas the particles with $mPEG_{high}$-PEI coatings were still colloidally stable up to 1 M NaCl. In the case of 0.15 M NaCl content, which is equivalent to the ionic strength of physiological media such as body fluids, both $mPEG_{low}$-PEI, and $mPEGl_{high}$-PEI coatings provided good colloidal dispersion. On the contrary, the difference in PEG grafting ratio did not cause any significant difference in flocculation behavior up to physiological salt concentrations level. In the literature, it has been reported that the PEG grafting density has a greater effect than the chain length on steric repulsion.[139] In our case, for the same chain lengths, and for both grafting densities of PEG ($mPEG_{low}$-PEI and $mPEG_{high}$-PEI), the thickness of the PEG layer is enough to balance the electrical double layer in the physiological salt concentration. This can be the result of the existing adsorption mechanism, as when the PEG grafting density of the copolymer is increased, the PEG part of the copolymer also starts to take part in the adsorption process, in which case this portion of PEG does not contribute to the steric stabilization as polymer chains extended from the particle surface into solution. Thus, the chain length of 5 kDa PEG provides a sufficient PEG layer thickness already at the low grafting density for the steric stabilization in the employed nanoparticulate system.

The obtained results from this part of the thesis served rational basis to design colloidally stable, well-dispersed nanoparticulate systems with PEG-PEI copolymers surface modifications for biomedical-related applications.

5.2.2 Surface Modification for Tuning the Net Effective Surface Charge

The net effective surface charge on non-porous silica nanoparticles (SiNP) and mesoporous silica nanoparticles (MSN) were altered. Co-condensation of organosilane (3-Aminopropyl) triethoxysilane (APTES) with the silica source in the synthesis step (SUPPORTING PAPER III), post-synthesis grafting of functional groups (PAPER IV) and physical adsorption of polymers on the readymade silica particles (PAPER I and IV) were the employed strategies for surface modification of silica nanoparticles.

In SUPPORTING PAPER III, altering the net surface charge of two differently sized SiNPs (small non-porous (SS), big non-porous (SB) silica nanoparticles) and MSNs (small mesoporous (MS), big mesoporous (MB) silica nanoparticles) were carried out with the incorporation APTES in the synthesis solution by the co-condensation method. For the net surface charge altering on SiNPs, the incorporated APTES amounts were increased relative to the amount of TEOS (2.5 mol %, 5 mol %,10 mol %) in the different batches, and net surface charge of particles was varied from negative (-) to positive (+) values. In the same manner as SiNPs, the net surface charge of MSNs was altered by increasing the added APTES amount relative to TEOS (with respect to 4 mol % and 10 mol % of TEOS). In Figure 34, ζ-Potential values and the estimated w% amount of APTES for silica nanoparticles are presented.

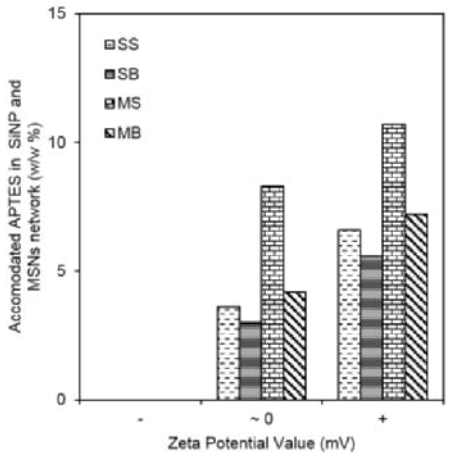

Figure 34. ζ-potential values of prepared SiNPs and MSNs in HEPES buffer solution vs. estimated w% APTES amount in co-condensed SiNPs.

According to estimated data, the incorporated APTES amount was slightly higher for mesoporous particles compared to non-porous particles to provide net surface charge tuning on the particles from net negative to net positive values. This case is most probably due to more embedding of the functional groups (aminosilanes) in the mesoporous silica network compared to non-porous silica network, since the aminosilane groups also may take part in structure directing during the synthesis whereas for the non-porous structure it takes part in the condensation reaction.

The post-grafting surface functionalization method was employed in the unpublished investigations of the thesis in order to alter the net surface charge of the SiNPs at physiological pH 7.2. In this way of preparation, APTES was post-grafted on differently sized SiNPs (100 nm and 300 nm, labelled as 100 SiNPs, 300 SiNPs respectively) by increasing the added APTES amount for each prepared batch relative to the specific surface are of SiNPs (250, 100, 50, 25, 10, 5, 1, μmol/m^2). With the obtained results, we can claim that the concentration and the distribution of organic moieties provided by the post-grafting method are constrained by the number of surface silanol groups and their accessibility.[62, 140] In the post-grafting process, the silanols on the surface of SiNPs anchor the organosilanes so the difference in the number of silanol groups lead to a difference in the yield of post-grafting. According to the obtained ζ-potential results, the values were -35 and -55 mV in HEPES buffer solution for 100 SiNPs and 300 SiNPs, in order which can be accepted as the implication of difference in the number of existing silanol groups on the particles. When the efficiency of the post-grafting process was compared, the difference in the existing silanol groups of 300 SiNPs and 100 SiNPs on the surface of SiNPs can be noticed. While the yield of post-grafting functionalization reaches the value 95 % for the grafting of 100 SiNPs with the highest starting concentration, it couldn't go higher than 10 % for the 300 SiNPs in the same case (Figure 35). With the help of the presented plots, the existing accessible silanols groups for 100 SiNPs can be estimated as being roughly 10-fold higher than 300 SiNPs.

The case is more complicated for the mesoporous structure compared to non-porous structures. The literature studies reveal that the space of the mesopores does create a different situation compared to the functionalization of non-porous surfaces.[141] The post-synthesis grafting on mesoporous silica nanoparticles yields inhomogeneous surface coverage due to the accumulation of the functional groups near the entries of mesopores and exterior surfaces. So the differences in the surface structure of silica particles also have an influence on the yield of accommodated functional groups by post-grafting, in addition to accessibility of silanol groups.[62]

According to the obtained results, both co-condensation and post-grafting methods were successfully used to alter net surface charges and tune the surface concentration of the organosilanes, which can be subsequently employed as

anchoring points for further functionalization by using e.g. standard amino-carboxylic acid-based chemistry.

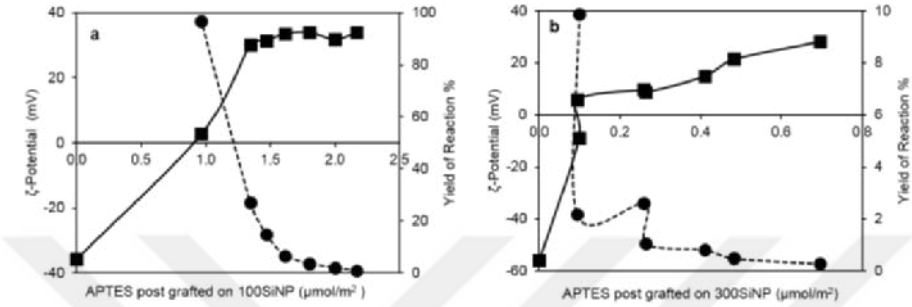

Figure 35. Yield of APTES post grafting reaction for a) 100 and b) 300 SiNPs preparations together with the estimated surface grafting by APTES and measured ζ-Potential values.

The polymeric surface modification via hyperbranching surface polymerization and physical adsorption of polymers (chitosan and polyethyleneimine (PEI)) on rod-like mesoporous silica nanoparticles (NR-MSP) also aided to tune the net surface charge of the silica nanoparticles (PAPER II and III). Moreover, the polyethyleneimine grafted silica samples were functionalized via either succinylation to yield negatively charged succinic acid groups or capping of the primary amines with uncharged acetyl groups as explained in the schematic presentation (Figure 36) below from PAPER II.

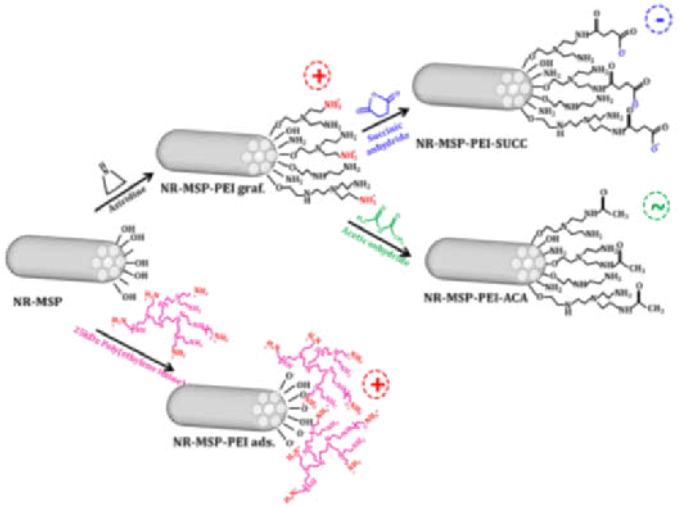

Figure 36. Schematic illustration of polymeric surface modification on NR-MSPs.

The accumulated PEI amount on the NR-MSP samples after the hyperbranched surface polymerization approach was determined as 10 wt% by TGA and the changes in the ζ-potential values are given in Table 2 below.

In this part of the study, ζ-potential values of the silica nanoparticles (Table 2) were examined in HEPES buffer (25mM @ pH 7.2) which is relevant to physiological pH value in biomedical applications.

Table 2. ζ-potential values of differently functionalized NR-MSPs in HEPES buffer solution.

SAMPLES	ζ- Potential [mV]
NR-MSP	-16
NR-MSP-PEI ads.	25
NR-MSP-PEI graf.	23
NR-MSP-PEI-ACA	-12
NR-MSP-PEI-SUCC	-29

In the case of physical adsorption of polymers on silica nanoparticles, $mPEG_{low}$-PEI, $mPEG_{high}$ PEI copolymers, PEI, and chitosan adsorption were carried out in order to yield net positive surface charge values on the particles, which also provided better redispersibility for the particles in the suspension.

In the unpublished data related to PAPER I, the copolymer concentration was increased stepwise and the yielded ζ-potential values were determined for 100 SiNPs. In the experimentation part the 100 SiNPs were coated with the increasing amount of $mPEG_{low}$PEI copolymer (0.1, 0.25, 1, 2.5, 5, 7.5 wt%) and the ζ-potential values for each coating amount was determined in order to find out required amount of $mPEG_{low}$PEI copolymer on SiNPs to yield high enough ζ-potential value for the colloidal stability. The influence of PEG amount on the copolymer was also further investigated by coating the 100 SiNPs with the 5 wt% starting amount $mPEG_{low}$PEI, $mPEG_{high}$PEI and PEI respect to the 100 SiNP mass.

Figure 37 reveals that a ζ-potential value of 100 SiNPs does not change significantly after the copolymer concentration on the 100 SiNP reaches the saturation value which is approximately 0.25 mg/m^2 (according to TG analysis results) and matching also with the obtained ITC results. As it is expected, in Figure 37 with the increased PEG content on the copolymers, tuning of the net surface charge on the 100 SiNP is not possible due to the uncharged PEG component which

has occupied the amine groups of PEI polymer providing the positive amine groups in HEPES buffer (25mM pH7.2)

As a brief summary of this part, co-condensation and post-grafting of 3-aminopropyl triethoxysilane (APTES) and physical adsorption of the differently charged polymers and copolymers on the silica nanoparticles have been successfully utilized to yield different ζ-potential values. All the methods have different simplicities and complexness, so in order to make the surface modification serve the aimed application, the functionalization approach should be decided carefully.

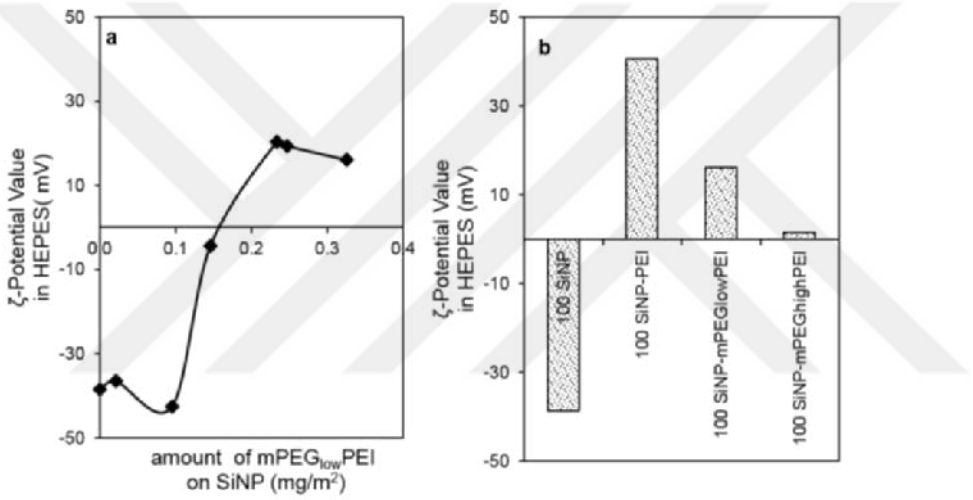

Figure 37. Influence of PEG portion of the post polymeric surface modifications on ζ-potential value of SiNPs a) the amount of mPEG$_{low}$PEI coating on 100 SiNPs b) change of ζ-potential values for different surface coating of 100 SiNPs.

5.3 Modular Design of Silica Nanoparticles for Diagnosis and Therapy Applications

Silica nanoparticles can be designed as multi-functional materials with the help of different surface modifications. In this study imaging, controlled drug release and cell-specific targeting capabilities were tried to be embedded in the silica nanoparticles, because these are important properties in order to make silica particles better functioning in biomedical applications. Traceable silica nanoparticles are required in the biological/physiological environment for imaging and/or diagnostic applications, in addition, controlling the release of therapeutic agents and delivering them to the precise address for combating disease states is needed in therapeutic applications in order to provide higher efficiency for curing the disease.

5.3.1 Enhancing the Drug-Loading Capacity of Silica Nanoparticles by Altering Structure

In the unpublished experiments of the thesis, the drug loading capacity of three non-functionalized mesoporous silica nanoparticles, spherical mesoporous silica nanoparticles (from Table 1- 10D the rod–shaped mesoporous silica nanoparticles (NR-MSPs) and hollow-structured mesoporous silica nanoparticles (H-MSN), were investigated based on their structural differences. The deposition of model drug furosemide (FUR), a class IV of the Biopharmaceuticals Classification System (BCS), was carried out by overnight mechanical mixing of silica nanoparticles with the drug in cyclohexane. First, the loading degree of FUR to 10D-MSN, NR-MSP, and H-MSN samples was investigated by depositing the different amount of furosemide (10, 25, 50,100 and 125 w/w% of silica mesoporous silica nanoparticles) in cyclohexane. Subsequently, the drug loading amounts were measured by UV-VIS spectrophotometry after the overnight liberation of FUR in ethanol solvent.

Different adsorption profiles were obtained for MSNs as presented in Figure *38* and the highest degree of loading was obtained for H-MSN (~100 w/w%) with the advantage of existing hollow space in H-MSN particles and expanded average pore sizes (about 5 nm, Figure 26 b presented in section 5.1.) The similar profile was also obtained for NR-MSP, which resulted in 88 w/w% loading degree, which is possibly due to the large pore sizes (about 11.3 nm, PAPER III), and might lead packing of high amount of drug molecules into the pores. On the other hand, 25 w/w% loading was obtained for 10D-MSNs samples, which thus has the lowest loading degree among the investigated MSNs.

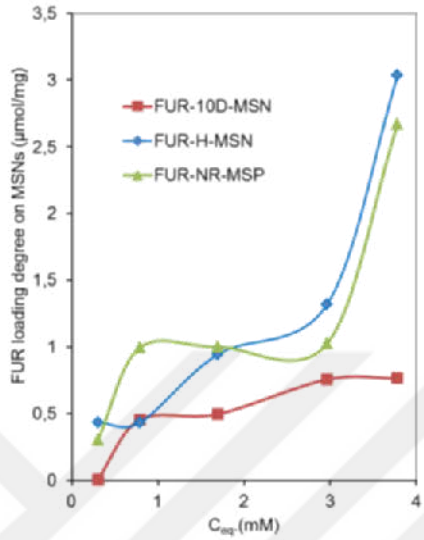

Figure 38. Adsorption isotherms of Furosemide (FUR) to 10D-MSN, H-MSN and NR-MSP plotted as loaded FUR amount (µmol) to mg of particles.

DSC analysis was carried out in order to investigate the thermal profile of bulk FUR and loaded FUR onto MSNs. In Figure 39, minor peaks were observed at around 137 °C which is probably caused by the glass transition of existing amorphous drug on the particles. Clear exothermic peak at 221.4 °C which is associated with the recrystallization of super cooled melt of the drug was observed for bulk FUR and loaded FUR on H-MSN and NR-MSP samples. Whereas, only a broad peak was observed for the FUR loaded 10D-MSN sample. The difference in the profile of recrystallization peak can be ascribed as the absence of crystal FUR structure on 10D-MSN due to retained drug molecules in the confined pore spaces. The existing the hollow space (of H-MSN) and the outer surface of the both type particles (H-MSN and NR-MSN) with bigger pores sizes provide enough space for the recrystallization of loaded drug on the particles. In the range of 250-290 °C endothermic peaks are observed for all the samples which can be ascribed as melting and decomposition of the drug.

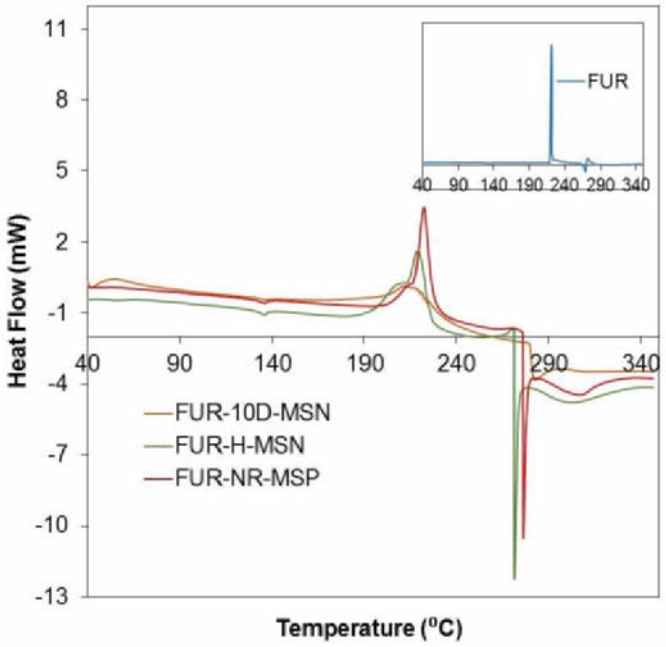

*Figure 39. DSC curve of FUR, FUR loaded 10D-MSN, H-MSN, and NR-MSP. Heat rate=10 °C/min, gas purge N2 (**Exo UP**).*

A clear difference is observed in the loading degrees of FUR on the MSNs due to the structural differences. In addition, high degree of FUR loading on both H-MSN and NR-MSP samples leads to formation of crystalline FUR on the samples. It is well known and tested with several different types of drugs in the literature; the crystalline drug formation affects the dissolution rate of the drug since the solubility is limited by high crystal energy.[142] From a drug delivery point of view, high loading degree could be quite attractive but it is critical to be aware of the possible crystalline formation within MSNs with high loading degrees which will, in turn, affect the dissolution rate of drug.

5.3.2 Enhancing the Imaging and Cell Labeling Capability of Silica Nanoparticles

Imaging capability for silica nanoparticles can be provided by incorporating the imaging agents either directly into the synthesis solution as *in situ* treatment or after making the particles ready as post-synthesis treatment. In this study, both strategies were employed to make the silica nanoparticles traceable with fluorescence based analysis (confocal microscopy, fluorescence-activated cell sorting) and magnetic resonance imaging (MRI).

In PAPER II and IV, silica nanoparticles were labeled by pre-conjugation of the fluorescent dye with aminosilanes, which were subsequently incorporated in the synthesis step *via* co-condensation. In SUPPORTING PAPER V the conjugation of fluorophores was carried out via post-synthesis conjugation method in order to use them as FRET-reporter particles to follow the intracellular cleavage of the conjugated molecules. In addition, in PAPER VI, paramagnetic gadolinium centers were incorporated into silica nanoparticles matrix *via* post synthesis and *in situ* synthesis doping protocols, as described in PAPER VI, to make them serve as contrast agents for magnetic resonance imaging.

Fluorescent dyes are the most commonly employed molecules to image silica particles by using common biological imaging techniques. However, it is well-known that organic fluorophores suffer from certain drawbacks that may limit or, at least, complicate the quantitative data that can be acquired based on the fluorescence-based analysis. In the literature, the covalent conjugation of fluorophores into silica matrix has been mentioned to decrease the leakage of the dye from the matrix which is important in the quantification based approaches.[143] In PAPER IV, two of the most commonly used fluorescent tags : fluorescein isothiocyanate (FITC) which is claimed as pH-sensitive and tetramethylrhodamine isothiocyanate (TRITC), pH-insensitive, were incorporated into MSNs and the parameters that influence the fluorescence properties of labelled particles such as surrounding (biologically relevant) media, particle concentration and especially, surface functionalization, was considered toward aiming for quantification in the fluorescence-based analyses.

First, the characterization of the MSNs was carried out to find the incorporated amount of fluorophores in unmodified particles by UV-Vis method and the calculated value was approximately 1 wt% in each MSN preparation.

Afterwards, the influence of surrounding media on the fluorescence properties of the produced fluorescent particles (without additional surface functionalization) was investigated by redispersing them in buffer solutions of cellular relevance at the concentration 0.5 mg/ml MSN, in MES buffer (pH 5 corresponding to endo/lysosomal pH), HEPES buffer (pH 7.2 corresponding to cytoplasmic pH) as well as serum-supplemented DMEM cell media.

Evidently, significantly lower fluorescent intensity value was observed for the FITC-conjugated MSNs (F-MSN1) at acidic pH than neutral, as expected; while no difference in fluorescence behavior was found for the TRITC-conjugated MSNs (T-MSN1) in both acidic and neutral pH buffer solutions (Figure 40).

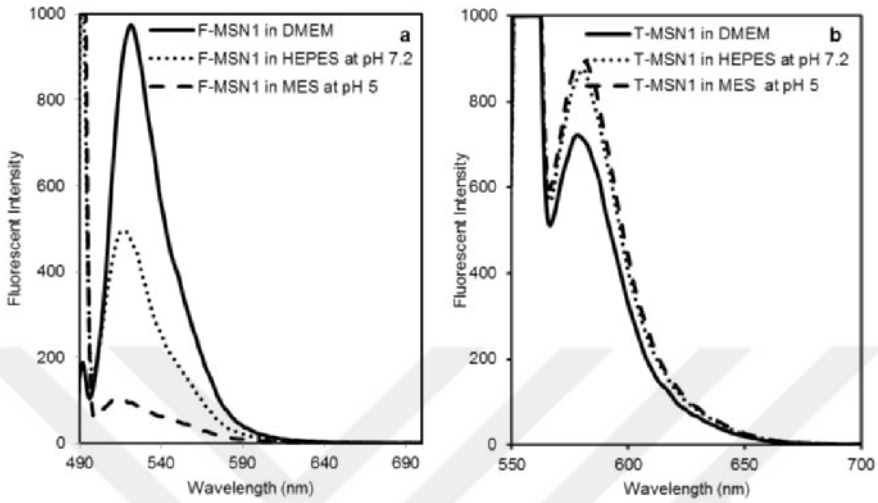

Figure 40. Fluorescence spectra of F-MSN1 and T-MSN1 at neutral and weakly acidic pH buffer solutions as well as in cell media (DMEM) (ex = 490 nm for FITC- and 555 nm for TRITC-conjugated MSNs) (PAPER IV).

Accordingly, the observation was in agreement with the well-established behavior of the free dyes. On the other hand, stronger fluorescent intensity value was observed for F-MSN1 compared to the fluorescent intensity of T-MSN1 in DMEM. This could be due to the complexity of composition of the cell media and the exact reason may be thus hard to clarify. For instance, it could be due to the exhibited auto fluorescence by the biologicals to some degree and the serum content in the media may also adsorb to the MSNs which induce either enhancement or quenching of the observed fluorescence.[144] With considering the results in DMEM cell media it is important to note that since MSNs are incubated in cell media for *in vitro* studies, quantification attempts based on measurements made under less-biological conditions, may not apply when extrapolated to biological conditions and still the pH-dependent effect was, however, in this case, clear-cut and in accordance with the expected behaviors of the free dyes.

The fluorescence spectra of unmodified F-MSN1 are presented in Figure 41 at different pH. The pH-dependent behavior of F-MSN1 is in agreement with the free dye behavior. The unmodified particle suspensions can be used as "standard curve" to probe the local pH that fluorescein molecules are experiencing on the corresponding surface modified MSNs. In order to define the "local pH" that the fluorescein molecules are experiencing due to the surface modification on MSNs, the fluorescence intensity at the maximum peak was plotted against pH (Figure 41*c)* for the unmodified F-MSN. In that case, the maximum peak intensity value of PEI

adsorbed F-MSN1 (PEI-F-MSN1) in water matched with the intensity value of F-MSN1 at pH 6 (Figure 41c). In this sense, pH 6 can be ascribed as the experienced "local pH" for the fluorescein molecules in PEI-F-MSN1.

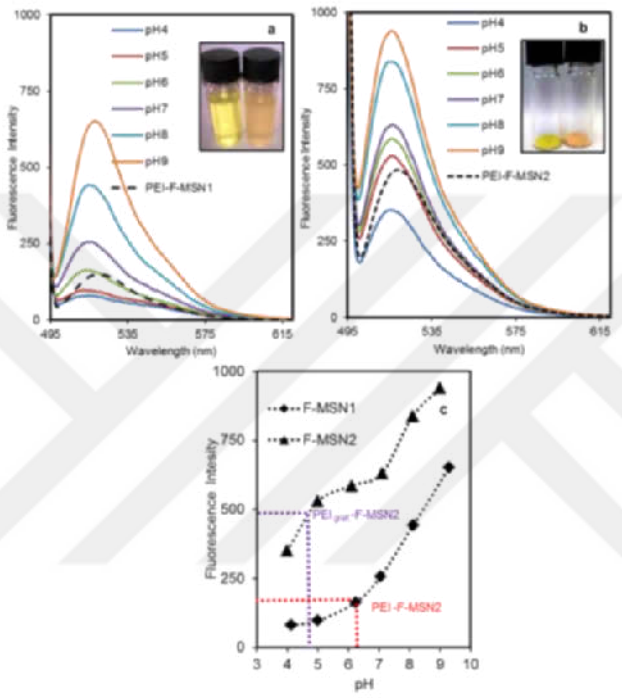

Figure 41. Dependence of fluorescence intensity of FITC-conjugated MSN as a function of pH. a) F-MSN1 fluorescence intensity variability with solvent pH. Coating with PEI (10 wt%) via electrostatic adsorption results in the same emission spectra regardless of solvent pH, Inset: F-MSN1s (left) vs PEI$_{ads.}$-F-MSN1s (right) in HEPES buffer. b) Same as previous repeated forMSN2 and PEI$_{graf.}$-MSN2, resulting in an enhanced local pH drop due to PEI residing also inside the mesopores. Inset: dry FITC-conjugated MSN2s (left) vs PEI$_{graf.}$-MSN2s (right) c) Determination of "local pH" experienced by the fluorescein molecules on PEI-modified F-MSN1 and F-MSN2.

With the same way of exploring the local pH for the fluorescein molecules in PEI$_{graf}$-F-MSN2 was estimated to be slightly below 5 (Figure 41c). In this sample preparation, F-MSN2 samples were prepared by a different MSN synthesis protocol than F-MSN1 as described in PAPER IV. The slightly different protocol was employed in order to provide amine groups on MSNs to be able to further graft the surface of particles with PEI. The obtained difference in the local pH of PEI$_{graf}$-F-MSN2 sample could very well be due to the fact that in the surface hyperbranching

process, PEI is grown both on the inner (pore wall) and outer (particle) surfaces; whereas by adsorption of large molecular (25 kDa) weight PEI, the location of the PEI polymer would be predominantly on the outer particle surface. Thus, being present both on the outside particle surface and inner pore walls, the local "proton trap" effect of PEI would also be more predominant inside the pores in the case of grafted PEI, which is reflected in the lower local pH (i.e. the higher local concentration of protons) observed. The accompanied red shift observed for both the PEI-MSN peaks (Figure 41 a, b) could be due to the induced local polarity change, brought upon by the local abundance of protons, similar to that of positive solvatochromism rather than a pH-induced effect.

To further confirm that no influence of the pH of the surrounding medium on the PEI-modified MSNs is taking place, the fluorescence spectra was recorded for PEI-F-MSN1 under the same conditions as presented in Figure 40. As can be seen also here *(*Figure 42*),* in the presence of a PEI coating, the surrounding pH has no effect on fluorescence intensity. Even the influence of cell media (DMEM) observed for the particles without a PEI coating above, is overridden by the strong influence of a PEI-coating.

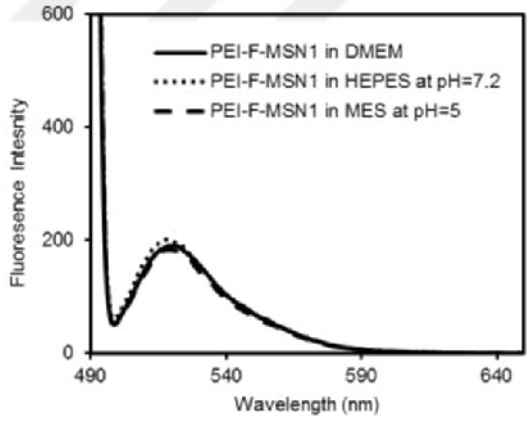

Figure 42. Fluorescence spectra of PEI-coated F-MSN1 at neutral and weakly acidic pH buffer solutions as well as in cell media (DMEM).

It is very well known that the self-quenching caused by the fluorophores in close proximity could be one of the problems for alteration in fluorescence. [145, 146] Therefore, it is ideal to have design of MSNs which own the fluorophores distributed throughout the MSN network to overcome such a problem. But it is still possible to have similar self- quenching problem if the particle concentration is high enough to be in contact each other. In this study, the amount of incorporated fluorophore

was fixed (~1 wt%) in MSNs and it is important to investigate the effect of particle concentration on fluorescence intensity especially for the applications in which the majority of fluorescent particles are used for the quantification. The fluorescence intensity values of F-MSN1, PEI-F-MSN1, T-MSN1and PEI-T-MSN1s were recorded as a function of particle concentration to investigate whether particle concentration could have a profound effect on the fluorescence. Clearly, a significant effect of MSN concentration on fluorescence intensity is observed for all particles, where the concentration dependence furthermore varies also depending on the surrounding pH for fluorescein-labeled MSNs (Figure 43). On the contrary, for the rhodamine-labeled particles (T-MSN1 and PEI-T-MSN1) a pH-independent behavior is obvious, whereas a similar particle-concentration-dependent behavior also exists.

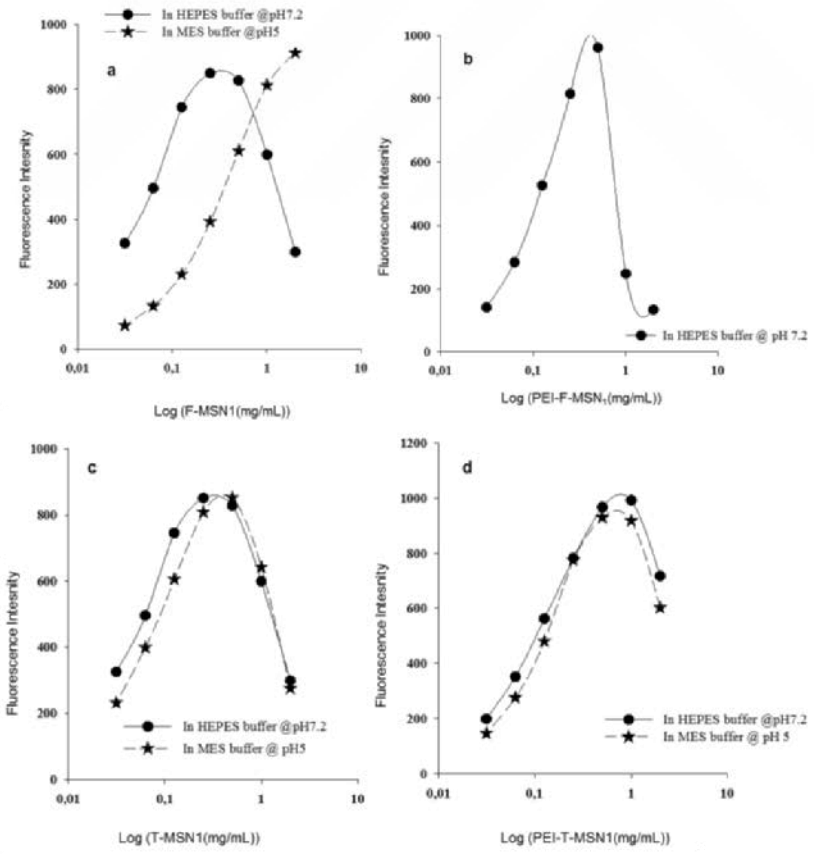

Figure 43. *Fluorescence intensity as a function of MSN concentration for (a) F-MSN1s (b) PEI$_{ads}$-F-MSN1s (c) T-MSN1s (d) PEI$_{ads}$T-MSN1s (PAPER IV).*

All in all, for utilizing silica nanoparticles as tracking agents by fluorescence-based analysis, the most critical points can be mentioned as the environment that the fluorophore is exposed (especially for pH-sensitive fluorophores) to and also the concentration of fluorophore (for both pH sensitive and insensitive fluorophores) in the analysis environment. Controlling the mentioned points aid the quantification of fluorophore-labeled silica nanoparticles in fluorescence-based analysis.

The structural properties and preparation routes of silica nanoparticles have also effects on the rational enhancement of the potential imaging capabilities. Therefore, in PAPER VI, the structural properties and preparation routes of the mesoporous silica nanoparticles (MSN) based contrast agents were modulated in order to enhance the T1-weighted MR imaging capability. In the present case, MSNs into which gadolinium (Gd (III)) was incorporated/introduced *via* different routes were synthesized, while the structural features were modulated *via* different pre- and post-synthesis approaches. With the investigated designs, we aimed to preserve the mesoporous channels free to act as drug reservoirs for future therapeutic prospects, while providing contrast enhancement for MR imaging.

In this study, the MSN samples were prepared by different routes, as presented in Figure 44 and the characterizations were carried out with different methods in order to see the variations in relaxivity values of the differently prepared MSN-based contrast agents.

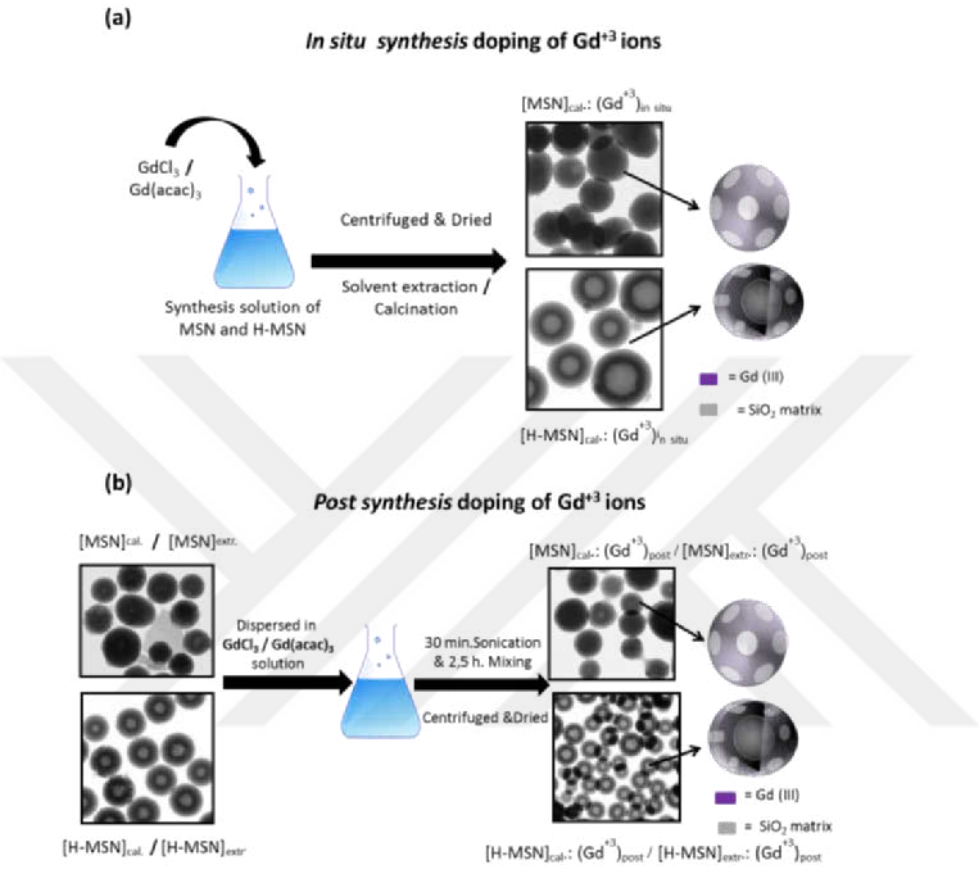

Figure 44. Incorporation of gadolinium ions into MSN matrices by (a) in situ synthesis and (b) post-synthesis methods (PAPER VI).

The changes in the dispersibility and net surface charge were determined by measuring the hydrodynamic diameter and zeta potential values of the samples in suspension form. The samples were dispersed in HEPES buffer (to a concentration of 0.5 mg/mL) for the measurements, and poly(ethylene glycol)-poly(ethylene imine) (PEG-PEI) block copolymer produced in PAPER I, which was also employed in our *in vitro* evaluations in order to enhance the cellular uptake, [147] was further used here as dispersing agent in order to obtain better dispersibility of the MSN-based contrast agents under physiological/biological conditions. The obtained values for the measurements are presented in Table 3 and the hydrodynamic diameters and the zeta potential values of the produced samples are varying between 300-700 nm and highly negative (approx. -41 mV) and positive values (approx. +17 mV) due to the different gadolinium incorporation routes as well as an abundance of amine

groups on the MSNs, provided by the added aminosilane reagent in the synthesis process.

Table 3. Hydrodynamic diameter and zeta potential values of prepared MSNs in HEPES buffer (pH 7.2, 25mM) as 0.5 mg/mL particle suspensions (Zeta potential measurements were carried out before the dispersion agent, a PEG-PEI copolymer addition)

SAMPLE	Hydrodynamic size [nm]	PDI	Zeta Potential [mV]
$[MSN]_{cal.}$	313	0.27	-39
$[MSN]_{extr.}$	530	0.32	17
$[H\text{-}MSN]_{cal.}$	686	0.26	-32
$[H\text{-}MSN]_{extr.}$	650	0.43	4
$[MSN]_{cal.}$: $(Gd(Cl)_3)_{in\ situ}$	417	0.65	-31
$[MSN]_{cal.}$: $(Gd(aca)_3)_{in\ situ}$	329	0.3	-41
$[H\text{-}MSN]_{cal.}$: $(Gd(Cl)_3)_{in\ situ}$	775	0.53	-28
$[H\text{-}MSN]_{cal.}$: $(Gd(aca)_3)_{in\ situ}$	574	0.42	-32
$[MSN]_{cal.}$: $(Gd(Cl)_3)_{post}$	243	0.1	-14
$[MSN]_{extr.}$: $(Gd(Cl)_3)_{post}$	381	0.38	16
$[MSN]_{cal.}$: $(Gd(aca)_3)_{post}$	348	0.34	-32
$[MSN]_{extr.}$: $(Gd(aca)_3)_{post}$	283	0.12	16
$[H\text{-}MSN]_{cal.}$: $(Gd(Cl)_3)_{post}$	671	0.29	-23
$[H\text{-}MSN]_{extr.}$: $(Gd(Cl)_3)_{post}$	348	0.3	4
$[H\text{-}MSN]_{cal.}$: $(Gd(aca)_3)_{post}$	650	0.35	-25
$[H\text{-}MSN]_{extr.}$: $(Gd(aca)_3)_{post}$	730	0.34	-2

The possible defects in the mesoscopic ordering of MSNs that might be caused during the post-synthesis doping process of gadolinium into MSN and H-MSN matrices were investigated by SAXRD analysis. Distortion of the mesoscopic order of the MSNs might affect the water accessibility to gadolinium centers in the matrices negatively in the application. The diffraction patterns are presented in view of the effect of the SDA removing protocols (Figure 45) and the employed post-synthesis doping protocols utilizing both gadolinium sources ($GdCl_3$, $Gd(acac)_3$) and their effect on the mesoscopic order of MSN and H-MSN. As shown in the diffractograms (Figure 45), the calcination process for SDA removal provides better rigidity for both MSN matrices. The partial distortion of the pore ordering was observed for the matrices treated by the solvent extraction process, which is most probably due to the accelerated dissolution rate of silica caused by the existing amine

groups and, furthermore, the lower silica condensation degree, when exposed to aqueous media.

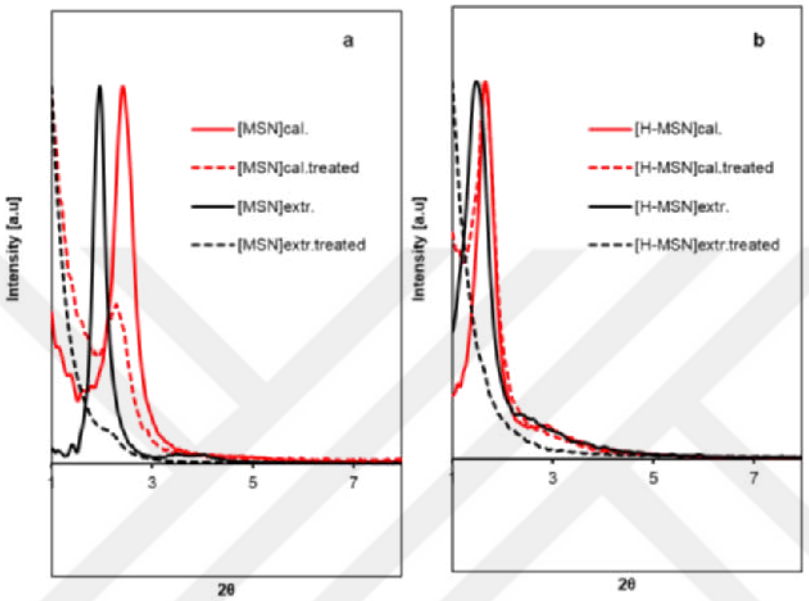

Figure 45. SAXRD diffraction patterns of (a) calcined /solvent extracted MSN powders ([MSN]$_{cal}$,[MSN]$_{extr}$), and after treating the same samples under the same condition of post-synthesis doping protocol ([MSN]$_{cal.treated}$, [MSN]$_{extr.treated}$) (b) calcined /solvent extracted H-MSN powders ([H-MSN]$_{cal}$,[H-MSN]$_{extr}$), and after treating the same samples under the same condition of post-synthesis doping protocol ([H-MSN]$_{cal.treated}$, [H-MSN]$_{extr.treated}$) (PAPER VI).

The quantitative determination of the amount of doped gadolinium in MSN matrices was carried out by ICP-AES after complete dissolution of the samples in HF. The results are given in Table 4 below, from which can be concluded that the highest incorporation of gadolinium was obtained via post-synthesis doping of [MSN]$_{extr.}$ and [H-MSN]$_{extr.}$ matrices with $Gd(Cl)_3$ (named as [MSN]$_{extr.}$: $(Gd(Cl)_3)_{post}$ and [H-MSN]$_{extr.}$: $(Gd(Cl)_3)_{post}$).

Table 4. Longitudinal relaxivity (r_1) and transverse relaxivity (r_2) data of prepared MSN-based contrast agents.

SAMPLES	Gd^{+3} amount in MSNs/ µmol mg^{-1}	r_1 / $mM^{-1}s^{-1}$	r_2 / $mM^{-1}s^{-1}$	r_2/r_1
$[MSN]_{cal.}$:$(Gd(Cl)_3)_{in\ situ}$	0.7	0.3	1.5	5
$[H\text{-}MSN]_{cal.}$:$(Gd(Cl)_3)_{in\ situ}$	0.11	6.7	10.2	1.5
$[MSN]_{cal.}$:$(Gd(acac)_3)_{in\ situ}$	0.69	0.5	2.6	5.2
$[H\text{-}MSN]_{cal.}$:$(Gd(acac)_3)_{in\ situ}$	0.6	13.1	28.4	2.2
$[MSN]_{cal.}$: $(Gd(Cl)3)_{post}$	0.81	7.3	12.1	1.6
$[MSN]_{extr.}$: $(Gd(Cl)3)_{post}$	0.92	1.9	5.6	2.9
$[H\text{-}MSN]_{calc.}$:$(Gd(Cl)_3)_{post}$	0.24	7.7	12.8	1.7
$[H\text{-}MSN]_{extr.}$:$(Gd(Cl)_3)_{post}$	0.02	1.0	3.3	3.3
$[MSN]_{cal.}$: $(Gd(acac)_3)_{post}$	0.52	12.1	17.7	1.5
$[MSN]_{extr.}$: $(Gd(acac)_3)_{post}$	0.45	2.4	7.5	3.1
$[H\text{-}MSN]_{calc.}$:$(Gd(acac)_3)_{post}$	0.53	13.1	21.1	1.6
$[H\text{-}MSN]_{extr.}$:$(Gd(acac)_3)_{post}$	0.5	5.9	13.1	2.2

The longitudinal proton relaxation times (T_1) and transverse relaxation times (T_2) of the MSN suspensions at 37◦C were determined for the samples at different concentrations (in the range of 0.01- 10 mg/mL) after determining the incorporated amount of Gd(III) for each sample. First, the performance of all the samples was investigated by reciprocal plotting T_1 (T_1^{-1}) values vs. MSN concentration. The obtained results revealed that post-synthesis doping of gadolinium of calcined matrices leads to better T_1^{-1} increase and longitudinal relaxivity (r_1) enhancement with increasing sample concentration compared to *in situ* synthesis gadolinium doped MSNs. This might be caused by the colloidal stability restrictions with increasing MSN concentration for the other samples, leading to deviation from linearity in the relaxivity plots. The samples $[MSN]_{cal.}$:$(Gd(Cl)_3)_{in\ situ}$, $[MSN]_{cal.}$:$(Gd(Cl)_3)_{post}$, $[MSN]_{extr.}$:$(Gd(Cl)_3)_{post}$ prepared *via* doping of $GdCl_3$ resulted in sedimentation when the concentration of the samples was increased above 2 mg/mL, which is possibly due to lack of proper stabilization mechanisms being operative in the suspension at higher concentrations. On the other hand, among the samples prepared by $Gd(acac)_3$ doping, such sedimentation was observed only for $[MSN]_{extr.}$:$(Gd(acac)_3)_{post}$ above 2 mg/mL concentration, while for the rest of the samples good dispersion stability was observed also above 2 mg/mL. By considering the measurements up to 2 mg/mL particle concentrations i.e. before deviation from linearity started to occur, plots were prepared to obtain r_1 and r_2 relaxivity values in the following figures (Figure 46 and Figure 47).

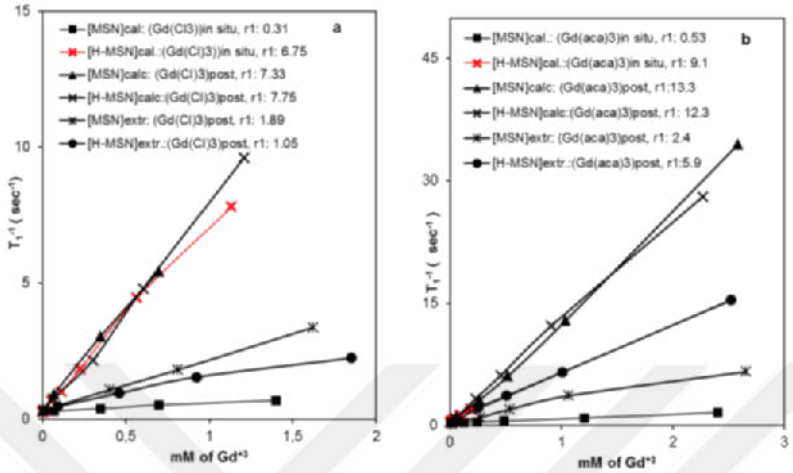

Figure 46. r_1 relaxivity values of MSN based contrast agents by doping a) $GdCl_3$ and b) $Gd(aca)_3$.

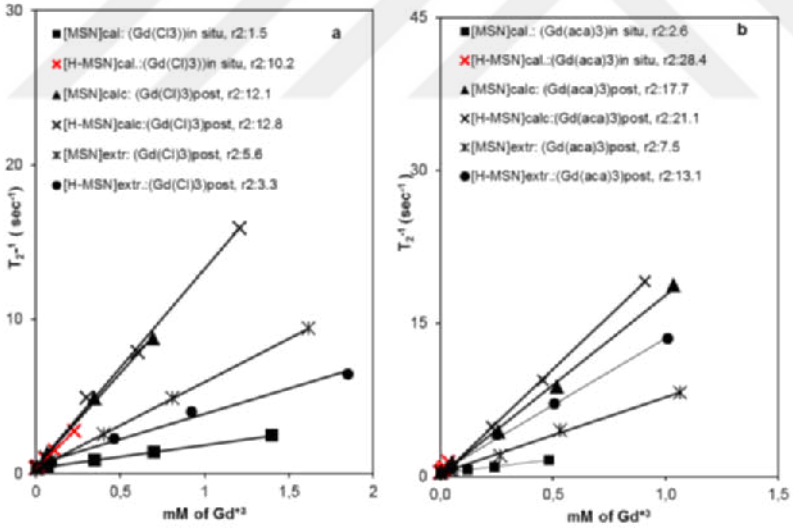

Figure 47. r_2 relaxivity values of MSN based contrast agents by doping a) $GdCl_3$ and b) $Gd(aca)_3$.

Quite remarkably, the H-MSN samples show pronouncedly better longitudinal, r_1 values compared to their corresponding regular MSN matrices especially for the *in situ* synthesis doped preparations. Even if the lowest Gd (0.1 μmol in mg of H-MSN) incorporation was obtained for *in situ* synthesis doped H-MSN, it resulted in 20-fold increase in r_1 value (6.7 $mM^{-1}s^{-1}$) compared to $Gd(Cl)_3$ *in situ* synthesis doped regular MSN ($[MSN]_{cal.}$: $(GdCl_3)_{in\ situ}$, 0.31 $mM^{-1}s^{-1}$) preparation. The obtained results clearly

present the effect of structural differences of the matrices. Namely, the pore-expanded hollow mesoporous silica nanoparticle structure (H-MSN) definitely seems to aid in achieving better diffusion of water molecules throughout these matrices to interact with the accommodated paramagnetic gadolinium centers. For the $Gd(acac)_3$ *in situ* synthesis doped MSN preparations, the same effect was also observed with 17-fold increase in the longitudinal relaxivity value (r_1) between the hollow and the regular counterparts. However, the matrix-structure-dependent variations were not observed for the post-synthesis doping protocol. The differences were mainly caused by the post-synthesis (solvent extraction vs. calcination) treatment of MSN matrices prior to post-synthesis doping of Gd. The plausible explanation for the observation could be the difference in the mesoscopic ordering of the matrices, and also, the existing organic amino groups may lead to a higher amount of Gd accommodation that can aid the shortening of relaxation times. As a result of longitudinal relaxivity (r_1) and transversal relaxivity (r_2) values, as well as calculations, the most promising MSN based T_1 contrast agents can be affirmed as $[H\text{-}MSN]_{cal}$: $(Gd(acac)_3)_{post}$) with both a low r_2/r_1 ratio of 1.6 as well as the highest r_1 relaxivity value 13.1 mM^{-1} s^{-1}. The reason for the varying r_2/r_1 ratios in Table 4 might be related to the amount as well as the distribution of Gd within the matrices, whereby in the literature the effect of high Gd was pointed to result in the suppressing the T_1 signal by T_2 relaxation.

As a brief summary of this part, it is possible to provide contrast enhancement of Gd (III) incorporated in MSN- based contrast agents by modeling the preparation and structural parameters of mesoporous silica nanoparticles (MSNs). According to our investigation, when the structural variations of the MSN matrix were considered, the *in situ* incorporation route helps to increase the longitudinal relaxivity value (r_1) of hollow pore-expanded MSNs (H-MSN). Employing *in situ* Gd(III) incorporation approach resulted in roughly 20-fold higher longitudinal relaxivity value (r_1) compared to the corresponding regular pore-sized MSN (Figure 46 b); alas simultaneously causing the highest degree of destruction on the particle morphology, which is an imperfection for the further theranostic nanoparticles design. On the other hand, structure dependent variation was not pronounced for the post-synthesis preparation route. Instead, for the post-synthesis preparation route, the most effective r_1 value enhancement was provided with the modulation of the SDA removal method. The calcination process resulted in almost 6-fold higher r_1 values as compared to solvent extraction of the corresponding MSN matrix. Therefore, while the structural variation of the MSN matrix creates significant r_1 enhancement in the *in situ* synthesis preparations, it remains the secondary regulator for the post-synthesis preparation route. As a consequence, the best contrast agent (CA) candidate was obtained by post synthesis doping of a calcined

hollow MSN matrix with $Gd(acac)_3$ ($[H\text{-}MSN]_{cal}$:$(Gd(acac)_3)_{post}$). This procedure is yielded a CA candidate with a relaxivity value of 13.1 $mM^{-1}s^{-1}$, which is approximately 4-fold to clinically used Gd-based molecular CAs. The r_2/r_1 ratio of 1.6 is rendering the CA candidate predominantly a T_1 contrast agent since, in the literature, the contrast agents with the r_2/r_1 value from 1.1 to 2.0 are attributed to a T_1 type contrast agent, and over 2.0 is typically T_2 type contrast agents.[148] Ultimately, cells tolerated this most promising MSN-based CA candidate well. In our case, assuming a cellular uptake of 100%, the highest used Gd(III) concentration in the cells would be 30 μM which is considerably lower than the toxicity level of Gd(III) reported as 1 mM for HeLa cells .[149]

5.3.3 Targeted Delivery of Cargo Molecules by Mesoporous Silica Nanoparticles

In the existing chemotherapeutic methods for cancer treatments, serious side-effects due non-specific delivery of drugs to the health cells can be prevented by cancer cell-specific drug delivery systems. When the cancer drugs are considered, they are mainly hydrophobic, which also make the direct administration of drugs challenging. In nanomedicine research, there are numerous of studies aiming to design targeted drug delivery systems in order to overcome the problem.

In PAPER III and SUPPORTING PAPER IV, VI the research was concentrated on designing MSN based targeted drug delivery systems for therapeutic purposes.In PAPER III, rod-shaped silica nanoparticles which were abbreviated as NR-MSPs were surface modified with chitosan and chitosan conjugated with affinity ligand folic acid by means of active cellular targeting for the delivery of potential anti-cancer drug anisomelic acid (AA) to folate receptor (FR)-enriched cancer cell surfaces by conjugating folic acid (FA) on the particles. The design of material presented in detail in Figure 48.

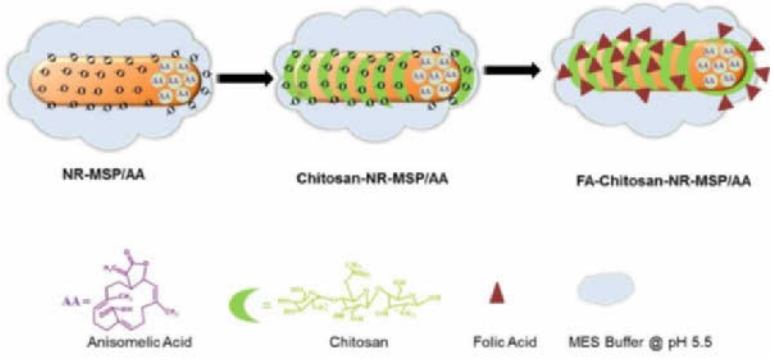

Figure 48. Schematic presentation of designed NR-MSPs for targeted drug delivery of the potential anticancer drug.

The prepared particle design possesses the advantages of one of the few natural cationic biopolymer chitosan, which was electrostatically adsorbed on the NR-MSPs after drug loading which provided better dispersibility for the drug-loaded NR-MSPs and act as capping agent for the pores of NR-MSPs with also the known pH-responsive property of it. Furthermore, folic acid (FA) conjugated chitosan was used for coating with the aim of uptake enhancement by means of active cellular targeting. The succeeded chitosan coating was analyzed by TGA and calculated as 10 w/w % and the FA amount was analyzed by UV-Vis analysis and estimated as 0.025 w/w %. In the cellular uptake part of the study, human cervical cancer cells (SiHa and HeLa) and noncancerous embryonic kidney epithelial cells (HEK 293) was evaluated by using flow cytometry (FACS) and confocal microscopy techniques. Enhanced internalization of Chitosan-NR-MSP was observed with increased concentration and longer time of incubation Figure 49.

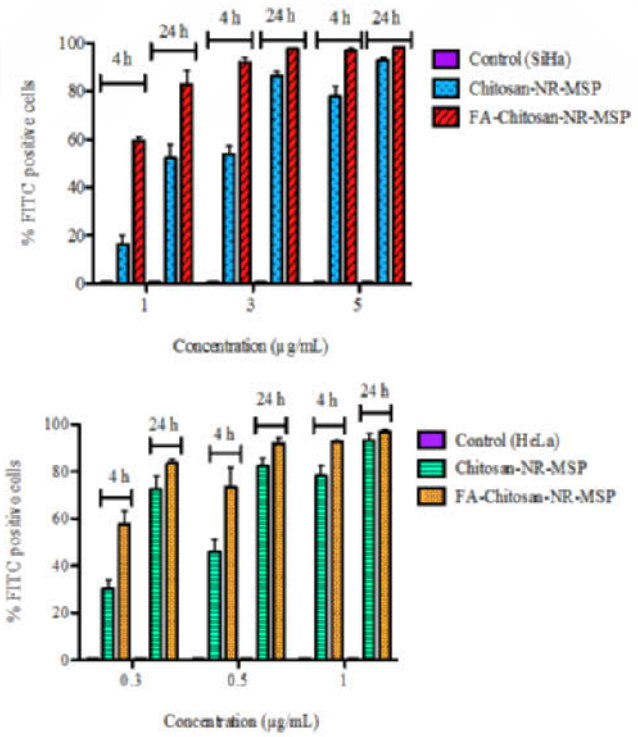

Figure 49. Cellular uptake of Chitosan-NR-MSP and FA-Chitosan-NR-MSP in (A) SiHa and (B) HeLa cell lines measured by flow cytometry. Error bars represents SD n≥3. (PAPER III)

The difference in internalization of FA-Chitosan–NR-MSP and Chitosan-NR-MSP was observed at lower concentrations, which reveal that in the higher concentrations treatment, the saturation capacity was already reached. The difference becomes clear when the histogram profiles and normalized mean fluorescence intensity (MFI) of Chitosan-NR-MSP and FA-Chitosan-NR are compared at concentration 1 µg/mL for HeLa, SiHa, and HeK-293 cell lines.

As presented in Figure 50, an increase in cellular uptake is clear with increased folate receptor amount on the cell line with the order of HeLa>SiHa>HeK293.In addition a clear difference was observed in the confocal microscopy images of SiHa, HeLa and HEK 293 cells treated with Chitosan-NR-MSPs and FA-Chitosan-NR-MSP (1 µg mL^{-1}-1of Chitosan-NR-MSP and FA-Chitosan-NR-MSPs show that the Chitosan-NR-MSPs were localized in the cytoplasm while the FA-Chitosan-NR-MSP accumulated more closely around the nucleus (Figure 51).

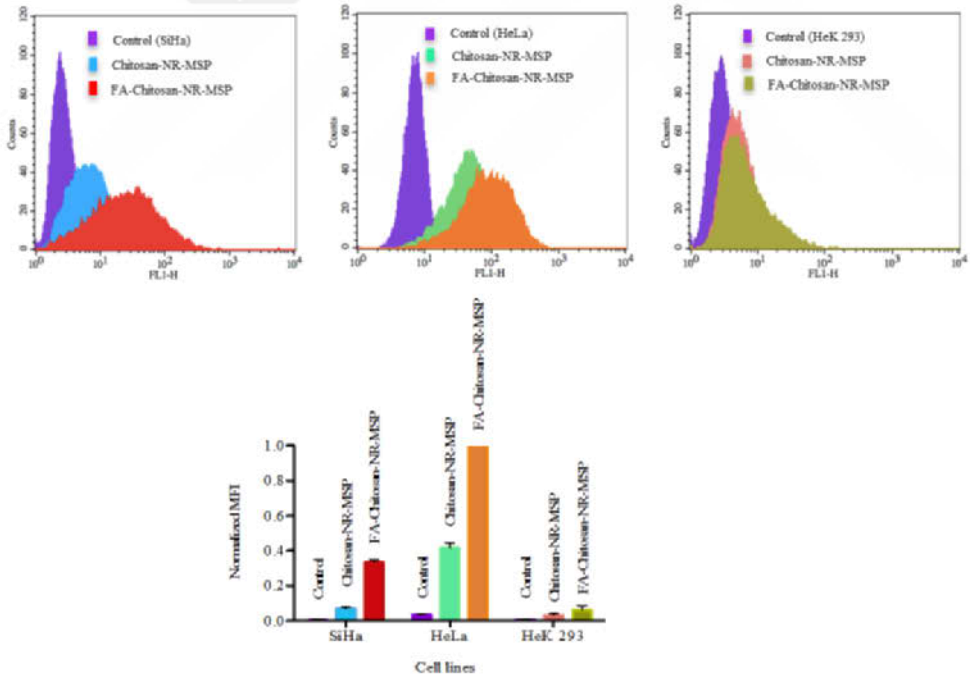

Figure 50. Histogram profiles of cervical (SiHa and HeLa) and human embryonic kidney HEK 293 cell lines incubated with 1 µgmL^{-1} of Chitosan-NR-MSP and FA-chitosan-NR-MSP b) Normalized fluorescence Intensity (MFI) of chitosan-NR-MSP and FA-Chitosan-NR-MSN(1 µgmL^{-1}). Error bars represents SD n≥3. (PAPER III)

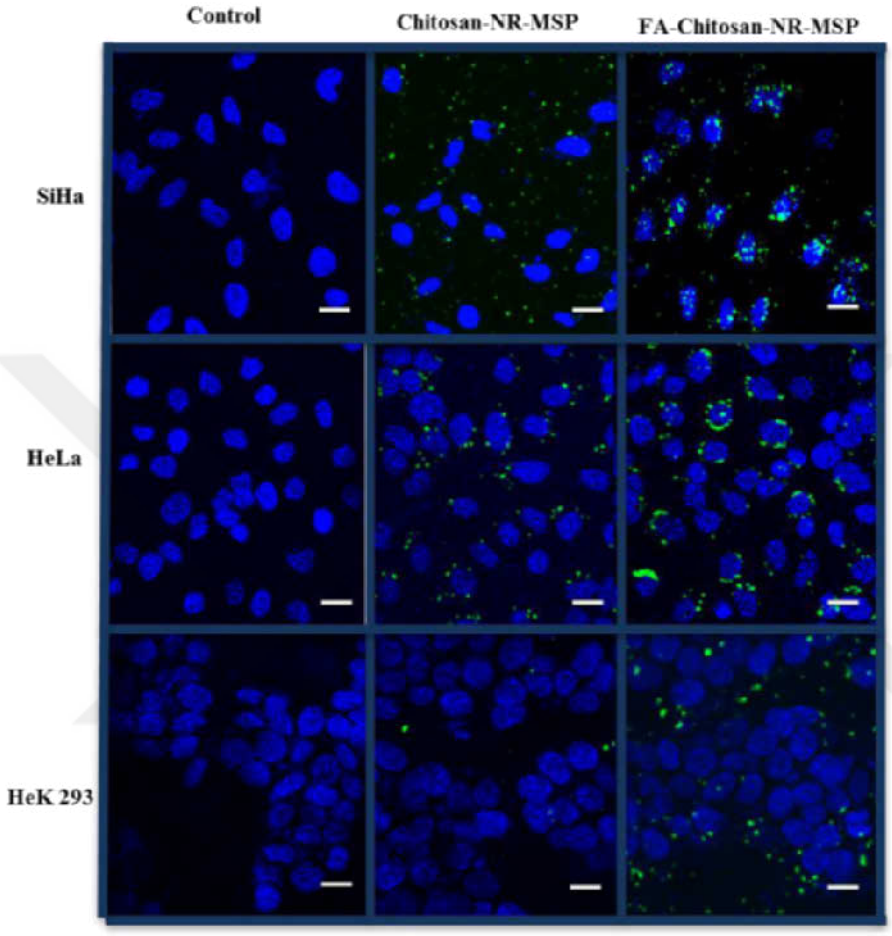

Figure 51. Confocal microscopy images showing the intracellular uptake of FITC-labelled Chitosan-NR-MSPs (green) in SiHa, HeLa and HEK 293 cell lines incubated for 4 h. Nuclei were stained with DAPI (blue). Scale bar: 10 μm.

In the same study, enhanced apoptosis effect was observed with AA loaded FA-Chitosan-NR-MSN samples compared to AA loaded Chitosan-NR-MSN and free AA at the corresponding concentration of loaded ones. The cell death assessment was carried out by caspase-3 activation assay and presented in Figure 52. About 3.5 fold increases in caspase-3 activation of SiHa cells was observed when the cells were exposed to AA-loaded FA-Chitosan-NR-MSNs as compared to free AA at corresponding AA concentration in loaded carriers. There is also an evident difference in the apoptotic cell percentage.

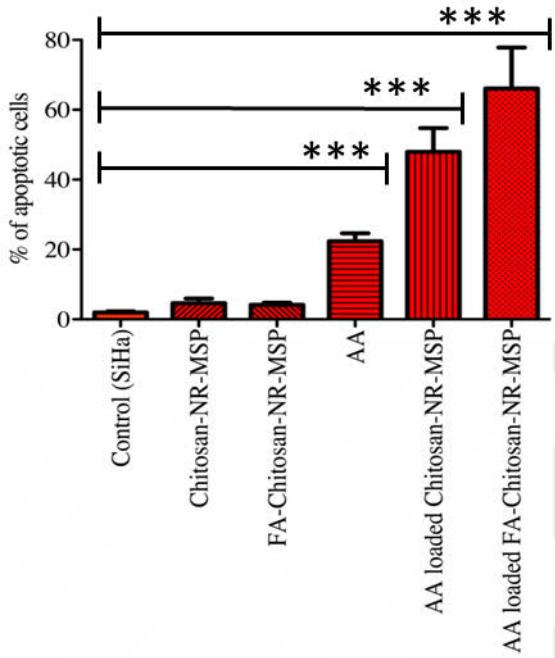

Figure 52. Cells were incubated with 20 μM free AA and AA-loaded Chitosan-NR-MSN at corresponding AA concentration for 24 h. The percentage of apoptotic cells were determined by the determination of cells that contained activated caspase-3.Error bars represents SD n≥3 , *p<0.05, **p<0.01, ***p<0.001.

In SUPPORTING PAPER VI, various surface modification strategies was employed by utilizing polymeric (PEG, PEI) coatings and affinity ligand (FA) in different combinations, to evaluate the effect of surface modification on their feasibility as targeted oral drug delivery carriers, was investigated. HT-29 and Caco-2, both are folate receptor positive cell lines, were employed to find out the cellular uptake differences and FA modification. Only the uptake of PEGylated particles (PEG-MSNs) was enhanced by FA modification but it did not add further benefit to PEG-PEI-MSNs at the studied concentrations. The reason of such an observation might be due to the inherent high uptake of PEG-PEI- modified particles, which have already reached the saturation level.[150] Consequently, further modification with FA has no advantage in these cases in terms of total uptake. A boosting effect of FA on cellular uptake was only, but clearly, detected in the case when FA was linked to PEGylated particles where PEG was conjugated to the MSNs directly, without an intermediate PEI layer; and for which the basal uptake was low.

During the investigation of ligand-mediated cellular uptake, it is important to optimize the design of ligand containing portion on the surface modified nanoparticles in order to obtain ligand-mediated delivery of therapeutics.

5.4 Evaluation of Silica Nanoparticles in Biological Environment and Cellular Uptake

5.4.1 Interactions of Silica Nanoparticles in Physiological Media

Controlling the interaction of nanoparticles with biological systems is an essential challenge. When nanoparticles are contacted with the biological matrices protein corona is formed when the nanoparticles are exposed to the existing proteins in the medium.[151] The adsorbed proteins determine the identity of the particles in a biological environment which is usually different from its synthetic identity. The biological identity of the particles determines their responses including agglomeration, cellular uptake, circulation lifetime, kinetics, transport, accumulation, and toxicity. The formed protein corona around the particles causes the changes in the size and interfacial properties of the particles, also mediates the interaction of nanoparticles with biomolecules, membranes, and physical barriers.[152]

Protein corana formation highly affected by nanoparticle size, shape, curvature, net surface charge (zeta potential), solubility, surface modification, and route of administration of nanoparticles. These parameters have been reviewed recently by various research groups.[153,154,155] The impact of particle's surface properties on the adsorption of the protein species was reviewed by Aggarwal *et al.*[156] In their review, literature reports about the effects of particles surface properties were evaluated and according to literature reports, the increment in the plasma protein adsorption on the nanoparticles was observed for the polymeric nanoparticles with net negative surface charges (keeping their sizes and hydrophobicity approximately constant).[157] On the other hand, for the polystyrene nanoparticles with positive zeta potential value, the proteins with isoelectric points less than 5.5 (as albumin) was adsorbed preferentially whereas the proteins with isoelectric points higher than 5.5 (as IgG) bound to negatively charged particles. In another study, enhanced adsorption of plasma proteins onto hydrophobic particles was reported. The diversity in size and morphology, surface curvature and area of particles also resulted in the alteration of protein adsorption.[158]

In one of the literature reviews, the influence of nanoparticles PEGylation on eliminating and controlling the protein adsorption was also emphasized.[159] In PAPER I, stealth effect of PEG, which is one of the most frequently claimed advantages for employing PEG in biomedical applications, was studied for prepared 100 SiNPs. Bovine Serum Albumin (BSA) was used as a protein source since it is the major component of Fatal Calf Serum (FCS) used serum-supplement in *in vitro* cell cultures. Adsorbed amount of protein per surface area of 100 SiNPs were estimated after 4h and 24h incubations of 100 SiNPs with BSA. UV-VIS spectroscopy analysis was carried out to estimate the adsorbed amount of proteins on the particles. In the

following Figure 53, the highest amount of protein adsorption was observed for the PEI-coated 100 SiNP and the mPEG grafting on PEI in coatings resulted in the reduction of the adsorbed protein amount as compared to PEI-coated 100 SiNP. Even if the PEG on the particles is frequently claimed approach to prevent nonspecific protein adsorption, the same clear-cut effect was not observed in our samples. This should be due to the architecture of how the PEG portions are placed on the 100 SiNP surfaces. In the same study, the distance (d) between two attached PEG chains after copolymer adsorption was calculated by assuming that the PEG parts of the $mPEG_{high}PEI$ did not contribute to the adsorption process of copolymer onto SiNP surfaces, and instead be fully stretched out from the particle surface. The obtained distance values were estimated to about: 4.5 and 2 nm for SiNP $mPEG_{low}$-PEI and PEG_{high}-PEI coated particles which were mainly higher than the threshold limits of 1 nm and 1.5 nm for the adsorption of small and big proteins respectively. In the report of Malmsten *et al.*[160], they have claimed that only high enough interfacial density of PEG chains could result in efficient protein rejection on flat surfaces, irrespective of the underlying surface chemistry and coupling chemistry used to attach the PEG chains. The reason for the highest amount of protein adsorption on PEI-coated 100 SiNPs can be explained as a result of electrostatic interactions. Since the ζ-potential values of the PEI-coated SNPs are positive (+ 56 mV) at pH 7.2 (HEPES media), and the net surface charge of the protein species used are negative (-12 mV) for BSA in HEPES, the electrostatic attractions become dominant and results in protein adsorption.

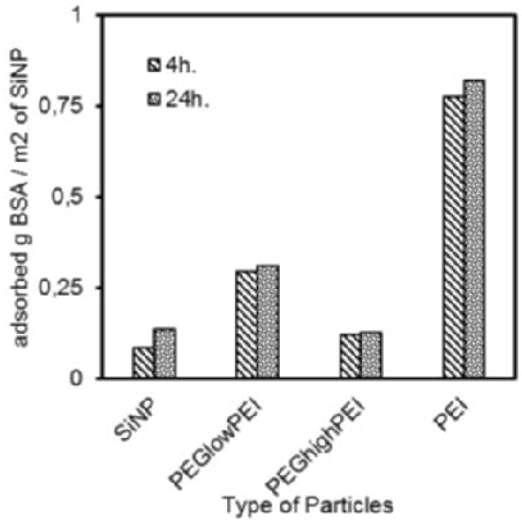

Figure 53. Adsorbed BSA amount on non-coated and $mPEG_{low}PEI$ and $mPEG_{high}PEI$ and PEI coated100 SiNPs.

In order to confirm the compliance between adsorbed BSA and cell media-exposed 100-SiNPs, the particles were incubated for 2 h in cell media, containing all components also used for cell culturing including serum, whereafter the particles were separated by centrifugation and redispersed in HEPES buffer solution (pH 7.2, 25 mM). The ζ-potential values of cell media-exposed particles were compared to that of the ζ-potential values of the same particles after BSA-adsorption. Even if the absolute values were not identical, which would also be expected given the much more complex composition of cell media, the trends observed were similar (Table 5) with decreasing absolute ζ-potential values for PEI > $mPEG_{low}$- PEI> $mPEG_{high}$-PEI.

Table 5 ζ-potential values of 100-SiNPs in 1) HEPES buffer, 2) after 2h incubation in serum-supplemented cell media (DMEM) and redispersion of the separated particles in HEPES buffer, and 3) after BSA adsorption and redispersion of the separated particles in HEPES buffer. Each value is an average of three measurements.

SAMPLES	ζ-potential value [mV][1]	ζ-potential value [mV][2]	ζ-potential value [mV][3]
100-SiNP-PEI	56	-32	-20
100-SiNP-$mPEG_{low}$PEI	8	-14	-8
100-SiNP-$mPEG_{high}$PEI	-1	-6	-2

1:In HEPES buffer (25 mM) pH 7.2
2:After 2h incubation in cell media and redispersion in HEPES buffer
3:After BSA adsorption (in HEPES buffer)

In the unpublished experiments of the thesis, the hydrodynamic size and ζ-Potential values of MSNs were analyzed before and after BSA adsorption in order to compare their synthetic and biological identities. MSNs that were given in section 5.1 with the labeling 1C, 1D were analyzed with and without surface modifications by keeping the particles in bovine serum albumin (BSA) solution at two different concentrations of 100 µg/mL and 200 µg/mL, and the treatment durations were altered as 3h. and 24h. The surface modification of 1D was carried out by electrostatic adsorption of PEI polymer and in-the-lab prepared $mPEG_{low}$PEI and $mPEG_{high}$PEI copolymers. The existing organic portions on the MSNs was analyzed by thermogravimetric analysis method (TGA) and the values were estimated as 1.02, 19.7, 21.0, 28.6 w/w% for the samples 1D,1D-PEI_{ads}, 1D-$mPEG_{low}$PEI and 1D-$mPEG_{high}$PEI respectively.

After treating the MSNs in BSA solutions, the particles were centrifuged, collected and redispersed in HEPES buffer solution and the hydrodynamic size and

the ζ-potential values of MSNs were analyzed. In Table 6 clear differences were observed before and after BSA treatment which can be assigned to the interaction of proteins with particles, resulted in protein adsorption on the particles. The presented values in for the hydrodynamic size of PEI modified MSNs, 1D-PEI, was not altered significantly after 3h BSA treatment compared to starting values whereas the difference becomes obvious as the treatment duration increased to 24h. For the 1D-mPEG$_{high}$PEI sample, the hydrodynamic radius value and PDI value become lower compared to the starting sample, which means the interaction of the proteins and 1D-mPEG$_{high}$PEI aids to provide better dispersibility for particles. This could be due to the interaction of proteins with the PEG portions of the 1D-mPEG$_{high}$PEI sample via hydrogen bonding. The hydrogen bonding is one of the probable interactions between surfaces and proteins. The rest are described as repulsive and attractive ionic interactions, hydrophobic interactions, hydration forces, acid-base interactions, van der Waals interactions and steric repulsion.[161]

Table 6. MSNs hydrodynamic size and ζ-potential values in HEPES buffer solution (25mM pH7.2) before and after BSA adsorption.

SAMPLE NAME	Hydrodynamic size [nm]^0	PDI^0	ζ-Potential [mV]^0
1C	322±6.4	0.3	-44
1D	450±7.1	0.3	-11
1D-PEI ads.	321±2.5	0.2	44
1D-mPEG$_{low}$PEI ads.	297±5.7	0.05	27
1D-mPEG$_{high}$PEI ads.	1391±233	0.6	2

SAMPLE NAME	Hydrodynamic size [nm]^1	PDI^1	ζ-Potential value [mV]^1	Hydrodynamic size [nm]^2	PDI^2	ζ-Potential value [mV]^2
1C	417±14	0.5	-39	288±4	0.3	-40
1D	540±29	0.4	-17	538±13	0.3	-16
1D-PEI ads.	365±3	0.09	-8.6	3350±490	0.6	-7
1D-mPEG$_{low}$PEI ads.	278±5	0.08	-10	340±4	0.2	-11
1D-mPEG$_{high}$PEI ads.	306±1	0.1	-9	495±17	0.4	-11

1:MSPs before the treatment in BSA solution
2: After treating the MSPs for 3h. in 200 µg/mL BSA solution
3: After treating the MSPs for 24h. in 200 µg/mL BSA solution

The results plotted in Figure 54 reveal that there is a clear change in the adsorbed amount of BSA with time. The highest amount of protein adsorption has accrued for the 1D-PEI sample with the decreased order of 1D-mPEG$_{low}$PEI,1D and 1D-mPEG$_{high}$PEI and 1C. The time-dependent decrease is more significant for 1D-mPEG$_{low}$PEI samples compared to 1D and 1D-mPEG$_{high}$PEI samples. This could be due to formed multilayers with the protein adsorption in which the subsequent layers will be attached considerably weakly compared to the first layer which is interacting directly with the surface of MSNs. As the adsorption become loose in

subsequent layers, the exchange of the protein from adsorbed part to bulk protein solution becomes more facilitated.[162] The difference between $mPEG_{low}PEI$ and $mPEG_{high}PEI$ coated MSNs becomes more evident compared to the results obtained in Figure 53 with the increased amount of PEG on the samples in which the adsorbed amount of protein is decreasing. In addition, a clear difference is observed between the pristine 1D and 1C samples. This could be due to the existing amine groups on MSNs surfaces. As it was mentioned in one of the literature studies additions of monoamines and diamines into adsorption solutions of proteins helps to quench the adsorption on the bare silica surfaces.[163] The same trend is also observed in this part of the study, existing amine groups on solvent extracted sample (1D) yields the increment in protein adsorption. It is clear that the difference in the density of silanols and presence and absence of organic residues have played a major role in the resulting protein adsorption.

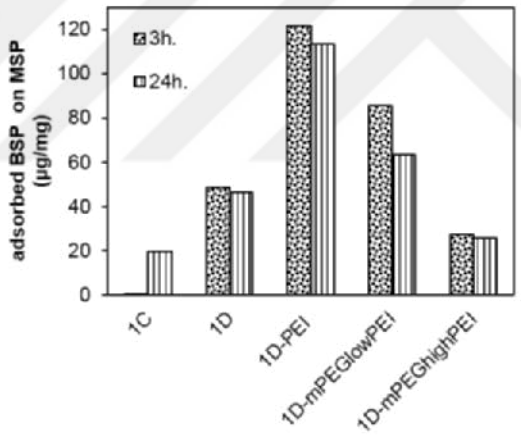

Figure 54. Adsorbed BSA amount on non-coated calcined, solvent extracted MSNs and copolymer coated calcined MSNs.

5.4.2 Intracellular Interactions of Silica Nanoparticles

The effect of provided colloidal stabilization mechanisms on the intracellular interaction was examined in PAPER I. *In vitro* microscopy imaging was carried out by confocal microscopy in order to compare the cellular uptake of $mPEG_{low}$-PEI, $mPEG_{high}$-PEI surface modified and bare 100 SiNPs. *In vitro* imaging of cancerous HeLa cells was carried out with the surface modified 100 SiNPs at copolymer concentrations, which was found to be the optimal level for dispersing and stabilizing the SiNP system. A clear difference in intracellular pattern after cellular

uptake was observed between non-coated, mPEG $_{low}$ -PEI and mPEG$_{high}$-PEI coated SiNPs (Figure 55).

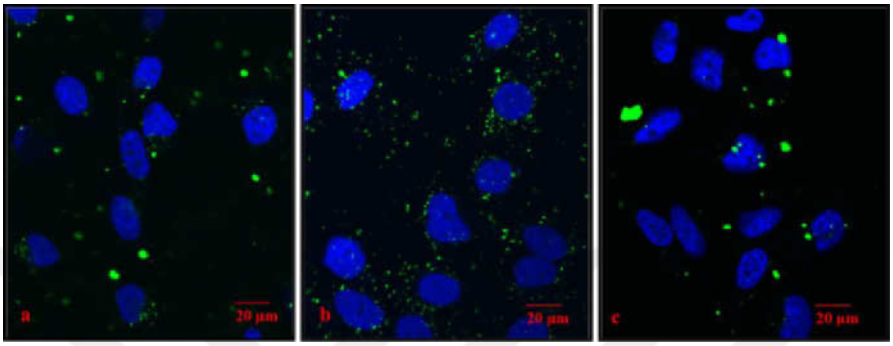

Figure 55. In vitro confocal fluorescence images of (a) non-coated and (b) PEG$_{low}$PEI and (c) mPEG$_{high}$PEI coated 100 SiNP in HeLa cells after 4 h incubation. All images are confocal sections through the nucleus and the nuclei of cells are stained with DAPI (blue color) (PAPER I).

The images in Figure 55 reveal that the effective amount of PEG chains exposed on the surface with the correct conformation is decisive rather than the total concentration of PEG on the particles has a great impact to prevent aggregation of particles during the cellular interactions. In addition, to obtain efficient colloidal stability under biological conditions, both steric and electrostatic contributions are needed the dominant effect of which cannot be isolated.

In PAPER II, the behavior of MSNs at the nano-bio interface was also investigated as *in vitro* studies in cellular models. For this purpose, two similarly sized but differently shaped, rod-shaped and spherical shaped, mesoporous silica nanoparticles were prepared and the cellular internalization performances were compared. Furthermore, both types of particles were functionalized to obtain different surface charges in order to find out the dominant effect that induces the cellular internalization of the presented strategies in Figure 56. In *vitro* studies were carried out in two different cancer cell lines, HeLa (cervical carcinoma cells) and Caco-2 (human epithelial colorectal adenocarcinoma cells), to investigate the impact of particle characteristics on cells of different origin. The influence of morphology alterations and surface modifications on cellular uptake was investigated by flow cytometry and confocal microscopy imaging techniques in PAPER II.

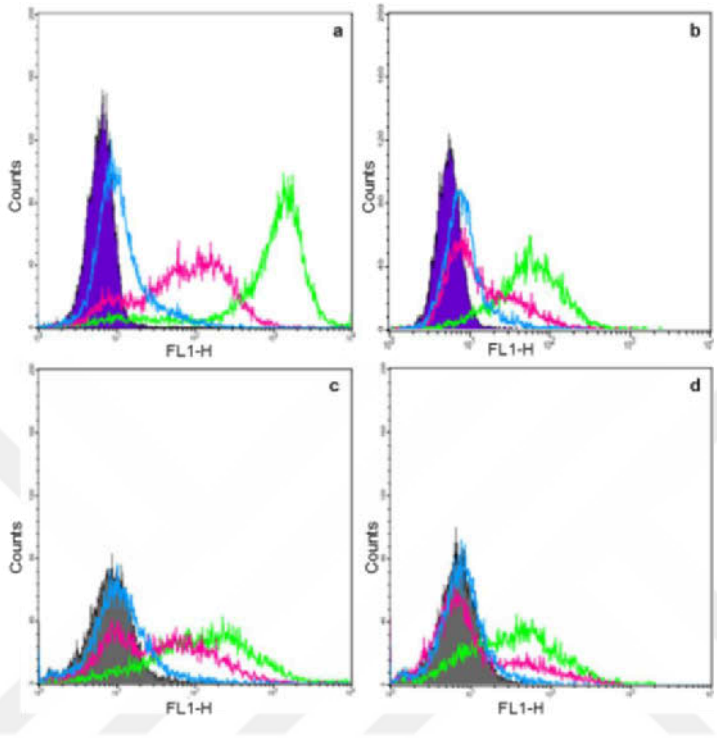

Figure 56. Cellular uptake of uncoated MSNs in two different cancer cell lines after 4-h incubation. (a) HeLa 10 μg/ml, (b) HeLa 2 μg/ml,(c) Caco-2 10 μg/ml and (d) Caco-2 2 μg/ml; NR-MSP (green), S-MSN1 (pink) and S-MSN-2 (blue). The shaded area is the control (no particles) (PAPER II).

First, the cellular uptake of unmodified fluorescently labeled particles with spherical (S-MSN) and rod-like morphologies (NR-MSP) was studied. Two different concentrations (2, 10 μg/mL) were tested in order to find concentration and morphology-dependent variations. In order to detect cell-internalized particles, the extracellular fluorescence was quenched for both FACs and microscopy studies. In Figure 56, the histogram plots were given in order to compare the preferences of two cell line for spherical and rod-shaped particles. In Figure 56, the peaks of S-MSN2 in histogram plots are not shifted significantly from the control, and bimodal peak distribution was observed for the S-MSN1 which indicates low cellular uptake. The observed difference between two spherical particles plausibly due to the difference in the net surface charge of the particles, in which S-MSN1 is negatively charged (ζ-potential value -18 mV in HEPES buffer) to resemble the pristine silica material whereas S-MSN2 is a co-condensed material consisting of basic aminopropyl groups on the surface of the material and which are counteracting the acidic silanol groups responsible for the negative charge of silica surfaces, thus resulting in a net

neutral charge (ζ-potential value ~0 mV in HEPES buffer) under the studied conditions. The NR-MSPs were fluorescently labeled via post-synthesis functionalization to yield a sufficient fluorescent labeling, so the surface of NR-MSP resembles S-MSN1. The measured ζ-potential value of NR-MSP was -16 mV in HEPES buffer, so the S-MSN1 and NR-MSP can be compared to find out the shape effect on the cellular internalization. The difference between S-MSN1 and S-MSN2 can be due to the serum protein adsorption onto particles and coronation, which leads to enhancement in the unspecific cellular uptake of negatively or positively, charged particles. Therefore, two net negatively charged S-MSN1 and NR-MSP could be exposed to higher protein adsorption compared to net neutral charged particles (S-MSN2) and result in increased cellular uptake. Beside this, the aggregation of S-MSN2 in the physiological environment might be possible, due to the absence of surface coating to provide electrostatic or steric stabilization for S-MSN2. The observed significant peak shift in the histograms of the NR-MSPs clearly supports the findings in literature about the preferred cellular uptake of rod-shaped particles over spherical particles.

The cellular internalization of organically modified particles with different net surface charges was investigated. For this purpose, high positive surface charge was provided with cationic polyelectrolyte polyethyleneimine (PEI) by surface grafting method. In addition, the effect on cellular uptake upon derivatization of the PEI layer was investigated by capping the terminal primary amino groups with either uncharged acetyl groups or acidic (negatively charged under neutral conditions) succinic acid groups. Furthermore, PEI surface functionalization method was verified by electrostatic adsorption of the hyperbranched PEI polymer on the surface of particles. The uptake in terms of positive cell percentage of the whole series of the particles with (or without) different functionalization was investigated with two different concentrations (2 and10 μg/mL) on both Caco-2 and HeLa cell lines as presented in Figure 57.

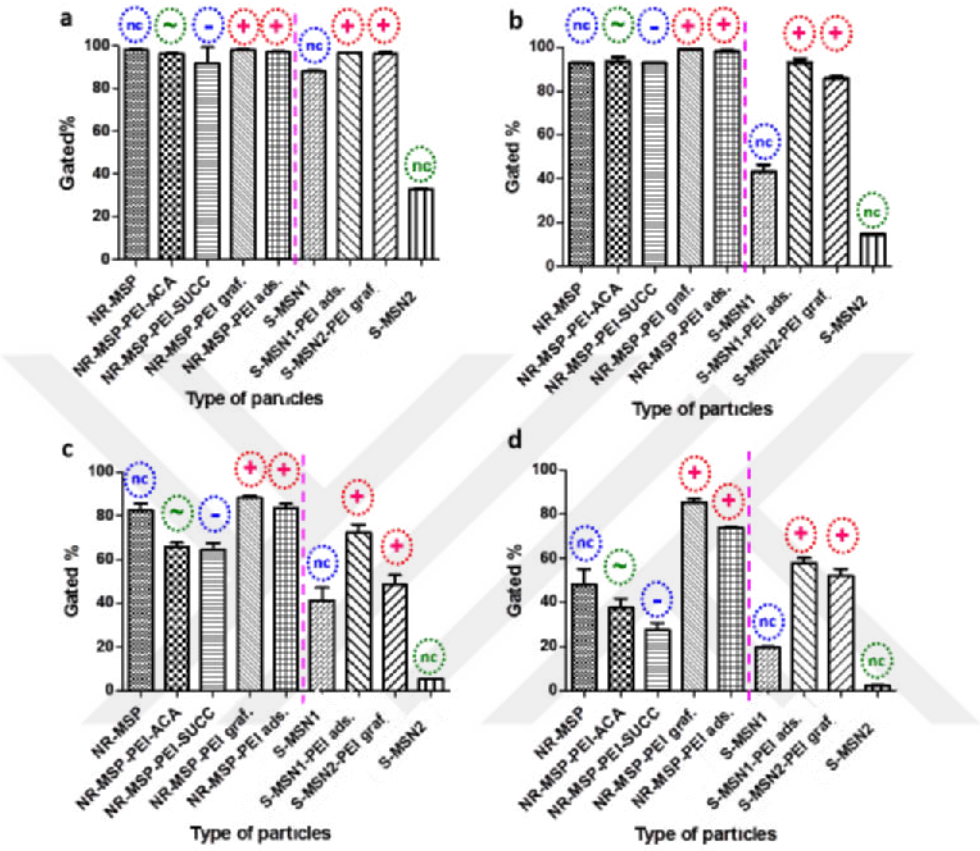

Figure 57. Cellular uptake efficiency. Cellular uptake of coated vs uncoated rods vs spheres in HeLa ((a) 10 μg/ml and (b) 2 μg/ml) vs Caco-2((c) 10 μg/ml and (d) 2 μg/ml) cell lines after 4 h incubation, as measured by FACS. Error bars represent SD (n≥4). The pink dotted line distinguishes the rods from the spheres (PAPER II).

For HeLa cells, almost no difference was observed in the level of NR-MSNs cellular uptake for 2 μg/mL with different surface modifications whereas decreased uptake of NR-MSNs was observed at 2 μg/mL concentrations with surface modifications. For Caco-2 cells, the differences become obvious and surface-charge-induced differences are also clear. Capping the charge with uncharged groups reduces the uptake, but a negative charge seems to reduce it even more. This effect is even more evident from the graph of normalized fluorescence intensity vs type of particles in Figure 58 where MFI values from FACS have been normalized against particle-specific fluorescence in suspension.

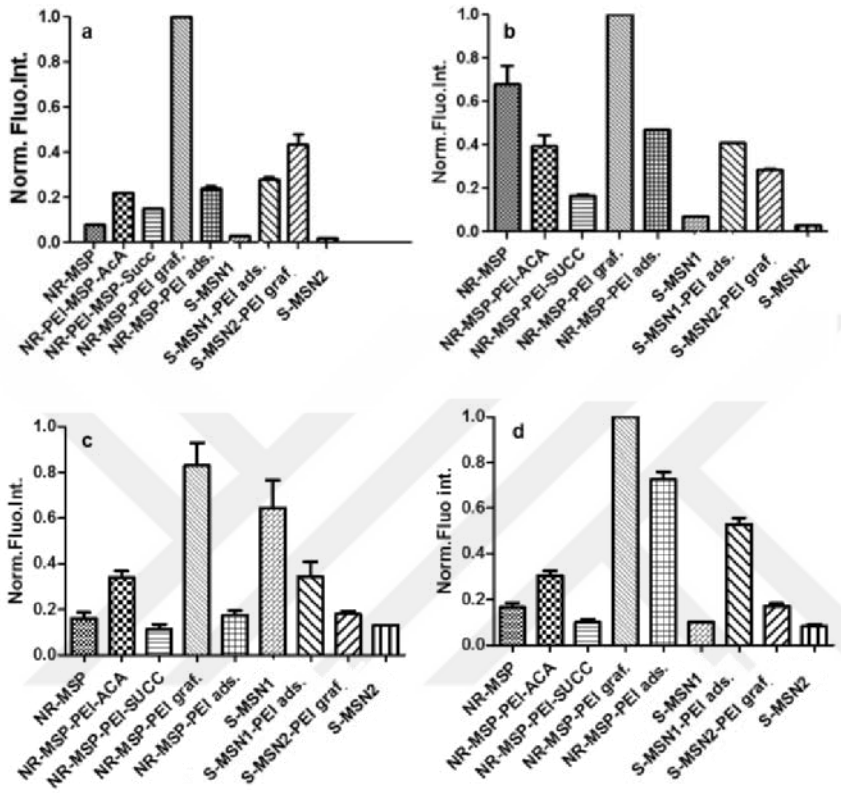

Figure 58. Normalized pure particles suspension fluorescence intensity values measured at 530 nm in HEPES buffer solution against MFI values from FACS for Hela with a) 2μg/mL and b) 10μg/mL MSN incubation and Caco-2 cells with c) 2 μg/mL and d) 10μg/mL MSN incubation for 4h. Error bars represents SD n≥3.(PAPER II).

The observed difference is probably due to the fact that the absolute charge is not neutral, but still, a competition between negatively charged silanols on the underlying silica surface and secondary and tertiary amine groups in the PEI layer results in a net neutral effective charge. As this net effective charge recorded at neutral pH was even slightly negative, the capping of the terminal primary amines seems to have been very effective as it has been able to shield the positive charge. The terminal acetyl groups are serving as 'charge capping' and reduce uptake observed for positively charged particles. On the other hand, the succinylation provides for terminal negatively charged groups on the organic layer which, together with the secondary and tertiary amine groups in the PEI layer (or any residual primary amines), creates zwitterionic functionalization with the organic layer consisting of both negative and positive charges. Such composition of surface on silica

nanoparticles has also been suggested to minimize serum protein adsorption, which could also lead to decrease in unspecific uptake. Thus, it may not be the negative charge as such that reduces the uptake but the zwitterionic nature of the organic layer.[106]

For HeLa cells no distinctions were obtained with the surface functionalization and particles are all taken up almost in 100% of the cells. But for HeLa cells, at lower concentrations (1 μg/ml), the charge-induced differences started to occur as shown in the histogram presented in Figure 59 with the same trend, i.e., the positively charged rod-like particles are taken up to a greater extent.

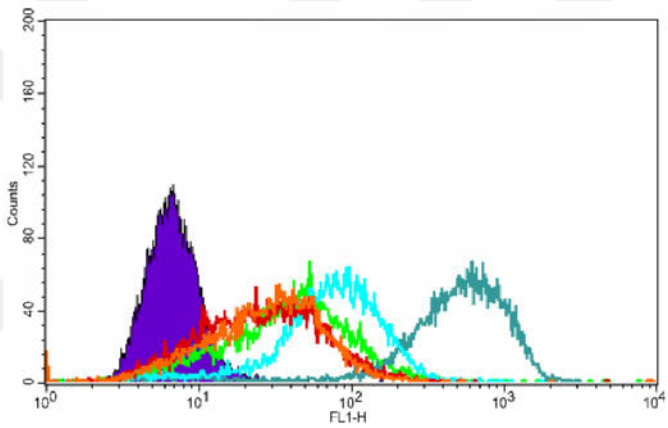

Figure 59. Charge-induced differences in cellular uptake of particles. Incubation of NR-MSNs in HeLa cells at a low concentration (1 μg/ml), NR-MSN (green, 83.6%),NR- SP-PEI-ACA (red, 62.4%), NR-MSN-PEI-SUCC (orange, 69.6%), NR-MSN-PEI adsorbed (light blue, 93.2%), NR-MSN-PEI grafted (teal, 97.9%) and control (violet) (PAPER II).

According to the presented results, particle morphology is a decisive property regardless of both the different surface charges and doses tested, whereby rod-like particles internalized more efficiently in Caco-2 and HeLa cell lines. Performed uptake studies in different cell lines reveal that along with particle shape and surface functionalization, cellular origin and features may also influence the uptake of particles in cells. In addition, at lower doses where the shape-induced advantage is less dominant, charge-induced effects can, however, be used to fine-tune the cellular uptake as a prospective 'secondary' uptake regulator for tight dose control in nanoparticle-based drug formulations.

6 CONCLUSIONS AND OUTLOOK

Diverse design strategies for the preparation of multifunctional silica nanoparticles were presented in this thesis with the focus on their utilization in therapeutic, diagnostic, or both, in theranostic applications. The investigations of this study revealed that among the employed modular design strategies, modifying the surface characteristics of silica nanoparticles possess great impact on the fate of particles in biological environments. In the case of copolymer surface modification of silica nanoparticles, only when proper composition and architecture of copolymers was provided, joint electrostatic and steric stabilization could be obtained. The combined stabilization mechanism resulted in efficient colloidal stability of the particles under biologically relevant conditions and also well distributed intracellular particle patterns.

The structural and morphological diversification of mesoporous silica nanoparticles (MSNs) was carried out to improve the drug loading capacity of unmodified MSNs for therapeutic applications. Among the prepared MSNs, the hollow structured and pore expanded particles offered 100 w/w% loading capacity as a drug carrier.

Imaging and cell labelling capability of silica nanoparticles was also attempted to be tuned for diagnostic applications. The surface properties (environment that the fluorophores was exposed due to their incorporation in MSN matrix), structural and morphological features of MSNs and incorporation strategy of imaging agents was extensively explored. To image silica nanoparticles with fluorescence imaging techniques, the most critical points were stated as the environment of the fluorophore (especially for pH-sensitive fluorophores) that it was exposed to and also the concentration of fluorophore (for both pH-sensitive and insensitive fluorophores) in the analysis environment. Controlling the mentioned points aided the quantification of fluorophore-labelled silica nanoparticles in fluorescence-based analyses. The impact of morphology and imaging agent incorporation strategies were determined as being critical parameters also when the mesoporous silica nanoparticles are designed as contrast agents for magnetic resonance imaging.

The impact of morphological and surface properties of silica nanoparticles on interactions in physiological media and their intracellular interactions was evaluated. The findings revealed that highly positively charged particle surfaces enhanced the cellular internalization of particles when compared to their net negatively or net neutrally charged counterparts. In order to boost the therapeutic effect of silica nanoparticles, their morphological features were altered. Elevated cellular uptake efficiency was obtained with the rod-shaped silica nanoparticles compared to spherical shaped particles regardless of the employed dose and surface charges. Additional to morphological features of the particles, surface modification with

conjugated targeting moiety aided to provide better therapeutic efficacy on the tested cancer cells when MSNs were employed as drug carriers.

The results presented in the thesis are believed to provide deep insight into the critical preparation steps of silica nanoparticles with diverse physicochemical properties. The impacts of the obtained features on biomedical applications were also evaluated. This knowledge facilitates the preparation of silica nanoparticles with desired properties and aids to predict their fate in biomedical applications. Currently the gained information from the study is used to prepare theranostic silica nanoparticles for a variety of research projects. For instance, antibacterial nanoparticles have been developed as an alternative platform of traditional antibiotics treatment. We believe that this decade's one of the most threatening problem, antibiotic resistance can be solved by this way.

7 REFERENCES

[1] Editorial "Nanomedicine: A Matter of Rhetoric?," Nature Materials **5**, 243-243(2006)

[2] Chen, Y., Hangrong, C., Zhang, S., Chen F., Zhang L., Zhang, J., Zhu, M. Multifunctional Mesoporous Nanoellipsoids for Biological Bimodal Imaging and Magnetically Targeted Delivery of Anticancer Drugs, *Advanced Functional Materials* **21**, 270–278 (2011).

[3] Sotiropoulou, S., Sierra-Sastre, Y., Mark, S. S. and Batt, C. A. Biotemplated Nanostructured Materials, *Chemistry of Materials* **20**, 821–834 (2008).

[4] Encyclopedia Britannica Online, s. v. "nanotechnology" at <http://global.britannica.com/technology/nanotechnology >accessed 20 February 2016.

[5] Bottom-up Methods for Making Nanotechnology Products at < www.azonano.com> accessed 20 February 16.

[6] Brinker, C.J., Scherer, G. W. *Sol-Gel Science: The Physics and Chemistry of Sol-Gel Processing*. (Academic Press, 1990).

[7] Wright, J.D., Sommerdijk, N. A. J. M. *Sol-Gel Materials: Chemistry and Applications*. (Gordon and Breach Science Publ., 2001).

[8] Bogush G.H., Zukoski, C.F. Studies of the Kinetics of the Precipitation of Uniform Silica Particles through the Hydrolysis and Condensation of Silicon Alkoxides, *Journal of Colloid and Interface Science* **142**, 1–18 (1991).

[9] Iler, R. K. *The Chemistry of Silica: Solubility, Polymerization, Colloid and Surface Properties, and Biochemistry*.(Wiley, 1979).

[10] Brinker, C.J. Hydrolysis and Condensation of Silicates: Effects on Structure, *Journal of Non-Crystalline Solids* **100**, 31-50, (1988).

[11] Pouxviel, J.C., Boilot, J.P., Beloeli, J.C., Lallemand, J.Y.NMR Study of Sol-gel Polymerization, *Journal of Non-Crystalline Solids* **89**, 345-360, (1987).

[12] Stöber, W. Controlled Growth of Monodisperse Silica Spheres in the Micron Size range, *Journal of Colloid and Interface Science* **26**, 62-69, (1968).

[13] Kolbe G., Das Komplexchemische Verhalten Der Kieselsäiure, *Dissertation*, Friedrich-Schiller Universitäit (1956).

[14] Yanagisawa, T., Shimizu, T., Kuroda, K., Kato, C. Trimethylsilyl Derivatives of Alkyltrimethylammonium-Kanemite Complexes and Their Conversion to Microporous SiO2 Materials, *Bulletin of the Chemical Society of Japan* **63**, 1535–1537, (1990).

[15] anagisawa, T., Shimizu, T., Kuroda, K., Kato, C. The Preparation of Alkyltrimethylammonium-Kanemite Complexes and Their Conversion to Microporous Materials, *Bulletin of the Chemical Society of Japan* **63**, 988-992, (1990).

[16] Sattler, K. D.(ed.), *Handbook of Nanophysics. Functional Nanomaterials*. (Taylor & Francis, 2011).

[17] Beck, J. S., Vartuli, J. C., Kennedy, G. J., Kresge, C. T., Roth, W. J., Schramm, S. E. Molecular or Supramolecular Templating: Defining the Role of Surfactant Chemistry in the Formation of Microporous and Mesoporous Molecular Sieves, *Chemistry of Materials* **6**, 1816–1821 (1994).

[18] Beck, J. S., Vartuli, Roth, W. J., Schramm, Leonowics, M.E., Kresge, C.T., Schmitt, K.D., Chu, C.T.W., Olson, D.H., Sheppard, E.W., McCullen, S.B., Higiins, J.B., Chlenker, J.L., A New Family of Mesoporous Molecular Sieves Prepared with Liquid Crystal Templates, *Journal of the American Chemical Society* **114**, 10834-10843, (1992).

[19] Kresge, C. T., Leonowicz, M. E., Roth, W. J., Vartuli, J. C., Beck, J. S., Ordered Mesoporous Molecular Sieves Synthesized by a Liquid-Crystal Template Mechanism, *Nature* **359**, 710-712 (1992).

[20] Karge H. G., Weitkamp, J. (eds.), *Molecular Sieves: Science and Technology.* (Springer-Verlag, 1998).

[21] Vartuli, J. C., Schmitt, K. D., Kresge, C. T., Roth, W. J., Leonowicz, M. E., McCullen, S. B., Hellring, S. D., Beck, J. S., J. L. Schlenker, Effect of Surfactant/Silica Molar Ratios on the Formation of Mesoporous Molecular Sieves: Inorganic Mimicry of Surfactant Liquid-Crystal Phases and Mechanistic Implications, *Chemistry of Materials* **6**, 2317-2326, (1994).

[22] Karra, V.R., Moudrakovski, I. L., Sayari, A.Odd-Even Effect in the Synthesis of Mesoporous Silicate Molecular Sieves in the Presence of Alkyl Cetyl Dimethyl Ammonium Bromide, *Journal of Porous Materials* **3**, 77-82, (1996) .

[23] Kresge, C.T., Roth, W.J. The Discovery of Mesoporous Molecular Sieves from the Twenty Year Perspective, *Chemical Society Reviews* **42**, 3663-3670, (2013).

[24] Monnier, A., Schuth, F., Huo, Q., Kumar, D., Margolese, D., Maxwell, R. S., Stucky, G. D., Krishnamurty, M., Petroff, Firouzi, A., Janicke, M.,Chmelka, B.K. Cooperative Formation of Inorganic-Organic Interfaces in the Synthesis of Silicate Mesostructures, *Science* **261**, 1299–1303 (1993).

[25] Hoffmann, F., Cornelius, M., Morell, J., Fröba, M. Silica-Based Mesoporous Organic–Inorganic Hybrid Materials, *Angewandte Chemie International Edition* **45**, 3216–3251 (2006).

[26] Keene, M. T. J., Denoyel, R., Llewellyn, P. L., Ozone Treatment for the Removal of Surfactant to Form MCM-41 Type Materials, *Chemical Communications*, **20**, 2203–2204 (1998).

[27] Kawi, S., Supercritical Fluid Extraction of Surfactant Template from MCM-41, *Chemical Communications* **13**, 1407-1408 (1998).

[28] Tian, B., Liu, X., Yu, C., Gao, F., Luo, Q., Xie, S., Tu, B., Zhao, D. Microwave assisted template removal of siliceous porous *Chemical Communications* **11**, 1186–1187 (2002).

[29] Hitz, S., Prins, R. Influence of Template Extraction on Structure, Activity, and Stability of MCM-41 Catalysts, *Journal of Catalysis* **168**, 194–206 (1997).

[30] Lang, N., Tuel, A., A Fast and Efficient Ion-Exchange Procedure To Remove Surfactant Molecules from MCM-41 Materials, *Chemistry of Materials* **16**, 1961–1966 (2004).

[31] A Van Helden, A.K., Jansen, J.W., Vrij, A. Preparation and characterization of spherical monodisperse silica dispersions in nonaqueous solvents, *Journal of Colloid and Interface Science* **81**, 354–368 (1981).

[32] Matsoukas, T., Gulari, E. Dynamics of growth of silica particles from ammonia-catalyzed hydrolysis of tetra-ethyl-orthosilicate, J*ournal of Colloid and Interface Science* **124**, 252–261 (1988).

[33] Rao, K.S., El-Hami, K., Kodaki, T., Matsushige, K., Makino, K. A novel method for synthesis of silica nanoparticles, *Journal of Colloid and Interface Science* **289**, 125–131 (2005).

[34] Jin, H., Liu, Z., Ohsuna, T., Terasaki, O., Inoue, Y., Sakamoto, K., Nakanishi, T., Ariga, K., Che, S. Control of Morphology and Helicity of Chiral Mesoporous Silica, *Advanced Materials* **18**, 593–596 (2006).

[35] Naik, S.P., Elangovan, S.P., Okubo, T., Sokolov, I. Morphology Control of Mesoporous Silica Particles, *Journal of Physical Chemistry C* **111**, 11168–11173, (2007).

[36]Lelong, G., Bhattacharyya, S., Kline, S., Cacciaguerra, T., Gonzalez, M.A., Saboungi, M.-L. Effect of Surfactant Concentration on the Morphology and Texture of MCM-41 Materials, *The Journal of Physical Chemistry C* **112**, 10674–10680 (2008).

[37] Pang, X., Tang, F. Morphological control of mesoporous materials using inexpensive silica sources, *Microporous and Mesoporous Materials* **85**, 1–6 (2005).

[38] Shen, S., Gu, T., Mao, D., Xiao, X., Yuan, P., Yu, M., Xia, L., Ji, Q., Meng, L., Song, W., Yu, C., Lu, G. Synthesis of Nonspherical Mesoporous Silica Ellipsoids with Tunable Aspect Ratios for Magnetic Assisted Assembly and Gene Delivery, *Chemistry of Materials* **24**, 230–235 (2005).

[39] Denkova, A.G., Mendes, E., Coppens, M.-O. Effects of Salts and Ethanol on the Population and Morphology of Triblock Copolymer Micelles in Solution, *The Journal of Physical Chemistry B* **112**, 793–801 (2008).

[40] Sadasivan, S., Khushalani, D., Mann, S. Synthesis and shape modification of organo-functionalised silica nanoparticles with ordered mesostructured interiors, *Journal of Materials Chemistry* **13**, 1023–1029 (2003).

[41] Zhang, H., Sun, J., Ma, D., Bao, X., Klein-Hoffmann, A., Weinberg, G., Su, D., Schlögl, R. Unusual Mesoporous SBA-15 with Parallel Channels Running along the Short Axis, *Journal of the American Chemical Society* **126**, 7440–7441 (2004).

[42] Sadasivan, S., Fowler, C.E., Khushalani, D., Mann, S. Nucleation of MCM-41 Nanoparticles by Internal Reorganization of Disordered and Nematic-Like Silica–Surfactant Clusters, *Angewandte Chemie International Edition* **41**, 2151 (2002).

[43] Hao, N., Li, L., Tang, F. Facile preparation of ellipsoid-like MCM-41 with parallel channels along the short axis for drug delivery and assembly of Ag nanoparticles for catalysis, *Journal of Materials Chemistry A* **2**, 11565 (2004).

[44] Chen, Y., Chen, H.-R., Shi, J.-L. Construction of Homogenous/Heterogeneous Hollow Mesoporous Silica Nanostructures by Silica-Etching Chemistry: Principles, Synthesis, and Applications, *Accounts of Chemical Research* **47**, 125–137(2002).

[45] Das, S.K., Bhunia, M.K., Chakraborty, D., Khuda-Bukhsh, A.R., Bhaumik, A. Hollow spherical mesoporous phosphosilicate nanoparticles as a delivery vehicle for an antibiotic drug, *Chemical Communications* **48**, 2891 (2012).

[46] Zhu, Y., Meng, W., Gao, H., Hanagata, N. Hollow Mesoporous Silica/Poly(l -lysine) Particles for Codelivery of Drug and Gene with Enzyme-Triggered Release Property, *The Journal of Physical Chemistry C* **115,** 13630–13636 (2011).

[47] Peng, Y.-K., Lai, C.-W., Liu, C.-L., Chen, H.-C., Hsiao, Y.-H., Liu, W.-L., Tang, K.-C., Chi, Y., Hsiao, J.-K., Lim, K.-E., Liao, H.-E., Shyue, J.-J., Chou, P.-T. A New and Facile

Method To Prepare Uniform Hollow MnO/Functionalized mSiO 2 Core/Shell Nanocomposites, *ACS Nano* **5**, 4177–4187 (2011).

[48] Gu, H., Wang, J., Ji, Y., Wang, Z., Chen, W., Xue, G. Facile and controllable fabrication of gold nanoparticles-immobilized hollow silica particles and their high catalytic activity, *Journal of Materials Chemistry A* **1**, 12471 (2013).

[49]Jiang, Y., Ding, X., Zhao, J., Hari-Bala, Zhao, X., Tian, Y., Yu, K., Sheng, Y., Guo, Y., Wang, ZA facile route to synthesis of hollow SiO_2/Al_2O_3 spheres with uniform mesopores in the shell wall, *Materials Letters* **59**, 2893–2897 (2005).

[50] Le, Y., Chen, J.-F., Wang, J.-X., Shao, L., Wang, W.-C. A novel pathway for synthesis of silica hollow spheres with mesostructured walls, *Materials Letters* **58**, 2105–2108 (2004).

[51] Lin, Y.-S., Wu, S.-H., Tseng, C.-T., Hung, Y., Chang, C., Mou, C.-Y. Synthesis of hollow silica nanospheres with a microemulsion as the template, *Chemical Communications* 3542 (2009).

[52] Sasidharan, M., Zenibana, H., Nandi, M., Bhaumik, A., Nakashima, K. Synthesis of mesoporous hollow silica nanospheres using polymeric micelles as template and their application as a drug-delivery carrier, *Dalton Transactions* **42**, 13381 (2013).

[53] Argyo, C., Weiss, V., Bräuchle, C., Bein, T. Multifunctional Mesoporous Silica Nanoparticles as a Universal Platform for Drug Delivery, *Chemistry of Materials* **26**, 435–451 (2014).

[54] Rosenholm, J.M., Sahlgren, C., Lindén, M. Multifunctional mesoporous silica nanoparticles for combined therapeutic, diagnostic and targeted action in cancer treatment, *Curr Drug Targets* **12**, 1166–1186 (2011).

[55] Lee, J.E., Lee, N., Kim, T., Kim, J., Hyeon, T. Multifunctional Mesoporous Silica Nanocomposite Nanoparticles for Theranostic Applications, *Accounts of Chemical Research* **44**, 893–902 (2011).

[56] Stein, A., Melde, B.J., Schroden, R.C. Hybrid Inorganic-Organic Mesoporous Silicates—Nanoscopic Reactors Coming of Age, *Advanced Materials* **12**, 1403–1419 (2000)

[57] Zhang, J., Rosenholm, J.M. The viability of mesoporous silica nanoparticles for drug delivery, *Therapeutic Delivery*, **6,** 891-893, (2015).

[58] Rosenholm, J.M., Sahlgren, C., Lindén, M. Towards multifunctional, targeted drug delivery systems using mesoporous silica nanoparticles – opportunities & challenges, *Nanoscale* **2**, 1870 (2010).

[59] Cheng, T., Zhao, Q., Zhang, D., Liu, G. Transition-metal-functionalized ordered mesoporous silicas: an overview of sustainable chiral catalysts for enantioselective transformations, *Green Chem.* **17**, 2100–2122 (2015).

[60] Kim, C.O., Cho, S.J., Park, J.W. Hyperbranching polymerization of aziridine on silica solid substrates leading to a surface of highly dense reactive amine groups, *Journal of Colloid and Interface Science* **260**, 374–378 (2003).

[61] Sharma, K.K., Anan, A., Buckley, R.P., Ouellette, W., Asefa, T. Toward Efficient Nanoporous Catalysts: Controlling Site-Isolation and Concentration of Grafted Catalytic Sites on Nanoporous Materials with Solvents and Colorimetric Elucidation of Their Site-Isolation, *Journal of the American Chemical Society* **130**, 218–228 (2008).

[62] Lim, M.H., Stein, A. Comparative Studies of Grafting and Direct Syntheses of Inorganic–Organic Hybrid Mesoporous Materials, *Chemistry of Materials* **11**, 3285–3295 (1999).

[63] Brochier Salon, M.C., Belgacem, M.N. Hydrolysis-Condensation Kinetics of Different Silane Coupling Agents, *Phosphorus, Sulfur, and Silicon and the Related Elements,* **186**, 240-254 (2011).

[64] Tadros, T. F. *Surfactants in Agrochemicals*, Surfactant Science Series, 54 (Marcel Dekker, 1995).

[65] Hubbard, A.T. (Ed.) *Encyclopedia of Surface and Colloid Science.* (Marcel Dekker, Inc., 2002).

[66] Holmberg, K. (Ed.) *Surfactants and polymers in aqueous solution, 2nd ed.* (John Wiley & Sons: Chichester, 2003).

[67] Kontturi, K. Modification of Surfaces with Adsorption of Amphilic Polymers, *Dissertation*, Aalto University (2013).

[68] Prokop, A. (Ed.), *Intracellular delivery: fundamentals and applications*, (Springer, 2011).

[69] Brittain, W.J., Minko, S., A structural definition of polymer brushes, *Journal of Polymer Science Part A: Polymer Chemistry*, **45**, 3501-3802, (2007).

[70] Parveen, S., Misra, R., Sahoo, S.K. Nanoparticles: a boon to drug delivery, therapeutics, diagnostics and imaging, *Nanomedicine: Nanotechnology, Biology and Medicine* **8**, 147–166 (2012).

[71] Alharbi, K.K., Al-sheikh, Y.A. Role and implications of nanodiagnostics in the changing trends of clinical diagnosis, *Saudi Journal of Biological Sciences* **21**, 109–117 (2014).

[72] Sun, T., Zhang, Y.S., Pang, B., Hyun, D.C., Yang, M., Xia, Y. Engineered nanoparticles for drug delivery in cancer therapy, *Angew. Chem. Int. Ed. Engl.* **53**, 12320–12364 (2014).

[73] Wilczewska, A., Niemirowics, K., Markiewicz, K.H., Halina, C. Nanoparticles as drug delivery systems, *Pharmaceutical Reports* **64**, 1020–1037 (2012).

[74] Ayre, A., Kadam, V., Dand, N., Patel, P., Polymeric Micelles as a Drug Carrier for Tumor Targeting, *Chronicles of Young Scientists* **4,** 94, (2013).

[75] Lim, E.-K., Kim, T., Paik, S., Haam, S., Huh, Y.-M., Lee, K. Nanomaterials for Theranostics: Recent Advances and Future Challenges, *Chemical Reviews* **115**, 327–394 (2015).

[76] V Weissig, V., Pettinger, T., Murdock, N. Nanopharmaceuticals (part 1): Products on the Market, *International Journal of Nanomedicine* **9**, 4357-4373, (2014).

[77] Weissig, V., Guzman-Villanueva, D. Nanopharmaceuticals (part 2): Products in the pipeline, *International Journal of Nanomedicine*, **10**, 1245–1257 (2015).

[78] Jurkić, L.M., Cepanec, I., Pavelić, S.K., Pavelić, K. Biological and Therapeutic Effects of Ortho-Silicic Acid and Some Ortho-Silicic Acid-Releasing Compounds: New Perspectives for Therapy, *Nutrition & Metabolism* **10**, 2 (2013).

[79] Jaganathan, H., Godin, B. Biocompatibility Assessment of Si-Based Nano- and Micro-Particles, *Advanced Drug Delivery Reviews* **64**, 1800–1819, (2012).

[80] Bitar, A., Ahmad, N.M., Fessi, H., Elaissari, A. Silica-Based Nanoparticles for Biomedical Applications, *Drug Discovery Today* **17**, 1147-1154 (2012).

[81] Ow H., Larson D., Srivastava, M. , Baird, B.,A., W., W., Webb , U., Wiesner, Bright and stable core-shell fluorescent silica nanoparticles, *Nano Lett.*, **5**, 113–117 (2005).

[82] Benezra, M., Penate-Medina, O., Zanzonico, P., B., Schaer, D., Ow, H., Burns, A., DeStanchina, E., Longo, V., Herz, E., Iyer, S., Wolchok, J., Larson, S., M., Wiesner, U., Bradbury, M. S. Multimodal silica nanoparticles are effective cancer-targeted probes in a model of human melanoma, *J. Clin. Invest.* **121**, 2768–2780 (2011).

[83] Silicon Dioxide GRAS Notification, < http://www.fda.gov/default.htm> accessed 08 April 16

[84] Vallet-Regi, M., Rámila, A., del Real, R.P., Pérez-Pariente, A New Property of MCM-41: Drug Delivery System, *Chemistry of Materials* **13**,308-311 (2001).

[85] Georgelin, T., Bombard, S., Siaugue, J.-M., Cabuil, V. Nanoparticle-Mediated Delivery of Bleomycin, *Angewandte Chemie International Edition* **49**, 8897–8901 (2010).

[86] Xu, Z., Liu, S., Kang, Y., Wang, M., Glutathione- and pH-Responsive Nonporous Silica Prodrug Nanoparticles for Controlled Release and Cancer Therapy, *Nanoscale* **7**, 5859–5868 (2015).

[87] Compagnin, C., Baù, L., Mognato, M., Celotti, L., Miotto, G., Arduini, M., Moret, F., Fede, C., Selvestrel, F., Echevarria, I.M.R., Mancin, F., Reddi, E., The Cellular Uptake of Meta-Tetra(hydroxyphenyl)chlorin Entrapped in Organically Modified Silica Nanoparticles Is Mediated by Serum Proteins, *Nanotechnology* **20**, 345101 (2009).

[88] Chen, Y., Chen, H., Shi, J. In Vivo Bio-Safety Evaluations and Diagnostic/Therapeutic Applications of Chemically Designed Mesoporous Silica Nanoparticles, *Advanced Materials* **25**, 3144–3176 (2013).

[89] Wu, S.-H., Lin, Y.-S., Hung, Y., Chou, Y.-H., Hsu, Y.-H., Chang, C., Mou, C.-Y. Multifunctional Mesoporous Silica Nanoparticles for Intracellular Labeling and Animal Magnetic Resonance Imaging Studies, *ChemBioChem* **9**, 53–57 (2008).

[90] Lin, Y.-S., Hurley, K.R., Haynes, C.L. Critical Considerations in the Biomedical Use of Mesoporous Silica Nanoparticles, *The Journal of Physical Chemistry Letters* **3**, 364–374 (2012).

[91] He, Q., Zhang, J., Shi, J., Zhu, Z., Zhang, L., Bu, W., Guo, L., Chen, Y. The Effect of PEGylation of Mesoporous Silica Nanoparticles on Nonspecific Binding of Serum Proteins and Cellular Responses, *Biomaterials* **31**, 1085–1092 (2010).

[92] Lin, Y.-S., Abadeer, N., Haynes, C.L. Stability of Small Mesoporous Silicananoparticles in Biological Media, *Chem. Commun.* **47**, 532-534 (2011).

[93] Toy, R., Peiris, P.M., Ghaghada, K.B., Karathanasis, E. Shaping Cancer Nanomedicine: The Effect of Particle Shape on the *in Vivo* Journey of Nanoparticles, *Nanomedicine* **9**, 121-134 (2014).

[94] Gupta, R.B., Kompella, U.B. (Eds.), *Nanoparticle Technology for Drug Delivery*. (Taylor & Francis, 2006).

[95] Chiang, Y.-D., Lian, H.-Y., Leo, S.-Y., Wang, S.-G., Yamauchi, Y., Wu, K.C.-W. Controlling Particle Size and Structural Properties of Mesoporous Silica Nanoparticles Using the Taguchi Method, *The Journal of Physical Chemistry C* **115**, 13158–13165 (2011).

[96] Lu, F., Wu, S.-H., Hung, Y., Mou, C.-Y.Size Effect on Cell Uptake in Well-Suspended, Uniform Mesoporous Silica Nanoparticles, *Small* **5**, 1408-1413 (2009).

[97] Jiang, W., Kim, B.Y.S., Rutka, J.T., Chan, W.C.W. Nanoparticle-Mediated Cellular Response Is Size-Dependent, *Nature Nanotechnology* **3**, 145–150 (2008).

[98] Wang, J., Byrne, J.D., Napier, M.E., DeSimone, J.M. More Effective Nanomedicines through Particle Design, *Small* , **7**, 1919-1931 (2011).

[99] Hao, N., Li, L., Tang, F. Shape-Mediated Biological Effects of Mesoporous Silica Nanoparticles, *Journal of Biomedical Nanotechnology* **10**, 2508–2538 (2014).

[100] Huang, X., Teng, X., Chen, D., Tang, F., He, J. The Effect of the Shape of Mesoporous Silica Nanoparticles on Cellular Uptake and Cell Function, *Biomaterials* **31**, 438–448 (2010).

[101] Gratton, S.E.A., Ropp, P.A., Pohlhaus, P.D., Luft, J.C., Madden, V.J., Napier, M.E., DeSimone, J.M. The Effect of Particle Design on Cellular Internalization Pathways," *Proceedings of the National Academy of Sciences* **105**, 11613–11618 (2008).

[102] Kim, T.-W., Slowing, I.I., Chung, P.-W., Lin, V.S.-Y. Ordered Mesoporous Polymer–Silica Hybrid Nanoparticles as Vehicles for the Intracellular Controlled Release of Macromolecules, *ACS Nano* **5**, 360-366 (2011).

[103] Xia, T., Kovochich, M., Liong, M., Meng, H., Kabehie, S., George, S., Zink, J.I., Nel, A.E. Polyethyleneimine Coating Enhances the Cellular Uptake of Mesoporous Silica Nanoparticles and Allows Safe Delivery of siRNA and DNA Constructs, *ACS Nano* **3**, 3273–3286 (2009).

[104] Radu, D.R., Lai, C.-Y., Jeftinija, K., Rowe, E.W., Jeftinija, S., Lin, V.S.-Y. A Polyamidoamine Dendrimer-Capped Mesoporous Silica Nanosphere-Based Gene Transfection Reagent, *Journal of the American Chemical Society* **126**, 13216-13217 (2004).

[105] Thierry, B., Zimmer, L., McNiven, S., Finnie, K., Barbé, C., Griesser, H.J.Electrostatic Self-Assembly of PEG Copolymers onto Porous Silica Nanoparticles, *Langmuir* **24**, 8143-8150 (2008).

[106] Verma, A., Stellacci, F. Effect of Surface Properties on Nanoparticle–Cell Interactions, *Small* **6**, 12-21 (2010).

[107] Yu, T., Malugin, A., Ghandehari, H. Impact of Silica Nanoparticle Design on Cellular Toxicity and Hemolytic Activity, *ACS Nano* **5**, 5717-5728 (2011).

[108] Rosenholm, J.M., Gulin-Sarfraz, T., Mamaeva, V., Niemi, R., Özliseli, E., Desai, D., Antfolk, D., von Haartman, E., Lindberg, D., Prabhakar, N., Näreoja, T., Sahlgren, C. Prolonged Dye Release from Mesoporous Silica-Based Imaging Probes Facilitates Long-Term Optical Tracking of Cell Populations In Vivo, *Small* **12**, 1578-1592 (2016).

[109] Jambhrunkar, S., Qu, Z., Popat, A., Yang, J., Noonan, O., Acauan, L., Ahmad Nor, Y., Yu, C., Karmakar, S.,Effect of Surface Functionality of Silica Nanoparticles on Cellular Uptake and Cytotoxicity, *Molecular Pharmaceutics* **11**, 3642-3655 (2014).

[110] Tang, Q., Yao Xu, Dong Wu, Sun, Y., Wang, J., Jun X., Feng D. Studies on a New Carrier of Trimethylsilyl-Modified Mesoporous Material for Controlled Drug Delivery, *Journal of Controlled Release* **114**, 41-46 (2006).

[111] Quellec, P., Gref, R., Perrin, L., Dellacherie, E., Sommer, F., Verbavatz, J.M., Alonso, M.J.Protein Encapsulation within Polyethylene Glycol-Coated Nanospheres. I. Physicochemical Characterization, *Journal of Biomedical Materials Research* **42**, 45-54 (1998).

[112] Mosqueira, V.C.F., Legrand, P., Gref, R., Heurtault, B., Appel, M., Barratt, G. Interactions between a Macrophage Cell Line (J774A1) and Surface-Modified Poly(D,L-Lactide) Nanocapsules Bearing Poly(ethylene Glycol), *Journal of Drug Targeting* **7**, 65-78 (1999).

[113] Louguet, S., Kumar, A.C., Guidolin, N., Sigaud, G., Duguet, E., Lecommandoux, S., Schatz, C.Control of the PEO Chain Conformation on Nanoparticles by Adsorption of PEO-Block-Poly(L-Lysine) Copolymers and Its Significance on Colloidal Stability and Protein Repellency, *Langmuir* **27**, 12891–12901 (2011).

[114] Comparision of Particle Sizing Methods at < www.cpsinstruments.eu> accessed 22 Feburary 16

[115] Malvern Instruments at <http://www.malvern.com/en/>, accessed 19 Feburary16

[116] The distribution of ions around a charged particle in solution at <www.pharmaceuticalonline.com> accessed 19 February 16

[117] Zeta potential - An introduction in 30 minutes at <http://www.malvern.com/en/>, accessed 19 Feburary16

[118] Properties of Electrons, their Interactions with Matter and Applications in Electron Microscopy at< http://www.microscopy.ethz.ch/>accessed 19 February 16

[119] Wess, T.J., Drakopoulos, M., Snigirev, A., Wouters, J., Paris, O., Fratzl, P., Collins, M., Hillier, J., Nielsen, K.The Use of Small-Angle X-Ray Diffraction Studies for the Analysis of Structural Features in Archaeological Samples, *Archaeometry* **43**, 117–129 (2001).

[120] Ciesla, U., Schüth, F. "Ordered Mesoporous Materials," *Microporous and Mesoporous Materials* **27**, 131–149 (1999).

[121] Sing, K. The Use of Nitrogen Adsorption for the Characterization of Porous Materials, *Colloids and Surfaces A: Physicochemical and Engineering Aspects* **187**, 3–9 (2001).

[122] Sing, K.S.W, Everett, D.H., Haul, R.A.W., Moscou, L., Pierotti, R.A., Rouquerol, F., Siemieniwska, T. Reporting physisorption data for gas /solid systems with special reference to the determination of surface area and porosity. *Pure and Applied Chemistry*, **57**, 603-619 (1985).

[123] Rouquerol, F., Rouquerol, J., Sing, K.S.W. *Adsorption by Powders and Porous Solids: Principles, Methodology, and Applications*. (Academic Press, 1999).

[124] Kruk, M., Jaroniec, M., Sayari, A.Application of Large Pore MCM-41 Molecular Sieves To Improve Pore Size Analysis Using Nitrogen Adsorption Measurements, *Langmuir* **13**, 6267-6273 (1997).

[125] Neimark, A.V., Ravikovitch, P.I. Capillary Condensation in MMS and Pore Structure Characterization, *Microporous and Mesoporous Materials* **44,** 697-707 (2001).

[126] Overview of spectroscopy at <www.chemwiki.ucdavis.edu> accessed 19 February 16

[127] Ladbury, J. E. Application of Isothermal Titration Calorimetry in the Biological Sciences: Things Are Heating Up, *BioTechniques* **37**, 885-887 (2004).

[128] Freire, E., Mayorga, O.L., Straume, M. Isothermal Titration Calorimetry, *Analytical Chemistry* **62**, 950A – 959A (1990).

[129] Thermogravimetric analysis-Beginner Guide at < www.perkinelmer.com> accessed 19 February 16

[130] Stöber, W., Fink, A., Bohn, E.Controlled Growth of Monodisperse Silica Spheres in the Micron Size Range, *Journal of Colloid and Interface Science* **26**, 62-69 (1968).

[131] Payne, C.C., Bergna, H.E. (Editor) Applications of Colloidal Silica: Past, Present, and Future, *The Colloid Chemistry of Silica* **234,** 581-594,american Chemical Society, Washington DC (1994).

[132] He, Q., Shi, J., Chen, F., Zhu, M., Zhang, L. An Anticancer Drug Delivery System Based on Surfactant-Templated Mesoporous Silica Nanoparticles, *Biomaterials* **31**, 3335-3346 (2010).

[133] Gu, J., Fan, W., Shimojima, A., Okubo, T. Organic–Inorganic Mesoporous Nanocarriers Integrated with Biogenic Ligands, *Small* **3**, 1740–1744 (2007).

[134] Zhang, J., Li, X., Rosenholm, J.M., Gu, H. Synthesis and Characterization of Pore Size-Tunable Magnetic Mesoporous Silica Nanoparticles, *Journal of Colloid and Interface Science* **361**, 16-24 (2011).

[135] Wong, Y.J., Zhu, L., Teo, W.S., Tan, Y.W., Yang, Y., Wang, C., Chen, H., Revisiting the Stöber Method: Inhomogeneity in Silica Shells, *Journal of the American Chemical Society* **133**, 11422-11425 (2011).

[136] Xia, K., Lu, C., Yang, Y., Zhang, B., Effect of Vinyltriethoxysilane Addition on the Pyrolytic Conversion of Tetraethoxysilane Based Silica Gel, *Journal of Sol-Gel Science and Technology* **69**, 266-271 (2014).

[137] Ottaviani, M.F., Moscatelli, A., Desplantier-Giscard, D., Di Renzo, F., Kooyman, P.J., Alonso, B., Galarneau, A. Synthesis of Micelle-Templated Silicas from Cetyltrimethylammonium Bromide/1,3,5-Trimethylbenzene Micelles, *The Journal of Physical Chemistry B* **108**, 12123-12129 (2004).

[138] Mathur, S., Moudgil, B.M. Adsorption Mechanism(s) of Poly(Ethylene Oxide) on Oxide Surfaces, *Journal of Colloid and Interface Science* **196**, 92-98 (1997).

[139] S.I Jeon, S., Lee, J., Andrade, J., Degennes, P. Protein—surface Interactions in the Presence of Polyethylene Oxide, *Journal of Colloid and Interface Science* 142, 149-158, (1991).

[140] Rosenholm, J.M., Lindén, M., Wet-Chemical Analysis of Surface Concentration of Accessible Groups on Different Amino-Functionalized Mesoporous SBA-15 Silicas, *Chemistry of Materials* **19**, 5023-5034 (2007).

[141] Rosenholm, J.M. Modular Design of Mesoporous Silica Materials: Towards Multifunctional Drug Delivery System, *Dissertation*, Åbo Akademi University (2008).

[142] Salonen, J., Laitinen, L., Kaukonen, A.M., Tuura, J., Björkqvist, M., Heikkilä, T., Vähä-Heikkilä, K., Hirvonen, J., Lehto, V.-P. Mesoporous Silicon Microparticles for Oral

Drug Delivery: Loading and Release of Five Model Drugs, *Journal of Controlled Release* **108**, 362-374 (2005).

[143] Auger, A., Samuel, J., Poncelet, O., Raccurt, O. A Comparative Study of Non-Covalent Encapsulation Methods for Organic Dyes into Silica Nanoparticles, *Nanoscale Research Letters* **6**, 328 (2011).

[144] Tian, Y., Shumway, B.R., Youngbull, A.C., Li, Y., Jen, A.K.-Y., Johnson, R.H., Meldrum, D.R. Dually Fluorescent Sensing of pH and Dissolved Oxygen Using a Membrane Made from Polymerizable Sensing Monomers, *Sensors and Actuators. B, Chemical* **147**, 714-722 (2010).

[145] Takakusa, H., Kikuchi, K., Urano, Y., Higuchi, T., Nagano, T. Intramolecular Fluorescence Resonance Energy Transfer System with Coumarin Donor Included in Beta-Cyclodextrin, *Analytical Chemistry* **73**, 939-942 (2001).

[146] Kawanishi, Y., Kikuchi, K., Takakusa, H., Mizukami, S., Urano, Y., Higuchi, T., Nagano, T. Design and Synthesis of Intramolecular Resonance-Energy Transfer Probes for Use in Ratiometric Measurements in Aqueous Solution, *Angewandte Chemie* **39**, 3438-3440 (2000).

[147] Şen Karaman, D., Gulin-Sarfraz, T., Hedström, G., Duchanoy, A., Eklund, P., Rosenholm, J.M. Rational Evaluation of the Utilization of PEG-PEI Copolymers for the Facilitation of Silica Nanoparticulate Systems in Biomedical Applications, *Journal of Colloid and Interface Science* **418,** 300-310 (2014).

[148] Faucher, L., Guay-Bégin, A.-A., Lagueux, J., Côté, M.-F., Petitclerc, É., Fortin, M.-A. Ultra-Small Gadolinium Oxide Nanoparticles to Image Brain Cancer Cells in Vivo with MRI, *Contrast Media & Molecular Imaging* **6**, 209-218 (2010).

[149] Long, X.-H., Yang, P.-Y., Liu, Q. , Yao, J., Wang, Y., He, G.-H., Hong, G.-Y., Ni, J.-Z., Metabolomic profiles delineate potential roles for gadolinium chloride in the proliferation or inhibition of Hela cells , *BioMetals*, **24**, 663–677 (2011).

[150] Davda, J., Labhasetwar, V., Characterization of Nanoparticle Uptake by Endothelial Cells, *International Journal of Pharmaceutics* **233**, 51-59 (2002).

[151] Lynch, I., Dawson, K.A., Protein-Nanoparticle Interactions, *Nano Today* **3**, 40-47 (2008).

[152] Rahman, M., Laurent, S., Tawil, N., Yahia, L., Mahmoudi, M., *Protein-Nanoparticle Interactions*, *The Bio-Nano Interface.* (Springer, 2013)

[153] Lundqvist, M., Stigler, J., Elia, G., Lynch I., Cedervall, T., Dawson, K. A. Nanoparticle size and surface properties determine the protein corona with possible implications for biological impacts, *Proceedings of the National Academy of Sciences of the United States of America* **105**, 14265–14270, (2008).

[154] Lundqvist, M., Stigler, J., Cedervall, T., Berggard, T., Flanagan, M. B., Lynch, I., Elia, G., Dawson, K. The evolution of the protein corona around nanoparticles: a test study, *ACS Nano* **5**, 7503–7509 (2011).

[155] Mahmoudi, M., Lynch, I., Ejtehadi, M.R., Monopoli, M.P., Bombelli, F.B., Laurent, S. Protein-nanoparticle interactions: opportunities and challenges, *Chem Rev* **111**, 5610–5637 (2011).

[156] Aggarwal, P., Hall, J.B., McLeland, C.B., Dobrovolskaia, M.A., McNeil, S.E. Nanoparticle Interaction with Plasma Proteins as It Relates to Particle Biodistribution, Biocompatibility and Therapeutic Efficacy, *Advanced Drug Delivery Reviews* **61**, 428-437 (2009).

[157] Gessner,A., Lieske, A., Paulke, B., Muller, R. Influence of surface charge density on protein adsorption on polymeric nanoparticles: analysis by two-dimensional electrophoresis *Eur. J. Pharm. Biopharm.,* **54**, 165–170 (2002).

[158] Cedervall, T., Lynch, I., Foy, M., Berggård, T., Donnelly, S.C., Cagney, G., Linse, S., Dawson, K.A. Detailed Identification of Plasma Proteins Adsorbed on Copolymer Nanoparticles, *Angewandte Chemie International Edition* **46,** 5754-5756 (2007).

159 Walkey, C.D., Chan, W.C.W, Understanding and controlling the interaction of nanomaterials with proteins in a physiological environment, Chemical Society Reviews, **41**, 2780-2799 (2012).

[160] Malmsten, M., Emoto, K., Van Alstine, J. M. "Effect of Chain Density on Inhibition of Protein Adsorption by Poly(ethylene Glycol) Based Coatings," *Journal of Colloid and Interface Science*, **202**, 507–517 (1998).

[161] Vonarbourg, A., Passirani, C., Saulnier, P., Benoit, J.-P. Parameters Influencing the Stealthiness of Colloidal Drug Delivery Systems, *Biomaterials* **27**, 4356-4373 (2006).

[162] Stutz, H. Protein Attachment onto Silica Surfaces--a Survey of Molecular Fundamentals, Resulting Effects and Novel Preventive Strategies in CE, *Electrophoresis* **30**, 2032-2061 (2009).

[163] Verzola, B., Gelfi, C., Righetti, P.G., Protein Adsorption to the Bare Silica Wall in Capillary Electrophoresis, *Journal of Chromatography A* **868**, 85-99 (2000).

ISBN 978-952-12-3406-4